

Calibration of the strain amplitude recorded with DAS using a strainmeter array

Thomas Forbriger^{*1}, Nasim Karamzadeh^{1,2}, Jérôme Azzola³,
Emmanuel Gaucher³, Rudolf Widmer-Schmidrig⁴, Andreas Rietbrock¹

¹Karlsruhe Institute of Technology (KIT), Geophysical Institute, Karlsruhe, Germany

²now at University of Münster Institut für Geophysik, Münster, Germany

³Karlsruhe Institute of Technology (KIT), Institute for Applied Geosciences, Karlsruhe, Germany

⁴Institute of Geodesy, University of Stuttgart, Stuttgart, Germany

*Corresponding author: Thomas.Forbriger@kit.edu, Karlsruhe Institute of Technology (KIT), Geophysical Institute (GPI), Black Forest Observatory (BFO), Heubach 206, 77709 Wolfach, Germany

Abstract

The power of distributed acoustic sensing (DAS) lies in its ability to sample deformation signals along an optical fiber at hundreds of locations with only one interrogation unit (IU). While the IU is calibrated to record ‘fiber strain’, the properties of the cable and its coupling to the rock control the ‘strain transfer rate’ and hence how much of ‘rock strain’ is represented in the recorded signal. We use DAS recordings in an underground installation near an array of strainmeters in order to calibrate the ‘strain transfer rate’ in situ, using earthquake signals between 0.05 Hz and 0.1 Hz. A tight-buffered cable and a standard loose-tube telecommunication cable (running in parallel) are used, where a section of both cables loaded down by loose sand and sand bags is compared to a section, where cables are just unreel on the floor. The ‘strain transfer rate’ varies between 0.13 and 0.53 depending on cable and installation type. The sandbags show no obvious effect and the tight-buffered cable generally provides a larger ‘strain transfer rate’. Calibration of the ‘strain transfer rate’ with respect to the strainmeter does not depend on wave propagation parameters. Hence it is applicable to the large amplitude surface wave signal in a strain component almost perpendicular to the great-circle direction for which a waveform comparison with seismometer data does not work. The noise background for ‘rock strain’ in the investigated band is found at about an rms-amplitude of 0.1 nstrain in 1/6 decade for the tight-buffered cable. This allows a detection of marine microseisms at times of high microseism amplitude.

1 Introduction

Distributed Acoustic Sensing (DAS) measures dynamic strain in an optical fiber. The DAS interrogation unit (IU) sends laser-generated coherent light into an optical fiber possibly extending for tens of kilometers. The light gets partly back-scattered by Rayleigh scattering due to manufacturing imperfections along the optical fiber and is sensitive to rapid variations in strain, commonly referred to as dynamic strain. Pioneering work by Dakin (1990), followed by Taylor and Lee (1993), recognized the potential of coherent Rayleigh back-scatter in assessing spatial disturbances in optical fibers. Following this work a range of techniques has been developed and implemented in IUs to measure the phase of the back-scattered signal. Hartog (2017) summarizes these pro-

gressions and outlines applications of distributed optical fiber sensors across various domains.

In seismology, the power of DAS lies in its ability to sample deformation signals along an optical fiber at hundreds of locations over distances of many kilometers with a single IU. In some applications, unused telecommunication infrastructures (so-called dark-fibers) can be leveraged, which significantly reduces the necessary effort for field deployment. Lindsey and Martin (2021) and Li et al. (2021) present an overview of fields of application in geosciences. Most of these applications rely only on the phase information in the recorded data.

Use cases, which rely on amplitude are less frequent. Such a use case would be the measurement of volume strain for the reduction of Newtonian Noise (Harms, 2015; Harms et al., 2022), as being planned for the Ein-

stein Telescope (ET Steering Committee, 2020). With well calibrated DAS strain recordings on cables running in six different directions from a single location, the full strain tensor could be composed. This requires a proper calibration of the ‘strain transfer rate’ (the fraction of ‘rock strain’ picked up as ‘fiber strain’) and a sufficiently low detection level, such that the strain background signal is resolved. Rademacher (2024) recently pointed at the limitations which still exist for DAS in both respects. We investigate these in the current study.

Signals recorded by the DAS IU represent the deformation of the fiber (denoted here as ‘fiber strain’). However, observations showing that the signal from two colocated cables might differ in amplitude (Azzola et al., 2022, and the current study) suggest that ‘fiber strain’ does not always represent the actual ‘rock strain’. This discrepancy can arise from the coupling of the fiber to the ground through the various layers of the cable.

Reinsch et al. (2017), for example, focus on the internal structure of an optic fiber cable and discuss this discrepancy based on a physical model (Li et al., 2006) of a DAS cable, based on actual material properties. They derive the ‘strain transfer rate’ as the ratio between ‘fiber strain’ and ‘rock strain’. In particular gel layers in loose-tube cables let the ‘strain transfer rate’ be less than 1 due to their small value of Young’s modulus. These thixotropic fluids are used to protect the fibers from damage. Reinsch et al. (2017) estimate that during measurement their yield point is not exceeded, such that they behave in a linear elastic way. In practice the parameters of the different layers in the cable are not available from manufacturers and the coupling to the rock is controlled by the actual installation conditions. For this reason the ‘strain transfer rate’ can be determined empirically only.

The studies by Lindsey et al. (2020) and Paitz et al. (2020) are two examples for in-situ calibration experiments. Both use a Silixa iDAS IUs and both primarily use surface wave signals.

Lindsey et al. (2020) focus on the low-frequency band from about 0.08 Hz to 1 Hz. They not only describe the calibration experiment, but also provide a well-written introduction to DAS including the conversion from optical phase to strain, the coupling of rock to fiber, and typical optical sources of noise. The DAS signals in their study are recorded on a gel-filled loose-tube dark fiber installed in a conduit. They convert the signals to particle velocity based on the assumption of plane waves and compare with the recordings of a broad-band seismometer at 66 m distance. The needed scaling factor, which is phase velocity along the fiber, is obtained by fk-analysis of 1 km of DAS data, which allows to capture wave dispersion and does not rely on the assumption of great-circle propagation. Though the superposition of Rayleigh- and Love-waves (both prop-

agating at difference phase velocity) might still present a problem. The authors use surface waves from four teleseismic earthquakes to demonstrate that the amplitude response of the DAS is like nominally expected for frequencies below 0.1 Hz, although there is a significant amplitude fluctuation of a factor of 10 along the fiber (Lindsey et al., 2020, their figure 6b). For frequencies higher than 0.1 Hz, they find DAS amplitudes larger than nominal by up to about 10 dB (about a factor of 3). The analysis of earthquakes and marine microseisms in this band yields inconsistent results in that the amplification seen for marine microseisms is larger. As a potential cause, the authors mention possible problems with the fk-analysis at near-perpendicular incidence of marine microseisms. While they prefer fiber coupling issues as the explanation for the amplification, they do not clarify how a passive mechanism could account for the signal amplification.

Paitz et al. (2020) derive a frequency dependent transfer function of DAS signals with respect to reference recordings for seven frequency bands, spanning a total range from 0.34 mHz to 60 Hz. As test signals, they use hydraulic stimulation and surface waves from four earthquakes (one per analyzed frequency band) and one icequake. The installation types of DAS cables in the various experiments differ significantly, without the possibility to track down systematic variations to the type of installation. The hydraulic stimulation experiment carried out for the lowest frequency bands is exceptional in that the DAS fiber is cemented in a borehole and in that a fiber-Bragg-grating (FBG) strainmeter could be used as a reference, while for the others strain had to be estimated from particle velocity. Though the results for this hydraulic stimulation does not appear exceptional in terms of deviation from the expected nominal response. Overall the authors report a variation of the amplitude response by ± 10 dB (about a factor of 0.3 to 3) around the nominal value.

When comparing DAS recordings with seismometer recordings a translating of strain or strain rate into particle displacement or velocity (or vice versa) is necessary. This is only possible for non-dispersive plane waves with known ray-parameter. The limitations of this approach and the resulting waveform dissimilarity are shown by Lindsey et al. (2020, their figure 4a) for example. Paitz et al. (2020) mention incorrect phase-velocity estimates as a possible source of inaccuracy.

In the current study, we directly compare the recordings of a DAS IU with those from the long-running array of Invar-wire strainmeters at the Black Forest Observatory (BFO). Both, the DAS recorded strain and the signal from the strainmeter can be expected to represent the same rock deformation, independent of its cause and independent of wave parameters in particular. Hence, this comparison allows for direct calibration of the DAS

system’s amplitude response, not limited to a specific wave type and without additional uncertainties due to limited accuracy of ray-parameters. Based on this calibration we estimate the detection threshold for strain recordings. The signal-to-noise ratio of both systems is appropriate for this purpose in the frequency band between 0.05 Hz and 0.1 Hz.

Our study further extends beyond the work of Lindsey et al. (2020) and Paitz et al. (2020) by interrogating two fibers in each cable, allowing us to distinguish coupling issues that effect all fibers in a cable, from photonic effects (like optical fading), which are specific to each fiber. We use a significantly larger dataset, comprising 19 earthquakes, covering almost all back-azimuths and include body waves in the analysis. The simultaneous interrogation of fibers in two cables at two locations enables us to investigate the direct differences observed under four different coupling conditions.

2 DAS installation and instruments

Black Forest Observatory (BFO) is situated in a former silver mine in the central Black Forest, Germany (Emter et al., 1994). The gallery that hosts the instruments (Fig. 1) is mostly horizontal and is excavated in granite. The granite is covered with Triassic sedimentary rocks (Emter et al., 1994). The study focuses on two straight sections of the tunnel, ‘Anton Gang’ and ‘Vorstollen’. Overburden increases with distance to the tunnel entrance, is about 100 m at the ‘Anton Gang’ and reaches 170 m at the ‘Strainmeter array’.

2.1 Distributed acoustic sensing (DAS)

Two fiber optic cables are installed in the tunnel. They are unreelied on the floor of the gallery and are in direct contact with the formation. In the section called ‘Anton Gang’ the cables are loaded down by sand and tightly spaced sandbags in order to improve the mechanical coupling to the rock, provide thermal shielding and cover the cable against water dripping from the gallery ceiling. The blue cable in Fig. 1 is a standard flexible telecommunication cable with loose-tube fibers embedded in gel. The green cable in Fig. 1 has a stiff jacket containing tight-buffered fibers (see section S1.2 in the supplemental material for additional details). We use two single mode fibers in each of the cables and splice them in series, such that the ‘Anton Gang’ and the ‘Vorstollen’ are both sampled four times. The signals from the fibers are sampled by a Febus A1-R interrogation unit (IU) installed in the laboratory (Fig. 1). The DAS recording parameters are listed in Table 1. The Febus A1-R recording time is synchronized by GPS,

like all other digitizers involved in the current study. When the IU was installed in the mine, the GPS timing signal was provided through an optical link (Meinberg GOAL: GPS Optical Antenna Link).

The Febus A1-R IU operates on the principle of differential phase-measuring distributed acoustic sensing. The light that is back-scattered in the optical fiber is mixed with a reference signal to measure the differential phase over a gauge length, subsequently leading to distributed strain-rate measurements, which is converted to strain by integration over time. The A1-R falls within the category of heterodyne Distributed Vibration Sensing (hDVS) systems, using a single-pulse heterodyne approach for phase detection, as described by Pan et al. (2011).

2.2 Reference instruments

BFO operates an array of three well calibrated, 10 m long, horizontal, Invar-wire strainmeters (Fig. 1). The SEED codes for the instruments are IL.BFO.00.BSA, IL.BFO.00.BSB, and IL.BFO.00.BSC. Their design is based on the instruments by King and Bilham (1976) and are discussed in more detail by Zürn et al. (2015). Agnew (1986) and Zürn (2012) discuss instruments of this type and their properties. These instruments are primarily designed to record very-long period signals, such as tidal strain or Earth’s free oscillations. For this reason they are equipped with an in-situ calibration device, which makes use of interferometrically calibrated ‘Crapaudines’ (Verbaandert, 1959). The accuracy of this calibration for the strainmeters is about 2 per cent. Comparison against theoretical tidal strain ensures a stability of the calibration of about 5 per cent in the long run. Section S2.4 in the supplemental material gives further details.

At short signal period the Invar-wire strainmeters show a linear parasitic sensitivity to vertical ground acceleration because of the inertia of the pick-up system. They provide useful strain signals at frequencies below 1 Hz. We use the instruments at frequencies below 0.1 Hz (which provides a safety-margin to the parasitic response) as a reference to present ‘rock strain’.

We use signals recorded by the STS-2 broad-band seismometer (Fig. 1) to demonstrate the limitations of waveform comparisons with particle velocity derived strain. The SEED codes for its three components are GR.BFO..BHZ, GR.BFO..BHN, and GR.BFO..BHE.

3 Data and data processing

3.1 Available data

The installation of DAS cables as shown in Fig. 1 was used for recording from May 22, 2022 until March 13,

BFO (Black Forest Observatory)

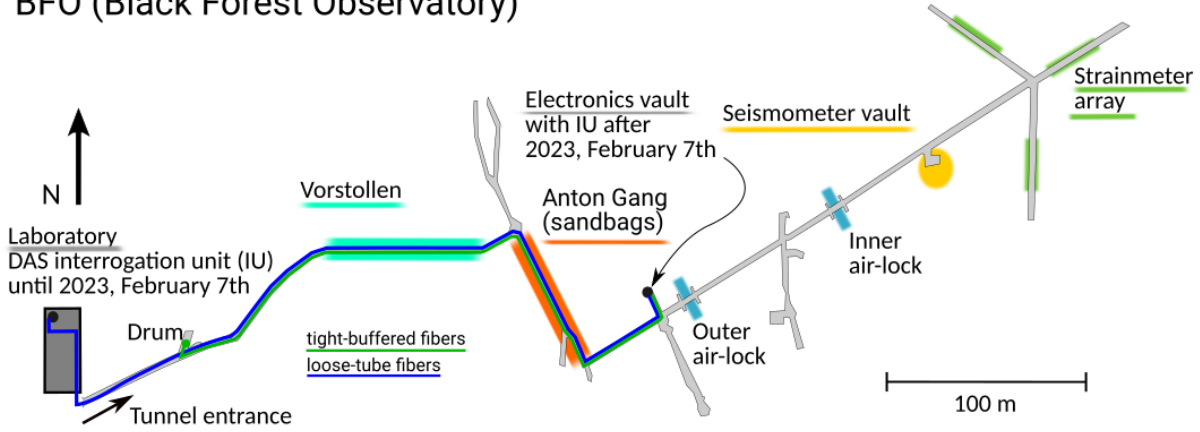


Figure 1: Floor map of the gallery of the former silver mine in which the instruments are installed. Two fiber optic cables are installed in the part in front of the air-locks. The cables are loaded down with tightly packed sandbags in the section called ‘Anton Gang’ (azimuth N330°E). We compare signals recorded in the ‘Anton Gang’ (69 m long) with signals recorded in the straight section called ‘Vorstollen’ (80 m long, azimuth N90°E), strain derived from the ‘Strainmeter array’, and strain simulated from the STS-2 broad-band seismometer in the ‘Seismometer vault’. The overburden increases from the ‘Tunnel entrance’ (0 m) to the ‘Anton Gang’ (100 m) to the ‘Strainmeter array’ (170 m). 585 m of the tight-buffered cable are rolled up on a ‘Drum’ that is used to remove coherent laser noise.

Table 1: Recording parameters for the Febus A1-R.

Interrogation unit (IU) Febus A1-R	
Software:	version 2.2.2
optical wavelength:	1550.12 nm
Fiber length:	2200 m
Pulse width:	5 m
Block rate:	1 Hz
Pulse rate frequency:	5 kHz
Ampli power:	28 dBm
Sampling resolution:	80 cm
Gauge length (GL):	50 m
Derivation time (DT):	20 ms
Channel spacing:	24.8 m

2023. The IU was moved on February 7, 2023 from the laboratory to the electronics vault in the mine (see Fig. 1 and Figs. S1 and S2 in the supplemental material for additional details). In both, ‘Anton Gang’ and ‘Vorstollen’, we focus on four almost colocated read-out locations that are separated by 5 m to 15 m. In all cases, the section of gauge length completely falls into the ‘Anton Gang’ or ‘Vorstollen’, such that the strain recordings are representative of the azimuth of these gallery sections.

From the GEOFON catalog (Quinteros et al., 2021) we find 84 earthquakes with moment magnitude larger than 6 in the recording time period. 21 of them show a maximum strain amplitude of larger than 1 nstrain in a visual inspection, which is considered large enough to provide a sufficient signal-to-noise ratio in the DAS data. For 19 of the events DAS data is available and allows an analysis. Their backazimuths (BAZ) cover all directions with an azimuthal gap of 107° (BAZ between $N110^\circ E$ and $N217^\circ E$). Event characteristics are detailed in the supplementary material (see Table S2). The largest amplitudes are found in the surface wave train. For body-waves, the horizontal strain amplitude is the smaller the steeper the ray incidence.

The strongest signals are recorded from the main shocks (Mw 7.7 and Mw 7.6) of the Kahramanmaraş earthquake sequence (Melgar et al., 2023) on February 6th 2023. Their body-wave signals have large enough amplitude of a few nstrain to be included in the analysis. This is due to the larger earthquake magnitude and the smaller epicentral distance (23°), compared to the other analyzed events in this study, which both result in rather large amplitude in general. In the set of analyzed events their surface waves provide by far the largest strain amplitudes of about 130 nstrain and about 250 nstrain, respectively, as measured by the Invar-wire strainmeters in the investigated frequency band of 0.05 Hz to 0.1 Hz.

For the comparison of strain waveforms, we can use 46 recordings for each combination of cable (tight-buffered and loose-tube) and location (‘Anton Gang’ and ‘Vorstollen’). For the loose-tube cable in ‘Anton Gang’ we use only 44 recordings, as the configuration was modified on 2023, February 7th.

3.2 Pre-processing of DAS data

Waveforms sampled simultaneously on a section of the tight-buffered cable rolled up on a ‘Drum’ (see Fig. 1 and Table S1 in the supplemental material) get averaged and subtracted from the recordings in order to reduce common mode laser noise (Lindsey et al., 2020, their section 2.6 Optical Noise). For a gauge-length of 50 m this coherent noise component clearly dominates the background level of the DAS signal at frequencies below 0.5 Hz and peaks at about 0.07 Hz with ‘fiber

strain’-amplitudes of a few nstrain. By subtracting this coherent signal component, the background level is lowered by up to 20 dB near 0.1 Hz. In the current application, it is essential that the drum is sufficiently decoupled from the rock and that the fiber coiled on the drum does not pick up the earthquake signal. Otherwise the correction procedure would affect the earthquake signal amplitude. In the supplemental material (section S2.3 and Figures S26 and S27) we demonstrate that no signature of the earthquake is apparent in the correction signal.

Data is converted from strain rate to strain for which the noise floor rapidly increases at low frequencies, such that we focus our analysis on frequencies higher than 0.05 Hz.

3.3 Linear strain from the strainmeter array

In order to compare the DAS recordings with recordings of the strainmeters, we derive linear strain in either the direction ‘Anton Gang’ or ‘Vorstollen’ by a linear combination of the signals recorded by the three strainmeters. Zürn et al. (2015, their eq. 2) specify linear strain

$$\epsilon(\psi) = \epsilon_{\theta\theta} \cos^2(\psi) + \epsilon_{\phi\phi} \sin^2(\psi) - \epsilon_{\theta\phi} \sin(2\psi) \quad (1)$$

in azimuth ψ as a function of the components $\epsilon_{\theta\theta}$, $\epsilon_{\phi\phi}$, and $\epsilon_{\theta\phi}$ of the 2D strain tensor. Here, ‘Anton Gang’ and ‘Vorstollen’ are in azimuth $N330^\circ E$ and $N90^\circ E$, respectively. Based on this, we compute linear strain in azimuth ψ

$$\epsilon(\psi) = \begin{pmatrix} \cos^2(\psi) \\ \sin^2(\psi) \\ -\sin(2\psi) \end{pmatrix} \mathbf{M}^{-1} \begin{pmatrix} \epsilon_A \\ \epsilon_B \\ \epsilon_C \end{pmatrix}, \quad (2)$$

from the strain recorded by the three array-instruments, where ϵ_A , ϵ_B , and ϵ_C are in azimuth $N2^\circ E$, $N60^\circ E$, and $N300^\circ E$, respectively. They correspond to the SEED channel names BSA, BSB, and BSC. The rotation matrix

$$\mathbf{M}^{-1} = \begin{pmatrix} 1.002 & -0.041 & 0.040 \\ -0.334 & 0.680 & 0.653 \\ 0.000 & -0.577 & 0.577 \end{pmatrix} \quad (3)$$

is the inverse of

$$\mathbf{M} = \begin{pmatrix} \cos^2(2^\circ) & \sin^2(2^\circ) & -\sin(2 \times 2^\circ) \\ \cos^2(60^\circ) & \sin^2(60^\circ) & -\sin(2 \times 60^\circ) \\ \cos^2(300^\circ) & \sin^2(300^\circ) & -\sin(2 \times 300^\circ) \end{pmatrix}. \quad (4)$$

4 Comparison of strain measurements

4.1 Strain transfer rate

By fitting the strainmeter data to the DAS data with a linear regression, we compute the ‘strain transfer rate’

$$r = \frac{\sum_k x_k y_k}{\sum_k y_k^2}, \quad (5)$$

where x_k is the DAS time series of ‘fiber strain’ and y_k is the strainmeter time series of ‘rock strain’. Data are filtered by a Butterworth high-pass (0.05 Hz, 4th order) and low-pass (0.1 Hz, 4th order). The average is thus removed from the signals prior to the computation. Fig. 2 (left) shows the ‘strain transfer rate’ r and Table 2 summarizes the ranges of values. They are between 0.13 and 0.53 in all cases and primarily depend on location and cable type. The variability in the values calculated for a single installation (i.e., one cable at one location) is depicted using a violin plot, where the edges illustrate the density of dots in Fig. 2.

The variability within individual violin plots is smaller than the differences between the median values for different cables and locations. This observation remains consistent across all considered installations, regardless of cable type or location. It underlines the significance of the differences observed between the installations. Differences between colocated fibers for the same cable, location, and event are smaller than 0.05 in almost all cases, which lets us rule out that fiber related causes (like optical fading) would dominate the observed differences. We find no discernible correlation of ‘strain transfer rate’ with signal amplitude, back-azimuth or other earthquake specific parameters (see Figs. S28 and S29 in the supplemental material for example).

The largest values of ‘strain transfer rate’ are found for the tight-buffered cable, which was expected. Although the loose-tube cable in the ‘Anton Gang’ is loaded down by sandbags as well, its ‘strain transfer rate’ is the lowest among all fibers. Hence, we do not observe a significant benefit from sand and sandbags to improve overall coupling.

4.2 Waveform similarity

The linear regression used to derive the ‘strain transfer rate’ requires that the ‘fiber strain’ waveform as recorded by DAS is consistent with the ‘rock strain’ waveform obtained from the strainmeters. We use the

normalized correlation coefficient

$$c = \frac{\sum_k x_k y_k}{\sqrt{\sum_k x_k^2} \sqrt{\sum_k y_k^2}} \quad (6)$$

as a measure of waveform similarity. Fig. 3 compares the P-waves radiated by the Mw 7.7 Pazarcık earthquake across all measurement types and illustrates differences in SNR. Fig. 2 (right) shows the distribution of the normalized correlation coefficients obtained for all tested configurations. They primarily depend on signal amplitude and thus on signal-to-noise ratio for the DAS data (see Fig. S33 in the supplemental material). The values are largest and larger than 0.92 for all signals of the Mw 7.7 and Mw 7.6 earthquakes of the Kahramanmaraş earthquake sequence (see Fig. S31 in the supplemental material). For the surface waves recorded by the tight-buffered cable in the ‘Anton Gang’ they are even larger than 0.99. The distribution shown in Fig. 2 (right) indicates a generally better signal quality for data recorded with the tight-buffered cable. The loose-tube cable, if not protected by sand-bags (‘Vorstollen’), appears to be prone to glitches caused by water drops (see Fig. S12 in the supplemental material for example).

The signal-to-noise ratio of the strainmeter generally is better than that of the DAS cables. This can be seen in Fig. 3, where the first P-wave arrival is clearly seen in the seismometer and strainmeter data at 50 s on the time scale. Only after 70 s the signal amplitude is large enough to allow the DAS recording to capture the P-waves. The high signal-to-noise ratio of the ‘rock strain’ allows the strainmeter signal to lock onto the ‘rock strain’-waveform in the DAS data in the linear regression. The high signal-to-noise ratio time series is in the denominator of Eq. (6) and thus there is no correlation between ‘strain transfer rate’ and normalized correlation coefficient found in the results.

4.3 Intercomparison of fibers at higher frequency

The comparison with strainmeter data is limited to frequencies below 0.1 Hz. Due to their short-period signal energy we can use the body-waves of the Kahramanmaraş earthquakes to extend the study to a larger frequency range by comparing the DAS signals of the main shocks (Mw 7.7 and Mw 7.6) with one another. Hence, the regression is computed with respect to recordings of read-out locations on the tight-buffered fibers. Fig. 4 shows the analysis results for a comparison between different fibers (all with respect to one of the tight-buffered fibers). The normalized correlation coefficients (waveform similarity) generally are higher than 0.970 and reach 1.000 for some of the combinations. At

frequencies above 1 Hz the signal-to-noise ratio for S-waves quickly drops because of the decrease of S-wave energy with increasing signal frequency. This results in reduced signal-to-noise ratio and thus waveform similarity and regression coefficients are reduced as well. A frequency dependence of regression factors beyond the scatter is not apparent up to 1 Hz.

In the frequency range up to 1 Hz, colocated fibers in the same cable practically pick up the same strain amplitude. Regression coefficients listed in Table 3 scatter about unity, where the scatter is smaller for the tight-buffered cable (smallest in the ‘Vorstollen’ with a range of 0.96 to 1.02) and largest for the loose-tube cable in the ‘Anton Gang’ (0.80 to 1.23). The ratios of ‘strain transfer rate’ given in Table 2 are consistent with the regression factors for colocated cables in the extended frequency range given in Table 3.

4.4 Comparison with seismometer data

Strainmeter installations recording at seismic frequencies are rare and available only in a few observatories. In the absence of strainmeters many studies use strain signals estimated from particle velocity recorded by seismometers, which appears possible for plane waves of known incidence and phase-velocity. The scaling relation is given by

$$\epsilon_{xx}(\mathbf{r}, t) = -s_h \cos(\psi_{BAZ} - \psi_x - 180^\circ) v_x(\mathbf{r}, t), \quad (7)$$

where v_x and ϵ_{xx} are horizontal particle velocity and linear strain in azimuth of ψ_x , respectively, $\psi_{BAZ} - 180^\circ$ is the azimuth of wave propagation, and s_h is the horizontal component of slowness (see section S4.1 in the supplemental material for additional details). The accuracy of the scaled seismometer signal in representing strain depends on the validity of the plane-wave assumption underlying the conversion. While strainmeters and DAS can be expected to record the same quantity, namely linear strain in a given azimuth, independent of the nature of the signal, this is not the case for the seismometer derived strain signals. This is not only the case because the recorded waveform is a superposition of non-plane waves with different phase slowness, but also because of the local free surface affecting the particle velocity and the strain in different ways (see section S2.5 in the supplemental material for additional details).

The signal derived from the STS-2 recording in Fig. 3 matches the strain signals quite well near the first P-wave arrival (75 s). In later parts (220 s) the P-wave signal of particle velocity obviously provides only half the amplitude of the signals from the strainmeter and the scaled DAS signals.

The surface waves with good signal-to-noise ratio used in the current study not only propagate at varying slowness (dispersion and superposition of Love-

and Rayleigh-waves), they also contain significant non-plane wavefield components due to scattering in particular on continental paths. Wielandt (1993) discusses the consequences of the non-plane nature of waves for the spatial derivatives of displacement. The scaling in Eq. (7) lets ϵ_{xx} vanish for ψ_{BAZ} being perpendicular to ψ_x . In cases where ψ_{BAZ} comes close to being perpendicular to ψ_x the actual strain component is dominated by off-great-circle propagation and non-plane wave contributions, which results in a large scatter of regression coefficients (see Fig. S34 in the supplemental material). In these cases, seismometers cannot reasonably be used to calibrate DAS signals.

Here, we illustrate the limitations of the comparison with seismometer data using the surface waves recorded on February 23rd 2023 after the Mw 6.8 earthquake in the the Tajikistan-Xinjiang Border Region. The great-circle backazimuth for this earthquake is $\psi_{BAZ} = N77.2^\circ E$, which is only by 17° off the direction perpendicular to the ‘Anton Gang’ azimuth of $\psi_x = N330^\circ E$. Fig. 5 (top panel) shows the signal comparison. Love-waves (300 s) and Rayleigh-waves (400 s) are inseparably superimposed. Both are dispersive and arrive at different phase velocity with non-plane wavefronts due to scattering on the continental path. Slowness $s_h = 280 \text{ ms km}^{-1}$ is used for scaling the seismometer signal, which corresponds to the average phase velocity of about 3.6 km s^{-1} , the value of Rayleigh-wave phase velocity at 0.05 Hz in Southern Germany (Friederich and Huang, 1996, their Table 1). The bottom panel of Fig. 5 shows the waveform residuals with respect to the strainmeter signal. The residual amplitude for the tight-buffered cable is about three to five times the noise level. For the seismometer the largest residual amplitude is five times larger and the waveform mismatch renders the seismometer signal unusable for a calibration. The adjustment of a scaling factor would not solve the problem. The seismometer derived amplitude for the first wave group (300 s – 500 s) is larger than that of strainmeter and DAS, while it is too small after 500 s. Additionally, Fig. 5 shows a significant mismatch throughout the wavetrain, while DAS and strainmeter waveforms are rather consistent. In practically all cases examined the normalized correlation coefficient between seismometer signal and DAS is smaller than between strainmeter signal and DAS (see Fig. S35 in the supplemental material). In most cases it is significantly smaller and in some cases it is even negative (anti-correlation).

5 Detection threshold for ‘rock strain’

The signal of largest amplitude in the natural seismic background are the marine microseisms. This can be a

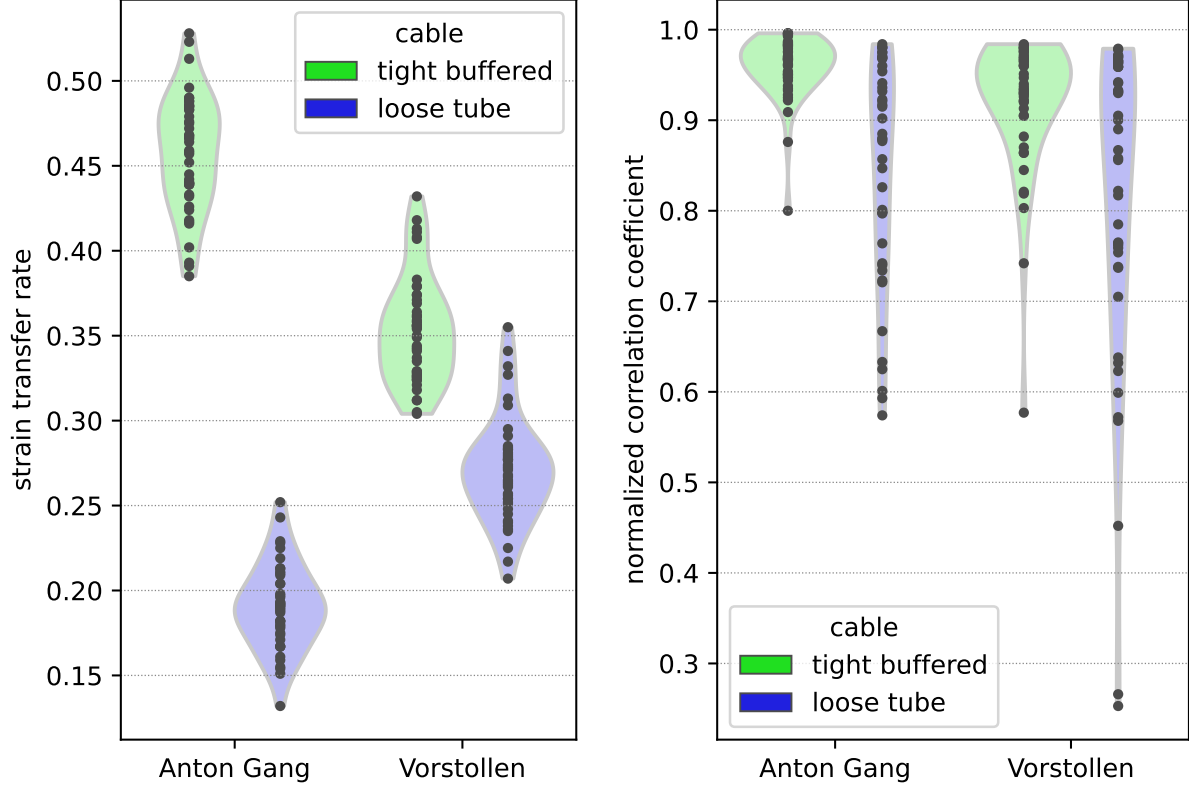


Figure 2: Values of ‘strain transfer rate’ (left diagram, representing the ratio of ‘fiber strain’ to ‘rock strain’ as recorded by the strainmeter) derived by Eq. (5) and the normalized correlation coefficients (right diagram) calculated using Eq. (6). The results are shown separately for two locations: ‘Anton Gang’ (left, N330°E) and ‘Vorstollen’ (right, N90°E). They are presented for two different cables: a tight-buffered (green, left) and a loose-tube cable (blue, right) at each location. These values are derived in two fibers per cable, for surface wave signals of 19 teleseismic earthquakes and the P- and S-wave signals of the two Turkey-events on 2023-02-06. All signals are consistently filtered with 4th order Butterworth high-pass (0.05 Hz) and low-pass (0.1 Hz) filters. For each set of cable and location, the black dots represent individual results from the 46 analyses and a summary of the values is provided in Table 2. The kernel density estimates that define the edges of the violin plot illustrate the spread in the distribution of numerical values.

Table 2: Ranges of ‘strain transfer rate’.

cable	location	minimum	median	maximum
tight-buffered	‘Anton Gang’	0.39	0.46	0.53
tight-buffered	‘Vorstollen’	0.30	0.35	0.43
loose-tube	‘Vorstollen’	0.21	0.27	0.36
loose-tube	‘Anton Gang’	0.13	0.19	0.25

Values are as presented in Fig. 2 (left). Strainmeter signals are fitted to DAS (distributed acoustic sensing) recorded waveforms by linear regression in the frequency band from 0.05 Hz to 0.1 Hz.

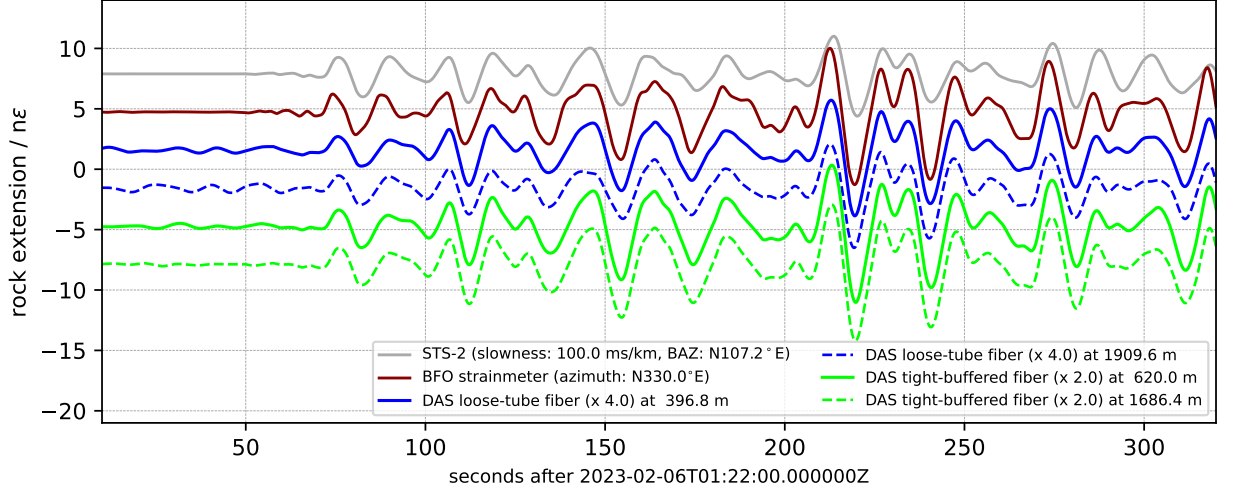


Figure 3: Waveforms of the P-waves radiated by the Mw 7.7 Pazarcık earthquake on February 6th, 2023. Traces are shifted vertically for better visibility. The legend (top to bottom, left to right) specifies the traces in order from top to bottom. All signals are consistently filtered with Butterworth high-pass (0.05 Hz, 4th order) and low-pass (0.1 Hz, 4th order) filters. The seismometer response is removed from the STS-2 data. The DAS signals of ‘fiber strain’ from the tight-buffered cable (green, signal amplified by a factor of 2) and the loose-tube cable (blue, signal amplified by 4) are taken with a gauge length of 50 m at a location in the center of the ‘Anton Gang’ (Fig. 1). Linear strain in azimuth N330°E of ‘Anton Gang’ is obtained from the BFO strainmeter array by Eq. (2). For comparison we show an estimate of linear strain simulated from ground velocity for a plane wave of slowness 100 ms km^{-1} and incoming from backazimuth N107.2°E. The basis for this simulation is the recording of the STS-2 seismometer converted by Eq. (7). The slowness of 100 ms km^{-1} , which acts as a scaling factor in Eq. (7) is not appropriate throughout the entire time window. This makes calibration with respect to strain simulated from ground velocity disputable. While the first P-wave onset is apparent near 01:22:50 UT (50 s on timescale) in the strainmeter and STS-2 data, the noise level in the DAS data is too high to detect the small amplitude signals before 01:23:10 UT (70 s).

Table 3: Ranges of regression coefficients for an intercomparison of fibers.

DAS with respect to colocated DAS fibers (in the same cable)	
tight-buffered ‘Vorstollen’	0.96 – 1.02
tight-buffered ‘Anton Gang’	0.92 – 1.08
loose-tube ‘Vorstollen’	0.89 – 1.11
loose-tube ‘Anton Gang’	0.80 – 1.23
DAS with respect to colocated DAS fibers (in the other cable)	
loose-tube vs. tight-buffered ‘Vorstollen’	0.72 – 0.83
loose-tube vs. tight-buffered ‘Anton Gang’	0.32 – 0.47

The presented values cover the frequency band from 0.05 Hz to 1.0 Hz.

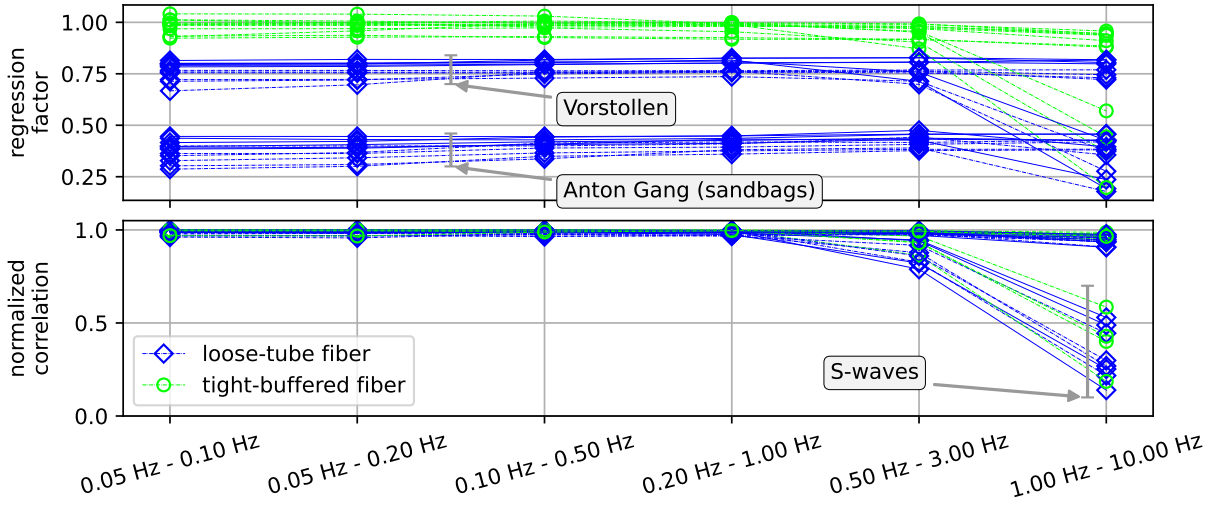


Figure 4: Regression factor derived by Eq. (5) and normalized correlation coefficient by Eq. (6) with respect to one colocated fiber in the tight-buffered cable (location 620.0 m in the ‘Anton Gang’ and 719.2 m in the ‘Vorstollen’, respectively, see Fig. 1). We use body-wave signals of both main shocks (Mw 7.7 and Mw 7.6) of the Kahramanmaraş earthquake sequence on February 6th 2023 for both locations, fibers and cables. The S-waves contain less short-period energy. The signal-to-noise ratio for them is reduced above 1 Hz, which results in a reduced waveform similarity (normalized correlation coefficient). This also affects the regression factors derived for S-waves. A summary of the values up to 1 Hz is given in Table 3.

helpful test signal for the investigation of instrumental properties at frequencies of 0.1 Hz to 1 Hz. In applications for Newtonian Noise mitigation the strain background at even smaller amplitude must be resolved.

We analyze the signals at times of large marine microseism amplitude. The rms-amplitude levels are shown in Fig. 6 (top) together with the pair-wise magnitude-squared coherence (Carter et al., 1973, their eq. 2) of signals (bottom). The signal of the BFO strainmeters shows the signature of the primary microseism peak at about 0.07 Hz as well as the secondary peak at 0.14 Hz. The tight-buffered cable appears to detect the secondary microseism peak, while the scaled noise in the loose-tube fibers is above the background ‘rock strain’ level. The coherence between the BFO strainmeter signal and the tight-buffered fibers (at 620.0 m and 1686.4 m), as well as among the tight-buffered fibers themselves, peaks at 0.8 at the frequency of the secondary microseisms, i.e. 0.14 Hz. The coherence for all other signal combinations reaches a maximum of 0.6 or less. The lower envelope of the coherence curves peaks at 0.3 at 0.14 Hz, which may indicate that all signals contain at least a portion of the marine microseisms. Nevertheless the similarity of the waveforms shown in Fig. 7 is not as good as for the earthquake signals, even though a narrow bandpass is applied. This is consistent with the coherence not exceeding a value of 0.8.

The amplitude levels of the marine microseisms at BFO strongly vary with weather conditions over the North Atlantic and are typically lower during northern hemisphere summer¹. A similar analysis for signals recorded on 2022-07-10 shows the background level of the BFO strainmeter recordings at below 0.02 nstrain with no indication of a microseism peak. At the same time, the amplitude levels of the DAS recordings range between 0.05 nstrain (0.3 Hz) and 0.4 nstrain (0.05 Hz), with the lowest levels observed for the tight-buffered fibers and rms values decreasing with increasing frequency for all fibers. Coherence between any pair of fibers, or between DAS recording and BFO strainmeter, is below 0.25 at these times. Thus, at times of low marine microseism amplitude, the DAS fibers are not able to pick up the background ‘rock strain’ in the discussed frequency band.

6 Conclusions

The waveform similarity between DAS- and strainmeter-recorded signals, as well as in the inter-comparison of DAS signals, is high for signals with large amplitudes. For the body- and surface waves recorded after the main shocks (Mw 7.7 and Mw 7.6) of the Kahramanmaraş earthquake sequence on February

¹The seasonal variation of marine microseism energy is seen in the analyses presented by the Waveform Quality Center at Lamont-Doherty Earth Observatory: https://www.ldeo.columbia.edu/~ekstrom/Projects/WQC/MONTHLY_HTML/BFO-II.LHZ-00_time.html.

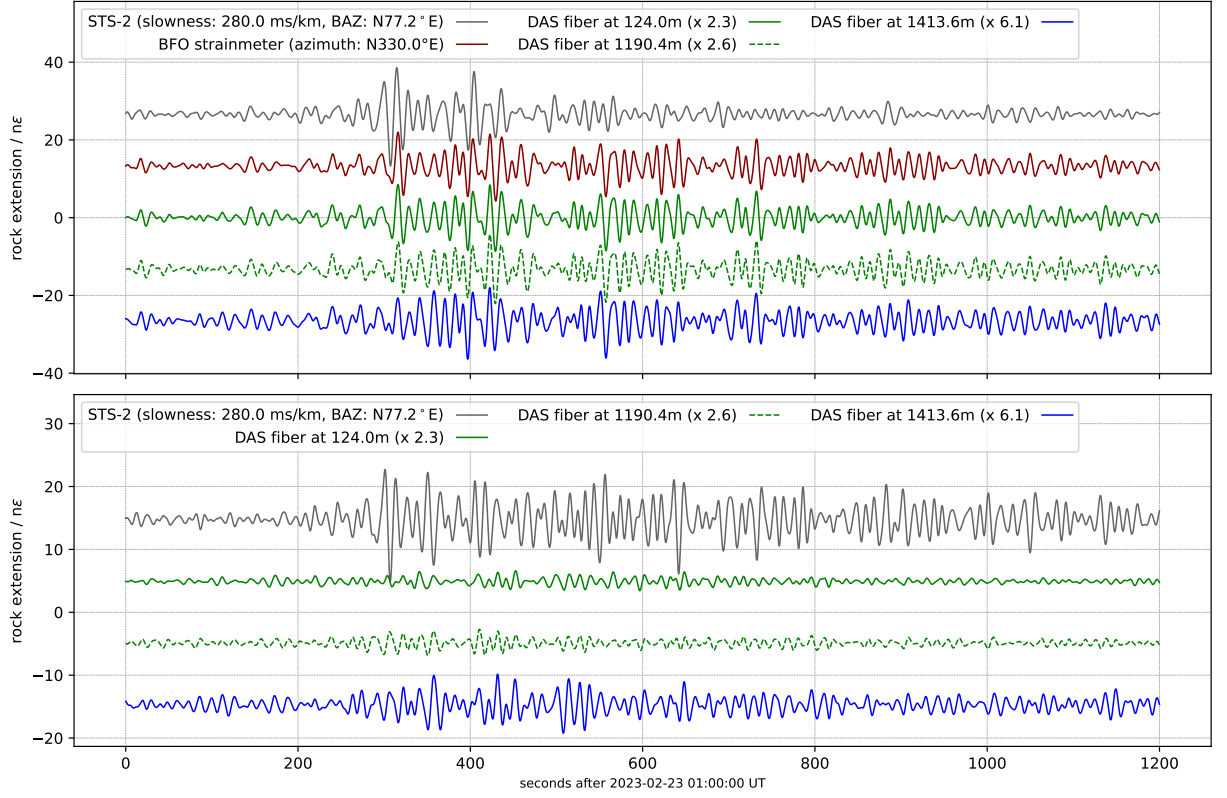


Figure 5: Surface waves (top) and residuals with respect to the strainmeter data (bottom) for the Mw 6.79 Tajikistan-Xinjiang Border Region earthquake (origin: 2023-02-23 00:37:39.01 UTC, 38.06°N , 73.29°E , 10.0 km depth, $\text{BAZ}=N77.24^{\circ}\text{E}$, $\Delta=47.06^{\circ}$). Traces are shifted vertically for better visibility. The legends (top to bottom, left to right) specify the traces in the order from top to bottom. Love-waves (300 s) and Rayleigh-waves (400 s) are inseparably superimposed. All direct body wave phases arrived prior to 1:00 UT (outside the displayed window). Displayed are strain signals for the azimuth $N330^{\circ}\text{E}$ (‘Anton Gang’). Top panel traces from top to bottom: gray: particle velocity scaled to apparent strain by Eq. (7) with $\psi_{\text{BAZ}} = N77.2^{\circ}\text{E}$ and slowness $s_h = 280 \text{ ms km}^{-1}$. The backazimuth is only by 17° off the direction perpendicular to the ‘Anton Gang’ azimuth of $\psi_x = N330^{\circ}\text{E}$. red: BFO strainmeters. green solid, green dashed: tight-buffered DAS cable (read-out locations 124.0 m and 1190.4 m). blue: loose-tube DAS cable (1413.6 m). The DAS signals are scaled to minimize the rms-residual with respect to the strainmeter (factors are given in the legend). Bottom panel: Waveform difference of the traces in the top panel with respect to the strainmeter signal.

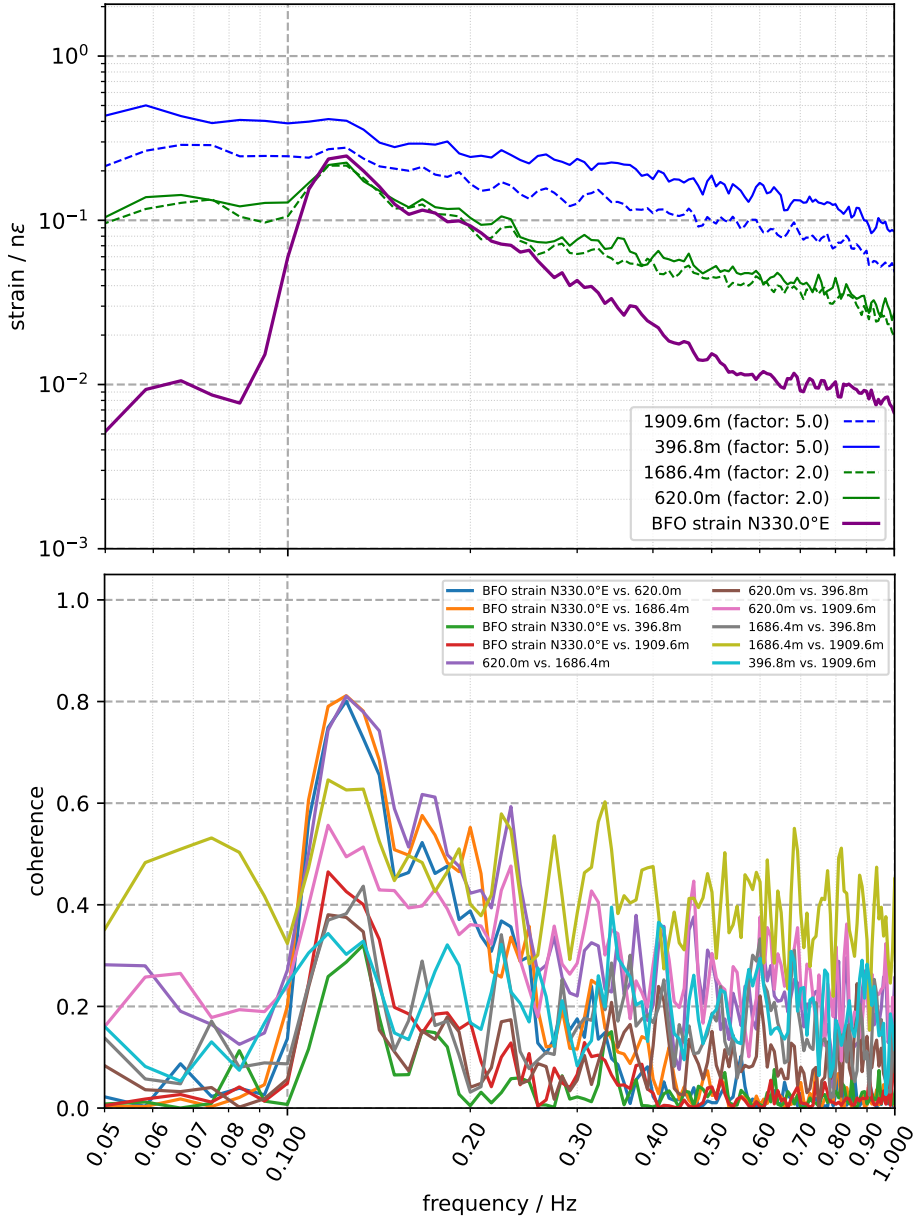


Figure 6: Analyses of the strain background signal in the ‘Anton Gang’ for 50 minutes after 2023-01-08 0:40 UT at times of large marine microseism amplitude. Top: rms-amplitude in 1/6 decade. The peaks of the primary (0.07 Hz) and secondary (0.14 Hz) microseisms are observed in the BFO strainmeter data. DAS recorded signals are multiplied by the average reciprocal ‘strain transfer rate’ as given in Table 3. The values from the loose-tube cable (1909.6 m and 396.8 m) are largest. The values for the BFO strainmeter are the smallest below 0.1 Hz and above 0.25 Hz. At 0.14 Hz the curves for the tight-buffered cable (1686.4 m and 620.0 m) coalesce with the curve for the BFO strainmeter. Bottom: magnitude-squared coherence of pairs of signals. The curves for the BFO strainmeter versus the tight-buffered cable (620.0 m and 1686.4 m) and the intercomparison of the tight-buffered fibers (620.0 m versus 1686.4 m) have a peak value of 0.8 at 0.14 Hz. Values for all other pairs are smaller at this frequency.

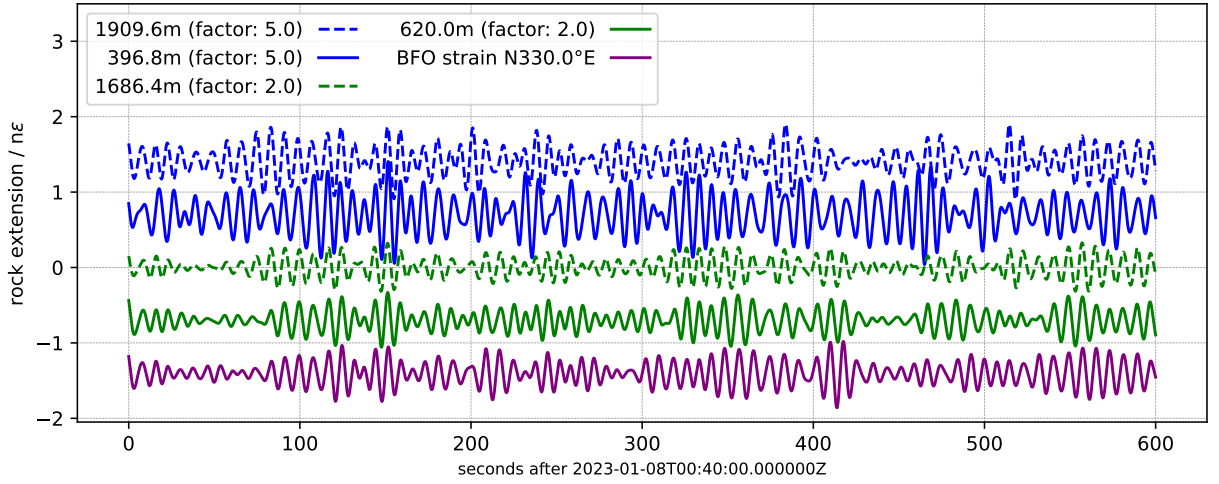


Figure 7: Waveforms of the recorded background signal at large amplitudes of marine microseisms. Traces are shifted vertically for better visibility. The legend (top to bottom, left to right) specifies the traces in order from top to bottom. Read-out locations 1909.6 m and 396.8 m are from the loose-tube cable and locations 1686.4 m and 620.0 m are from the tight-buffered cable, both in the ‘Anton Gang’. A narrow bandpass from 0.1 Hz to 0.16 Hz is applied in order to focus on the signal of the secondary microseisms. DAS recorded signals are multiplied by the average reciprocal ‘strain transfer rate’ as given in Table 2.

6th 2023 the normalized correlation coefficient (NCC) with respect to the strainmeter is larger than 0.92 for all DAS fibers in the frequency band from 0.05 Hz to 0.1 Hz. In an intercomparison of colocated DAS fibers for the body-wave signals up to 1 Hz, the NCC is larger than 0.97 and reaches 1.000 in some cases. For smaller signal amplitude the DAS signal-to-noise ratio worsens and the NCC becomes smaller. The signal quality in this respect is better for the tight-buffered cable and worst for the loose-tube cable in the ‘Vorstollen’, where it is not protected by a sand bed against water dripping from the ceiling.

The DAS recorded ‘fiber strain’ at large amplitude hence well represents the waveform and the signal phase of ‘rock strain’. This is, however, not the case for the signal amplitude. The values of ‘strain transfer rate’ (amplitude ratio of ‘fiber strain’ versus ‘rock strain’), which we calibrate by linear regression, cover a range from 0.13 to 0.53 (Table 2). None of the installed cables provides a ‘strain transfer rate’ equal 1, which would make ‘fiber strain’ equal ‘rock strain’. The largest value is obtained for the tight-buffered cable in the ‘Anton Gang’, where cables are loaded down by loose sand and sand bags. While the tight-buffered cable generally provides a larger ‘strain transfer rate’, the smallest values are obtained for the loose-tube cable in the ‘Anton Gang’. We hence find no consistent effect of the sand bags on coupling the fiber to the rock.

The scatter in ‘strain transfer rate’ values for a single cable at one location is smaller than the differences observed between different cables and locations. By the

high similarity of signals from two fibers in the same cable, we can rule out fiber related causes for the difference, like optical fading. We find no systematic dependency of ‘strain transfer rate’ on backazimuth of the event, nor do we find any other systematic correlation except with respect to cable type and location. The ‘strain transfer rate’ of the cables cannot be specified independently of local installation conditions.

An amplitude correction factor to be applied to DAS recorded strain not only adjusts the signal amplitude, but also amplifies the instrument generated background noise. Consequently the peak of the secondary marine microseisms is only detected by the installation with largest ‘strain transfer rate’ in Table 3. We estimated the detection threshold for the tight-buffered cable in the ‘Anton Gang’ at 0.1 nstrain rms-amplitude in 1/6 decade near 0.1 Hz.

Even if we attribute the ‘strain transfer rate’ to the cable type and installation here, we cannot rule out the possibility that some other effect reduces the recorded ‘fiber strain’. In a next step, we plan to install a testbed of fibers (just core, cladding, coating, and tight-buffer) directly cemented into the floor of the mine. We expect that this would make the DAS recordings more sensitive and would make ‘fiber strain’ equal ‘rock strain’.

Data and Resources

All data were recorded locally at (Black Forest Observatory [BFO], 1971, <https://dx.doi.org/10.5880/>

BFO). Strainmeter and seismometer data are available through data centers at the (Scripps Institution of Oceanography, 1986, <https://dx.doi.org/10.7914/SN/II>) and the (Federal Institute for Geosciences and Natural Resources, BGR, 1976, <https://dx.doi.org/10.25928/MBX6-HR74>), respectively. DAS data can be provided upon request. Event parameters were taken from the GEOFON catalog (Quinteros et al., 2021, <https://geofon.gfz-potsdam.de/eqinfo/>). Data analysis was carried out with ObsPy (The ObsPy Development Team, 2022, <https://dx.doi.org/10.5281/zenodo.6327346>). We provide a supplemental text file with figures, tables, and math to further support the findings presented in this paper.

Acknowledgments

We thank Peter Duffner for taking care of the BFO strainmeters and their calibration devices. We are grateful to Walter Zürn for many fruitful discussions and his continuing support of the operation of the Invar-wire strainmeters. Gaetan Calbris and Vincent Lanticq from Febus Optics provided helpful information on the measurement principle used in the Febus A1-R. Peter Duffner, Felix Bögelspacher, and Leon Merkel supported the installation of the experiment. We are grateful for the well-considered comments provided by two anonymous reviewers. The cable with the tight-buffered fibers (green cable) has been made available for the experiments through the INSIDE project. INSIDE is supported by the German Federal Ministry for Economic Affairs and Climate Action and the Project Management Jülich (PtJ) under the grant agreement number 03EE4008C.

References

- Agnew, D. C. (1986). Strainmeters and tiltmeters. *Rev. Geophys.* **24**(3), 579–624. doi: 10.1029/RG024i003p00579.
- Azzola, J., N. K. Toularoud, E. Gaucher, T. Forbriger, R. Widmer-Schmidrig, F. Bögelspacher, M. Frietsch, and A. Rietbrock (2022). Comparison between distributed acoustic sensing (DAS) and strainmeter measurements at the Black Forest Observatory. In *EGU General Assembly 2022*. doi: 10.5194/egusphere-egu22-6976.
- Baker, T. and G. Lennon (1973). Tidal tilt anomalies. *Nature* **243**, 75–76. doi: 10.1038/243075a0.
- Black Forest Observatory [BFO] (1971). Black Forest Observatory data. doi: 10.5880/BFO.
- Carter, G., C. Knapp, and A. Nuttall (1973). Estimation of the magnitude-squared coherence function via overlapped fast Fourier transform processing. *IEEE Trans. Audio and Electroacoustics* **21**(4), 337–344. doi: 10.1109/TAU.1973.1162496.
- Dakin, J. P. (1990). Distributed optical fibre sensors. In *OFS-7: Conference on Optical Fiber Sensors (02/12/90 - 06/12/90)*. <https://eprints.soton.ac.uk/77464/> (last accessed: 2023-12-07).
- Emter, D., H.-G. Wenzel, and W. Zürn (1994). The Black Forest Observatory, Schiltach. *Soil Dynamics and Earthquake Engineering* **13**(1), 73–75. doi: 10.1016/0267-7261(94)90043-4.
- Emter, D. and W. Zürn (1985). Observations of local elastic effects on earth tide tilts and strains. In J. C. Harrison (Ed.), *Earth Tides*, Chapter 14, pp. 309–327. New York: Van Nostrand Reinhold Company.
- ET Steering Committee (2020). Einstein Telescope design report update 2020. available from European Gravitational Observatory, document number ET-0007B-20.
- Federal Institute for Geosciences and Natural Resources, BGR (1976). German Regional Seismic Network (GRSN). doi: 10.25928/MBX6-HR74.
- Forbriger, T., R. Widmer-Schmidrig, L. Hillmann, H. Xiao, A. Rietbrock, V. R. Tribaldos, A. Strollo, and P. Jousset (2024). Cemented fibers as a test-bed for distributed acoustic sensing (das). In *AG Seismologie, 50th annual conference*, Hamburg.
- Friederich, W. and Z.-X. Huang (1996). Evidence for upper mantle anisotropy beneath southern Germany from Love and Rayleigh wave dispersion. *Geophys. Res. Lett.* **23**(10), 1135–1138. doi: doi.org/10.1029/96GL01216.
- Harms, J. (2015). Terrestrial gravity fluctuations. *Living Rev. Relativ.* **18**(3). doi: 10.1007/lrr-2015-3.
- Harms, J., L. Naticchioni, E. R. D. R. Calloni, F. Ricci, and D. D’Urso (2022). A lower limit for Newtonian-noise models of the Einstein Telescope. *Eur. Phys. J. Plus* **137**(687). doi: 10.1140/epjp/s13360-022-02851-z.
- Harrison, J. C. (1976). Cavity and topographic effects in tilt and strain measurement. *J. Geophys. Res.* **81**(2), 319–328. doi: 10.1029/JB081i002p00319.
- Hartog, A. H. (2017). *An Introduction to Distributed Optical Fibre Sensors* (1 ed.). CRC Press. doi: 10.1201/9781315119014.

- Kennett, B. L. N. (1991). The removal of free surface interactions from three-component seismograms. *Geophys. J. Int.* **104**(1), 153–163. doi: 10.1111/j.1365-246X.1991.tb02501.x.
- King, G. and R. Bilham (1973). Tidal tilt measurement in europe. *Nature* **243**, 74–75. doi: 10.1038/243074a0.
- King, G. and R. Bilham (1976). A geophysical wire strainmeter. *Bull. Seismol. Soc. Am.* **66**(6), 2039–2047. doi: 10.1785/BSSA0660062039.
- Li, D., H.-N. Li, L. Ren, and G. Song (2006, February). Strain transferring analysis of fiber bragg grating sensors. *Optical Engineering* **45**(2), 024402–. doi: 10.1117/1.2173659.
- Li, Y., M. Karrenbach, and J. B. Ajo-Franklin (2021). A literature review. In *Distributed Acoustic Sensing in Geophysics*, pp. 229–291. American Geophysical Union (AGU). doi: 10.1002/9781119521808.ch17.
- Lindsey, N. J. and E. R. Martin (2021). Fiber-optic seismology. *Annu. Rev. Earth Planet. Sci.* **49**(1), 309–336. doi: 10.1146/annurev-earth-072420-065213.
- Lindsey, N. J., H. Rademacher, and J. B. Ajo-Franklin (2020). On the broadband instrument response of fiber-optic DAS arrays. *J. Geophys. Res.* **125**(2), e2019JB018145. doi: doi.org:10.1029/2019JB018145.
- Longman, I. M. (1959). Formulas for computing the tidal accelerations due to the moon and the sun. *J. Geophys. Res.* **64**(12), 2351–2355. doi: 10.1029/JZ064i012p02351.
- Melchior, P. (1966). *The earth tides* (1. ed. ed.). Oxford: Pergamon Press.
- Melchior, P. (1978). *The tides of the planet Earth* (1. ed. ed.). Oxford: Pergamon Press.
- Melgar, D., T. Taymaz, A. Ganas, B. Crowell, T. Öcalan, M. Kahraman, V. Tsironi, S. Yolsal-Çevikbilen, S. Valkaniotis, T. S. Irmak, T. Eken, C. Erman, B. Özkan, A. H. Dogan, and C. Altuntaş (2023). Sub- and super-shear ruptures during the 2023 Mw 7.8 and Mw 7.6 earthquake doublet in SE Türkiye. *Seismica* **2**(3), 10. doi: 10.26443/seismica.v2i3.387.
- Paitz, P., P. Edme, D. Gräff, F. Walter, J. Doetsch, A. Chalari, C. Schmelzbach, and A. Fichtner (2020). Empirical investigations of the instrument response for distributed acoustic sensing (DAS) across 17 octaves. *Bull. Seismol. Soc. Am.* **111**(1), 1–10. doi: 10.1785/0120200185.
- Pan, Z., K. Liang, Q. Ye, H. Cai, R. Qu, and Z. Fang (2011). Phase-sensitive OTDR system based on digital coherent detection. In *2011 Asia Communications and Photonics Conference and Exhibition (ACP)*, pp. 1–6. doi: 10.1117/12.905657, ISSN: 2162-1098.
- Quinteros, J., A. Strollo, P. L. Evans, W. Hanka, A. Heinloo, S. Hemmleb, L. Hillmann, K.-H. Jäkel, R. Kind, J. Saul, T. Zieke, and F. Tilmann (2021). The GEOFON program in 2020. *Seism. Res. Lett.* **92**(3), 1610–1622. doi: 10.1785/0220200415.
- Rademacher, H. (2024, 02). Is the era of broadband seismometry coming to an end? *Seism. Res. Lett.* **95**(3), 1467–1468. doi: 10.1785/0220240007.
- Reinsch, T., T. Thurley, and P. Jousset (2017). On the mechanical coupling of a fiber optic cable used for distributed acoustic/vibration sensing applications—a theoretical consideration. *Measurement Science and Technology* **28**(12), 127003. doi: 10.1088/1361-6501/aa8ba4.
- Scripps Institution of Oceanography (1986). Global Seismograph Network - IRIS/IDA. doi: 10.7914/SN/II.
- Taylor, H. F. and C. E. Lee (1993). Apparatus and method for fiber optic intrusion sensing. <https://patents.google.com/patent/US5194847A/en> (last accessed: 2023-12-07), US patent no. 5194847A.
- The ObsPy Development Team (2022, March). ObsPy 1.3.0. doi: 10.5281/zenodo.6327346.
- Verbaandert, J. (1959). Etalonnage des pendules horizontaux par crapaudine dilatable étudiée interférométriquement. In *IIIème Symp. Marées Terr.*, Trieste, pp. 81–90. Observatoire royal de Belgique.
- Verbaandert, J. (1962). L'étalonnage des pendules horizontaux. *Boll. Geofis.* **4**(16), 419–446. Bolletino di Geofisica Teorica ed Applicata.
- Verbaandert, J. (1963). L'étalonnage des pendules horizontaux. *Comm. Obs. Roy. Belg., S. Géoph., No. 62* **214**, 419–446.
- Wielandt, E. (1993, 04). Propagation and Structural Interpretation of Non-Plane Waves. *Geophys. J. Int.* **113**(1), 45–53. doi: 10.1111/j.1365-246X.1993.tb02527.x.
- Zürn, W. (2012). Strainmeters. In P. Bormann (Ed.), *New Manual of Seismological Observatory Practice 2 (NMSOP2)* (2 ed.), Technical report Information Sheet 5.1, pp. 1–11. Potsdam, Germany: GeoForschungsZentrum. doi: 10.2312/GFZ.NMSOP-2.IS.5.1.

Zürn, W., A. M. G. Ferreira, R. Widmer-Schmidrig, K. Lentas, L. Rivera, and E. Clévéde (2015). High-quality lowest-frequency normal mode strain observations at the Black Forest Observatory (SW-Germany) and comparison with horizontal broadband seismometer data and synthetics. *Geophys. J. Int.* **203**(3), 1787–1803. doi: 10.1093/gji/ggv381.

Electronic supplement to *Calibration of the strain amplitude recorded with DAS using a strainmeter array*

Thomas Forbriger, Jérôme Azzola, Nasim Karamzadeh,
Emmanuel Gaucher, Rudolf Widmer-Schmidrig, Andreas Rietbrock

Introduction

This electronic supplement introduces additional information and diagrams that are not essential to an understanding of the manuscript, but provide further insight into the data analysis and support the results of the study.

The supplementary material focuses first on the recording environment. It details the position of the DAS read-out locations in the ‘Anton Gang’ and ‘Vorstollen’ and the extent of the associated gauges on the floor of the gallery (Sec. S1.1 ‘Location of sensing points and gauges in the mine’). It also details the characteristics of the fiber optic cables used in the study (Sec. S1.2 ‘Specifications of optical fibers’).

The supplement gives then further details about the 19 earthquakes used to carry out a waveform comparison in the main study. In Section S2.1 ‘Earthquakes used in the analysis’, earthquake parameters for all 19 events are detailed. We show the DAS and strainmeter surface wave signals corresponding to each event, for read-out locations in ‘Anton Gang’ and ‘Vorstollen’ (Sec. S2.2.1 ‘Surface wave signals’). For the two Kahramanmaraş earthquakes, we also include the body wave data (Sec. S2.2.2 ‘Body wave signals’). We complement the discussion in Section S2 ‘Analyzed data’ by details on the pre-processing of DAS data in section S2.3 ‘Reduction of coherent noise’. Section S2.4 ‘Calibration of the strainmeters’ provides information on the calibration of the BFO strainmeters and section S2.5 ‘Distortion of the strain field due to local heterogeneity’ adds considerations on strain-strain coupling.

Extended results are then introduced to support the main findings of the study (Sec. S3 ‘Additional diagrams to complement the main results’). They focus on the analysis of ‘strain transfer rate’ (shortened to STR), which quantifies how much of ‘rock strain’ is transferred to the signal recorded by the IU, and on normalized correlation coefficients (shortened to NCC), which quantify the waveform similarity between the two strain measurements. We assess the correlation between

STR and NCC and evaluate the symmetry of the regression matrix, analyzing differences in fitting strainmeter data against DAS data or the opposite. The correlation of NCC and STR to earthquake parameters, including backazimuth and observed maximum strain, is also evaluated.

Section S4 ‘Plane wave strain from seismometer recordings’ gives further insight into the comparison of DAS recordings to strain signals computed from seismometer data. Section S4.1 ‘Scaling rule for plane waves’ details the procedure used for the conversion from particle velocity to strain and Sec. S4.2 ‘Regression with respect to seismometer data’ compares the regression coefficients computed when fitting strainmeter signals to DAS signals with those obtained by fitting scaled seismometer data to DAS. Seismometer and strainmeter data are finally compared in Sec. S4.3 ‘Comparison of seismometer and strainmeter data’.

Pre-processing

Signal pre-processing is carried out following the procedure described in the main paper. All signals shown in the supplemental material are band-pass filtered between 0.05 Hz and 0.1 Hz, where the DAS signal-to-noise ratio is good enough and strainmeter signals are free from parasitic components.

S1 Fiber Optic Cable setting

S1.1 Location of sensing points and gauges in the mine

Table S1 details the position of the read-out locations identified near the centers of ‘Anton Gang’ and ‘Vorstollen’. The read-out locations shown in the Figs. S1 and S2 are the ones used in the study.

DAS strain is computed over so-called gauges, defined by the gauge length (GL) parameter, which cor-

respond to the length of optical fiber over which optical dephasing is measured by the IU. The extent of the gauge on the cable plays therefore a significant role in the measured strain. The gauge-sections are displayed in detail in Figs. S1 and S2 for this reason. Fig. S2 applies to the modified cable setup, after February 7, 2023. For each read-out location considered in the analysis on ‘Anton Gang’ and ‘Vorstollen’, the physical location of the sensing point is represented as a symbol with the cable offset indicated in the legend, and the extent of the gauge is represented as a colored line.

The read-out locations were selected because of their position, near the center of ‘Anton Gang’ and ‘Vorstollen’. The figures show the small distance between the read-out locations positioned in each section of interest. It shows also that the associated gauges cover these sections with a consistent azimuth.

S1.2 Specifications of optical fibers

The analysis explores the capacities of two fiber optic cables with different characteristics. We use on one hand a standard flexible telecommunication cable with loose-tube fibers embedded in gel (blue cable on the diagrams). It is distributed by Prysmian Group. The print on the cable is:

DRAKA UC FIBRE I/O CT LSHF 3.0kN 4 SM2D
G.652.D/SM7A1 BendBright 60011347 15 20506485
009201015.

On the other hand, we use a second cable that has a stiff jacket containing tight-buffered fibers (green cable in the diagrams). It is distributed by Solifos AG and specified as a ‘BRUsens DAS & DTS & Communication Hybrid’ cable. For distributed acoustic sensing, we use two 2.4 mm simplex elements with tight-buffered single mode fiber with Aramid, glass strain relief and plastic outer sheath. The print on the cable is:

BRUSENS ACOUSTIC TEMPERATURE HYBRID BSAH
2SMF+2MMF+10SMF FIBRE OPTIC CABLE 00241904.

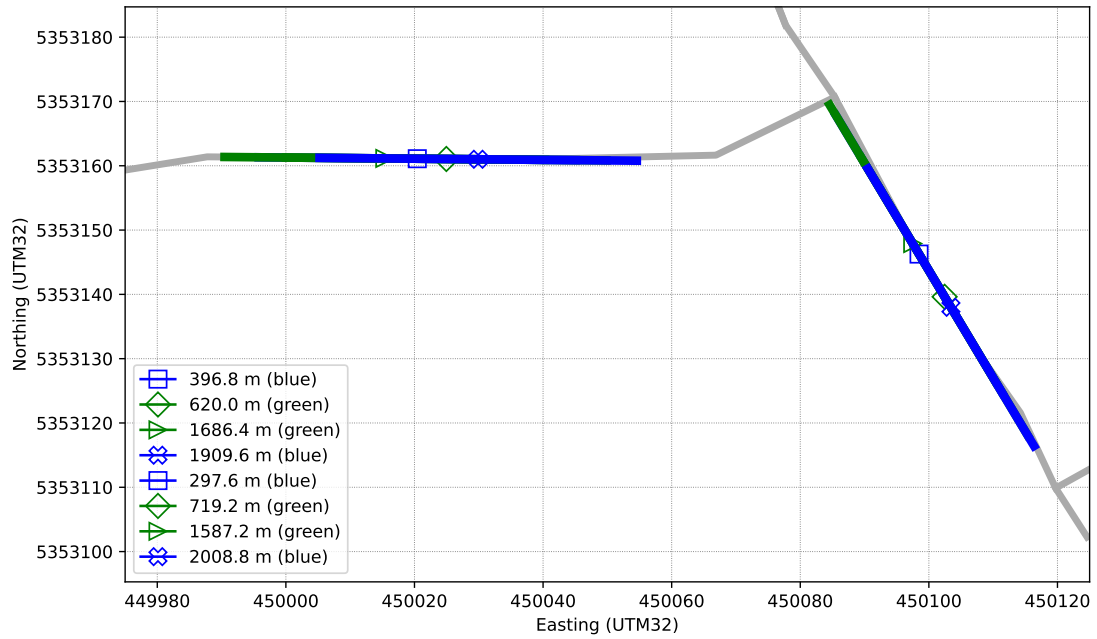


Figure S1: Floor map of the gallery of the mine with a zoom on the ‘Anton Gang’ (70 m long, azimuth N330°E) and on the ‘Vorstollen’ (80 m long, azimuth N90°E). It includes the extent of the gauge length, i.e. the optical fiber length over which optical dephasing is measured to produce a single sensing point located at the middle. The associated symbol shows the position of the measurement, as estimated by tap-tests. The figure includes the gauge lengths used for the study, considering the cable setup used in the mine from May 20, 2022 to February 7, 2023.

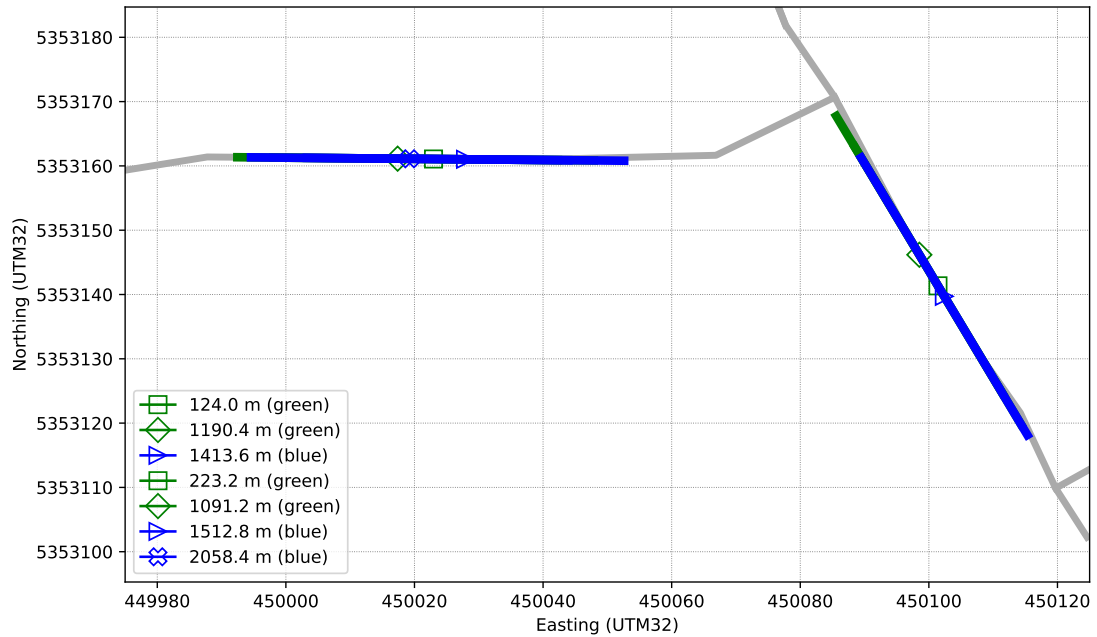


Figure S2: Same as previous figure, for the cable setup used in the mine from February 7 to March 13, 2023.

Table S1: Read-out locations along the fiber near the centers of ‘Anton Gang’ and ‘Vorstollen’ (see Figs. S1 and S2). The locations are specified by the linear distance from the IU (interrogation unit) along the fiber route.

‘Anton Gang’ (azimuth N330°E)			
cables covered with sand and sandbags			
UTM32N			
location / m	cable	easting / m	northing / m
396.8	loose-tube	450102.6	5353139.4
620.0	tight-buffered	450098.3	5353146.5
1686.4	tight-buffered	450101.6	5353141.0
1909.6	loose-tube	450099.3	5353144.9

‘Vorstollen’ (azimuth N90°E)			
UTM32N			
location / m	cable	easting / m	northing / m
297.6	loose-tube	450028.3	5353161.0
719.2	tight-buffered	450017.0	5353161.1
1587.2	tight-buffered	450023.4	5353161.1
2008.8	loose-tube	450022.0	5353161.1

‘Anton Gang’ (azimuth N330°E) after 2023-02-07			
UTM32N			
location / m	cable	easting / m	northing / m
124.0	tight-buffered	450101.4	5353141.4
1190.4	tight-buffered	450098.5	5353146.2
1413.6	loose-tube	450102.4	5353139.7

‘Vorstollen’ (azimuth N90°E) after 2023-02-07			
UTM32N			
location / m	cable	easting / m	northing / m
223.2	tight-buffered	450023.0	5353161.1
1091.2	tight-buffered	450017.4	5353161.1
1512.8	loose-tube	450027.9	5353161.0
2058.4	loose-tube	450019.3	5353161.1

‘Drum’	
location / m	cable
857.5	tight-buffered, drum start
1150.0	tight-buffered, drum center
1442.5	tight-buffered, drum end

‘Drum’ after 2023-02-07	
location / m	cable
367.5	tight-buffered, drum start
660.0	tight-buffered, drum center
952.5	tight-buffered, drum end

S2 Analyzed data

S2.1 Earthquakes used in the analysis

Table S2 details the seismic events used in the analysis with the main source parameters, which are taken from the GEOFON catalog. From the GEOFON catalog (Quinteros et al., 2021) we find 84 earthquakes with moment magnitude larger than 6 in the recording time period. For 21 of them, we measure a maximum strain amplitude larger than 1 nstrain in a visual inspection of strainmeter data, which is considered large enough to provide a sufficient signal-to-noise ratio in the DAS data. For 19 of these events, DAS data is available and allows an analysis. The largest amplitudes are found in the surface wave train. For body waves, the horizontal strain amplitude decreases as the ray incidence becomes steeper.

The table details the backazimuth (BAZ) and epicentral distance (Δ) that are given with respect to BFO (48.33°N, 8.33°E), as well as the maximum strain amplitude associated with surface wave signals, A_{\max} . The latter is visually read from the strainmeter data and should be understood as a proxy of the actual maximum signal amplitude in the analysis.

S2.2 Strain waveforms

In Figs. S3 to S25 we display waveforms of the analyzed data. All signals are consistently filtered with Butterworth high-pass (0.05 Hz, 4th order) and low-pass (0.1 Hz, 4th order) filters. Where STS-2 data is shown, the seismometer response is equalized to the response of the strain signals. Traces are shifted vertically for better visibility.

The DAS signals from the tight-buffered cable (green) and the loose-tube cable (blue) are taken with a gauge length of 50 m at a location in the center of the ‘Anton Gang’ and the ‘Vorstollen’, respectively (see Table S1 and Figs. S1 and S2). Linear strain in azimuth N330°E of ‘Anton Gang’ and azimuth N90°E of ‘Vorstollen’ is obtained from the BFO strainmeter array like explained in the main paper.

S2.2.1 Surface wave signals

Figures S3 to S21 detail the surface wave signals of the 19 events used in the manuscript to compare the DAS recorded ‘fiber strain’ with the strainmeter recorded ‘rock strain’. The figures focus on an ad-hoc waveform comparison of surface waves for linear strain in the direction of ‘Anton Gang’ (top) and ‘Vorstollen’ (bottom). Details about the analyzed frequency band, the event origin time and beam parameters are included in the caption.

S2.2.2 Body wave signals

For the large amplitude signals of the two main shocks (Mw 7.7 and Mw 7.6) of the Kahramanmaraş earthquake sequence, we also analyze the body wave signals. The body-wave signals of the Mw 7.7 Pazarcık earthquake are displayed for the ‘Anton Gang’ in Fig. S22 and in Fig. S23 for the ‘Vorstollen’. The surface wave signals are shown in Fig. S6. The corresponding diagrams for the Mw 7.6 Ekinözü earthquake are shown in Figs. S24, S25, and S5.

S2.3 Reduction of coherent noise

The Febus A1-R recordings contain a significant component of coherent noise at frequencies below 0.5 Hz. Lindsey et al. (2020, their section 2.6 Optical Noise) attribute this type of noise to vibrations of the optoelectronic system.

Other studies use the average over all recorded channels to capture the coherent component of noise. This relies on the earthquake signal not being coherent (because of propagation delay and varying orientation of the fiber), such that it more or less cancels out in the average and the earthquake signal in a single channel is not deteriorated by subtracting the average over all channels.

We follow a different approach. The idea behind using the reference coil on the drum is, that this section of the fiber is sufficiently decoupled from the rock and hence does not pick up a signal of the teleseismic earthquakes. For this reason it can be subtracted without affecting the amplitude of the earthquake signal.

In Figs. S26 and S27 we demonstrate this with the recordings of the Mw 7.7 Pazarcık earthquake. This is the earthquake which produced the by far largest strain amplitudes in the set of analyzed earthquakes. Even for the large amplitude surface waves, no signature of the earthquake signal is present in the recording from the reference coil (center diagram in Fig. S27). If a fraction of the earthquake signal should be hidden in the coherent noise on the reference drum, its amplitude is reduced to below 1.5 per cent of the full signal.

The P-wave signal of the earthquake becomes only apparent after this type of correction is applied, as shown in Fig. S26.

S2.4 Calibration of the strainmeters

The strainmeters operated at BFO are Invar-wire strainmeters of the design by King and Bilham (1976). Agnew (1986) and Zürn (2012) discuss instruments of this type and their properties. These instruments are primarily designed to record very-long period signals, such as tidal strain or Earth’s free oscillations. For the analysis of tidal strain amplitudes instrument calibration is of

utmost importance. The original calibration of the instruments was based on separate calibrations of several components, which then were put in series. In unfortunate cases the individual calibration inaccuracies added up constructively, which resulted in an unacceptable inaccuracy for the entire strainmeter.

For this reason an in-situ calibration mechanism for these instruments was developed at BFO, based on so-called 'Crapaudines', which provides an accuracy of about 2 per cent. They were originally used by Verbaandert (1959, 1962, 1963) in the calibration of tiltmeters. This application is described by Melchior (1966, pages 161 to 166), Melchior (1978, his section 8.8) and Agnew (1986, his section 4.1.5). Melchior (1966) calls them 'Expandable bearing plates of Verbaandert'. Agnew (1986) calls them 'distensible support of Verbaandert'. The 'Crapaudines' themselves are calibrated interferometrically (Verbaandert, 1959, 1962) and are used to impose a well defined motion on the fixed end of the wire in the strainmeter. The calibration factors of a few 'Crapaudines' used at BFO were confirmed by an independent interferometric measurement.

Because calibrations disturb the long-term tidal recordings, the stability of the calibration is occasionally tested by a comparison against theoretical tidal strain (Longman, 1959). This way we ensure a calibration accuracy and stability of about 5 per cent. Zürn et al. (2015) documented an episode of unstable calibration during the 2011 Tōhoku earthquake and how this was resolved. They were able to obtain strain amplitudes for radial mode ${}_0S_0$, which were consistent with Earth's radius and the observed radial surface motion within 15 per cent after the 2004 Sumatra-Andaman earthquake (their table 2).

The STR cannot be more accurate than the strainmeter calibration. The variation of STR between locations and cable type, however, cannot be due to limited calibration accuracy. This is because the differences exceed the level of 5 per cent and because the STR for the blue cable is larger in the 'Anton Gang' than in 'Vorstollen', while it is the opposite for the green cable, which cannot be caused by a calibration bias in principle.

S2.5 Distortion of the strain field due to local heterogeneity

Strain measurements and tilt measurements both are affected by local heterogeneity, sometimes called 'cavity effects'. This was first reported by King and Bilham (1973) and Baker and Lennon (1973) for measurements of tidal tilt and limits the usefulness of tidal strain and tilt amplitudes in the investigation of Earth's elastic properties. These effects are strongest at free surfaces of the chambers (cavities) in which instruments are in-

stalled and near the free surface of the Earth, which can have a significant topography. The free-surface condition lets components of the stress tensor vanish and this enforces specific linear combinations for the components of the deformation tensor through the stress-strain relation. Harrison (1976) investigated this by finite-element modeling.

All strain measurements are affected by such strain-strain coupling. This applies to DAS recordings as well as to conventional strainmeters. In a more general sense the coupling issues between rock and fiber could also be summarized under these effects of local heterogeneity. Likewise particle motion is affected by free-surface conditions (Kennett, 1991). When comparing DAS recorded strain with signals from reference instruments, these effects generally could limit the usefulness of the observations, but are commonly ignored in the respective studies (except for cable coupling). The problem is even more critical, when comparing DAS recorded strain with particle motion recorded by seismometers, because the effect of the free surface on both is different and most likely the plane wave assumption (see section S4 'Plane wave strain from seismometer recordings') is violated in this way. If DAS recorded strain is compared to recordings of a strainmeter, as is done in the current study, a problem may arise from spatially varying strain-strain coupling, if instruments are installed at a distance from each other.

The 10 m long Invar-wire strainmeters show little cavity effects due to their installation in the center and along the symmetry axes of 60 m long tunnels. For the DAS cables the cavity effects in a more general sense are addressed as coupling issues controlled by installation and cable type.

Topography at BFO, however, alters the strain field as demonstrated by Emter and Zürn (1985) with finite element simulations. In particular the strainmeter in azimuth N60°E experiences significant strain-strain coupling through the local topography. Zürn et al. (2015, their table S2 in the supporting material) list the strain-strain coupling coefficients derived from tidal analysis. Their analysis of the radial mode ${}_0S_0$ (Zürn et al., 2015, their table 2) suggests that not the same coupling might be at work for this type of straining. The factor 0.58 (for N60°E) given by Zürn et al. (2015, their table S2 in the supporting material) for tidal analysis is consistent with the factor of 0.67 derived in a 2D finite element analysis by Emter and Zürn (1985, their figure 5). For strain in the azimuth N90°E of the 'Vorstollen' we presumably observe part of this topography effect. The seismometer data systematically over-estimates the strain amplitude in this azimuth, as discussed in section S4.2 'Regression with respect to seismometer data'.

In the current experiment we use the Invar-wire strainmeter in a comparison with DAS data recorded at

a distance of about 350 m. If the strain-strain coupling would vary along this distance, it would contribute to the amplitude difference seen between DAS recordings and strainmeter recordings. The difference shown by Emter and Zürn (1985, their Fig. 5), with strain amplitude increasing towards the tunnel entrance near the free surface, however, is opposite to the observed difference. Because the section of the ‘Vorstollen’, which is used in the current analysis, is at distance of about 200 m to

the entrance the expected strain-strain coupling would be almost the same as for the strainmeters, according to Emter and Zürn (1985, their Fig. 5).

For strain recordings with cemented fibers in the ‘Vorstollen’ Forbriger et al. (2024) recently found a STR of about 1 with respect to the strainmeters for four different IUs, independently. We take this as a confirmation that the DAS cable and the strainmeters experience the same topography-effect, indeed.

Table S2: Events used in the analysis. Source parameters are taken from the GEOFON catalog. backazimuth (BAZ) and epicentral distance (Δ) are given with respect to BFO (48.33°N, 8.33°E). Maximum amplitude A_{\max} is the largest amplitude in the surface wave train and is from visual inspection of the strainmeter signals.

ID	Mw	origin time	region	latitude	longitude	depth / km	BAZ	Δ	A_{\max} / nstrain
gfz2023dsww	6.79	2023-02-23 00:37:39.01	Tajikistan-Xinjiang Border Region	38.06°N	73.29°E	10.0	N77.24°E	47.06°	20.0
gfz2023doky	6.34	2023-02-20 17:04:30.09	Turkey	36.11°N	35.93°E	10.0	N110.83°E	23.63°	8.0
gfz2023coos	7.59	2023-02-06 10:24:49.96	Turkey	38.11°N	37.22°E	10.0	N105.26°E	23.24°	130.0
gfz2023cnwr	7.69	2023-02-06 01:17:34.97	Turkey	37.23°N	37.05°E	10.0	N107.24°E	23.64°	250.0
gfz2023apzg	7.58	2023-01-09 17:47:35.03	Banda Sea	-7.11°N	129.98°E	108.1	N69.87°E	115.92°	1.5
gfz2022wxsg	6.06	2022-11-23 01:08:16.89	Turkey	40.97°N	31.05°E	10.0	N106.06°E	17.69°	3.0
gfz2022wvvo	7.01	2022-11-22 02:03:07.65	Solomon Islands	-9.78°N	159.57°E	9.7	N41.48°E	134.41°	2.5
gfz2022wcnj	6.83	2022-11-18 13:37:09.2	Southwest of Sumatra, Indonesia	-4.77°N	100.90°E	10.0	N91.10°E	95.16°	2.0
gfz2022wcnj	7.28	2022-11-11 10:48:48.57	Tonga Islands Region	-19.27°N	-172.38°E	44.5	N1.38°E	150.73°	3.0
gfz2022vpri	6.08	2022-11-04 10:02:51.02	Gulf of California	28.13°N	-112.15°E	10.0	N275.73°E	84.68°	1.5
gfz2022uoko	6.78	2022-10-20 11:57:11.66	South of Panama	7.66°N	-82.32°E	10.0	N297.89°E	89.69°	5.0
gfz2022sovf	6.79	2022-09-22 06:16:08.89	Michoacan, Mexico	18.33°N	-102.94°E	15.0	N298.02°E	89.65°	19.0
gfz2022shod	6.92	2022-09-18 06:44:16.55	Taiwan	23.20°N	121.35°E	10.0	N57.83°E	86.89°	10.0
gfz2022sgyk	6.46	2022-09-17 13:41:20.35	Taiwan	23.11°N	121.29°E	10.0	N57.93°E	86.92°	2.0
gfz2022rufw	7.51	2022-09-10 23:46:59.95	Papua New Guinea Region	-6.25°N	146.48°E	100.0	N53.88°E	124.91°	2.5
gfz2022rjqx	6.60	2022-09-05 04:52:19.87	Sichuan, China	29.64°N	102.16°E	10.0	N66.71°E	70.75°	2.0
gfz2022riez	6.88	2022-09-04 09:42:20.22	Central Mid-Atlantic Ridge	-0.85°N	-21.76°E	10.0	N217.51°E	55.46°	2.5
gfz2022oogo	6.99	2022-07-27 00:43:25.36	Luzon, Philippines	17.50°N	120.82°E	21.0	N61.70°E	91.06°	2.5

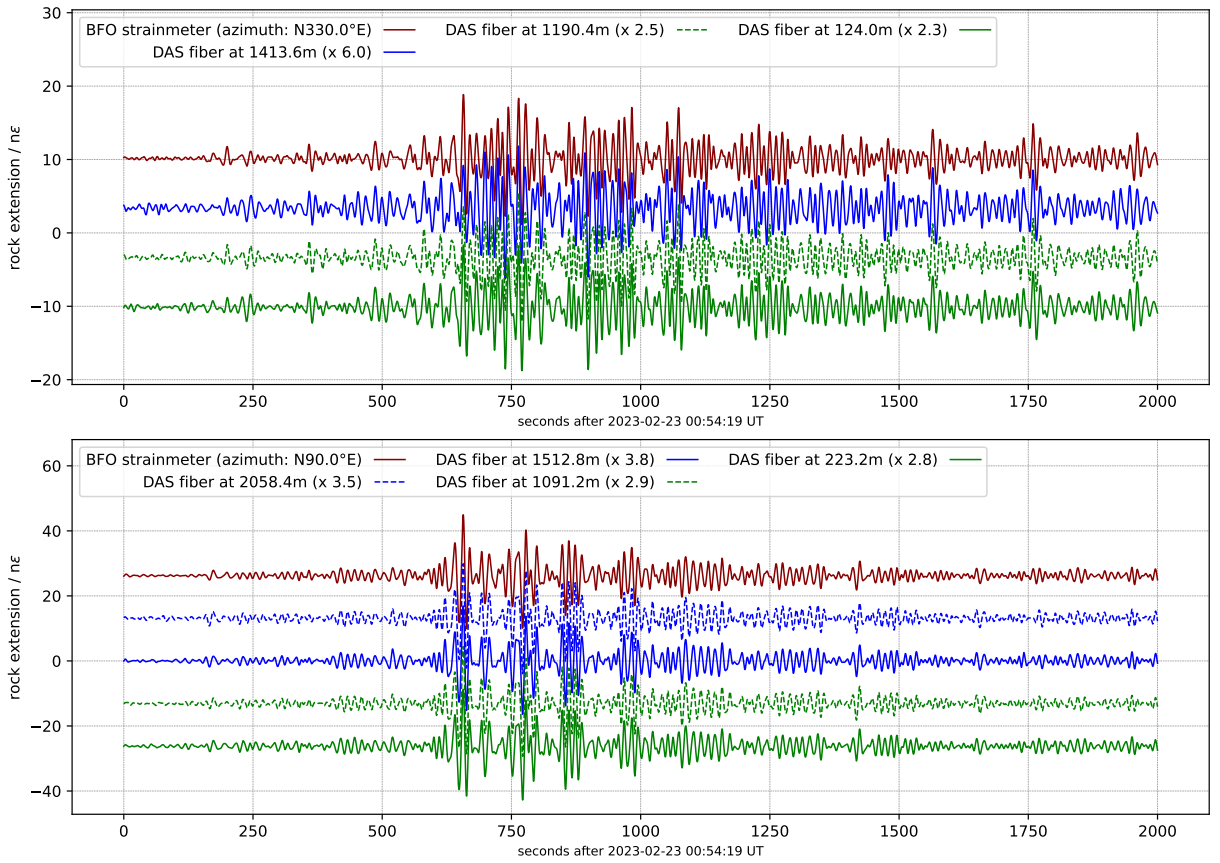


Figure S3: Surface wave data in the frequency band 0.05 Hz to 0.1 Hz for Mw 6.79 Tajikistan-Xinjiang Border Region 2023-02-23 00:37:39.01 UTC 38.06°N 73.29°E 10.0 km (BAZ=N77.24°E, Δ =47.06°). Top: ‘Anton Gang’ (N330°E), bottom: ‘Vorstollen’ (N90°E). DAS data are scaled (factors are given in the legend) to minimize the rms misfit with respect to the strainmeter waveform.

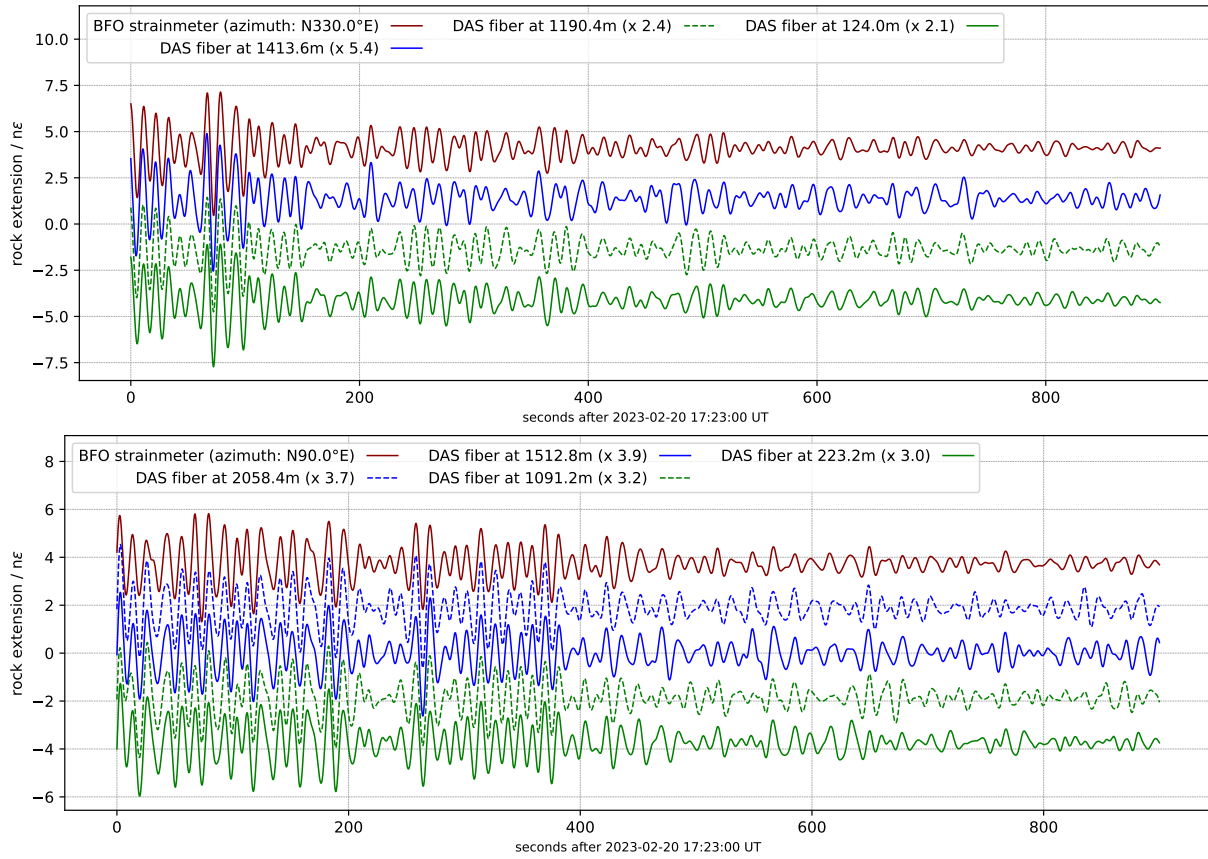


Figure S4: Surface wave data in the frequency band 0.05 Hz to 0.1 Hz for Mw 6.34 Turkey 2023-02-20 17:04:30.09 UTC 36.11°N 35.93°E 10.0 km (BAZ=N110.83°E, $\Delta=23.63^\circ$). Top: ‘Anton Gang’ (N330°E), bottom: ‘Vorstollen’ (N90°E). DAS data are scaled (factors are given in the legend) to minimize the rms misfit with respect to the strainmeter waveform.

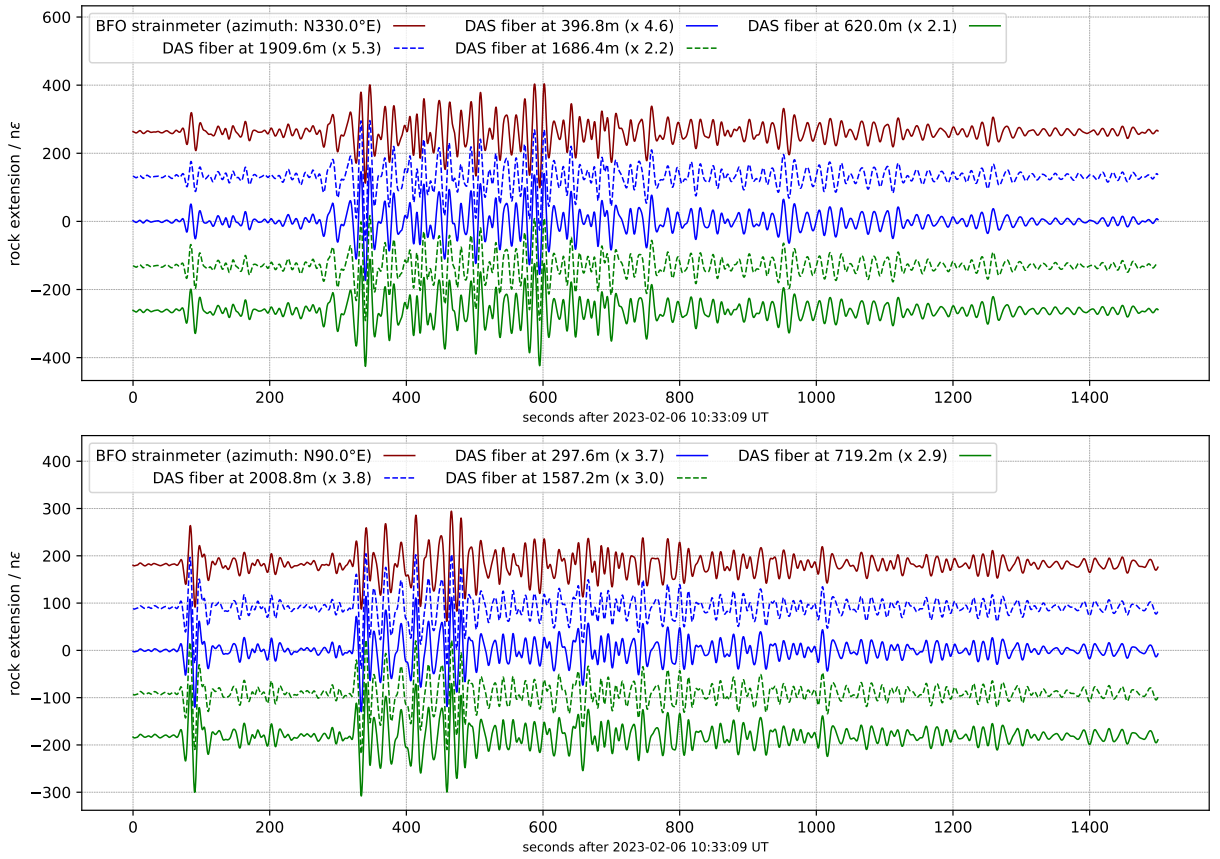


Figure S5: Surface wave data in the frequency band 0.05 Hz to 0.1 Hz for Mw 7.59 Turkey 2023-02-06 10:24:49.96 UTC 38.11°N 37.22°E 10.0 km (BAZ=N105.26°E, Δ =23.24°). Top: ‘Anton Gang’ (N330°E), bottom: ‘Vorstollen’ (N90°E). DAS data are scaled (factors are given in the legend) to minimize the rms misfit with respect to the strainmeter waveform.

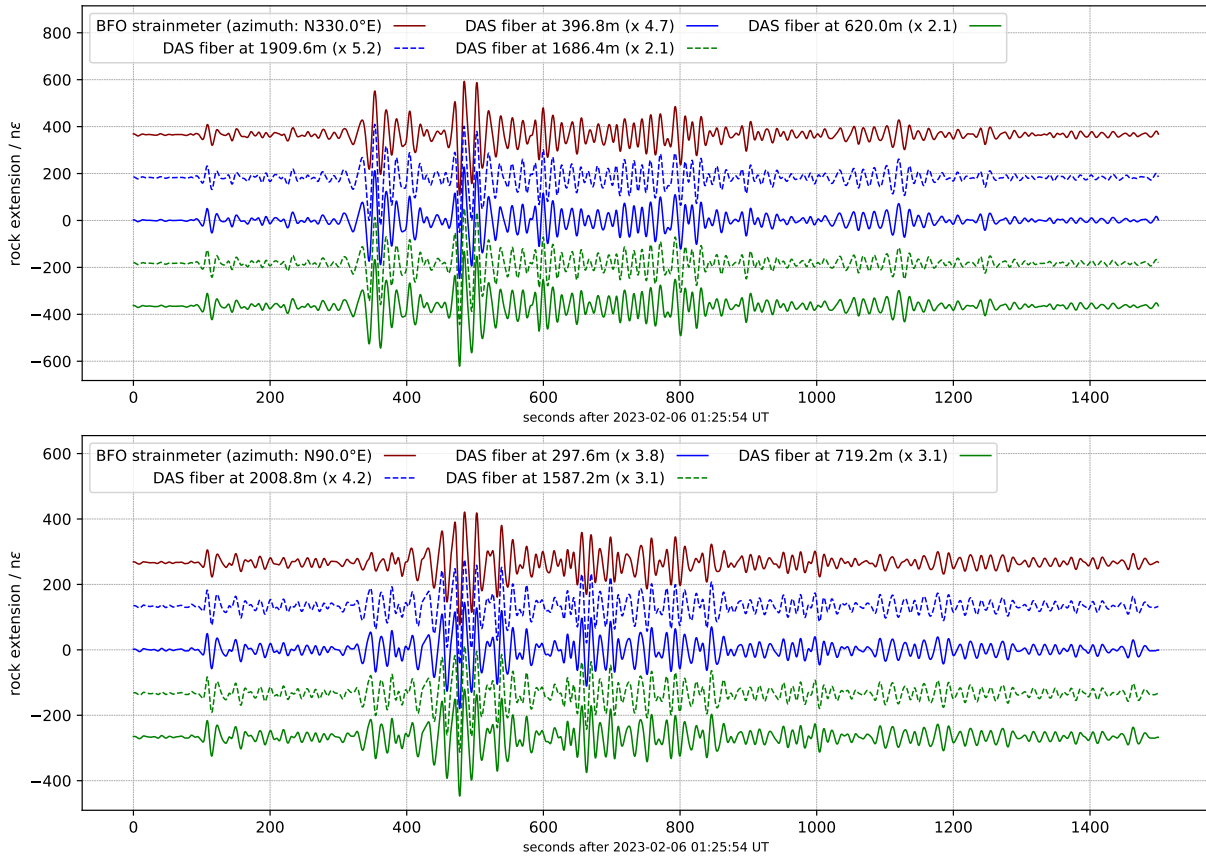


Figure S6: Surface wave data in the frequency band 0.05 Hz to 0.1 Hz for Mw 7.69 Turkey 2023-02-06 01:17:34.97 UTC 37.23°N 37.05°E 10.0 km (BAZ=N107.24°E, $\Delta=23.64^\circ$). Top: ‘Anton Gang’ (N330°E), bottom: ‘Vorstollen’ (N90°E). DAS data are scaled (factors are given in the legend) to minimize the rms misfit with respect to the strainmeter waveform.

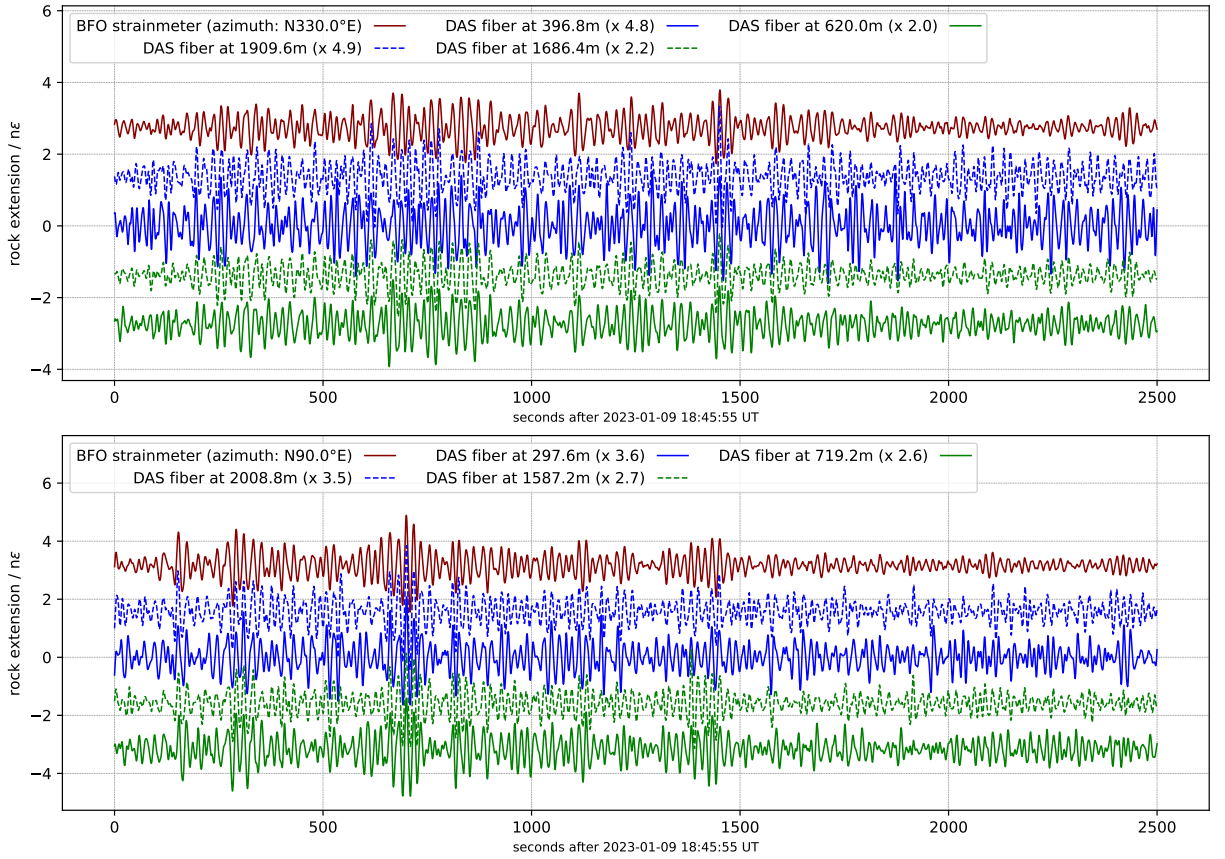


Figure S7: Surface wave data in the frequency band 0.05 Hz to 0.1 Hz for Mw 7.58 Banda Sea 2023-01-09 17:47:35.03 UTC -7.11°N 129.98°E km km (BAZ= $N69.87^{\circ}\text{E}$, $\Delta=115.92^{\circ}$). Top: ‘Anton Gang’ ($N330^{\circ}\text{E}$), bottom: ‘Vorstollen’ ($N90^{\circ}\text{E}$). DAS data are scaled (factors are given in the legend) to minimize the rms misfit with respect to the strainmeter waveform.

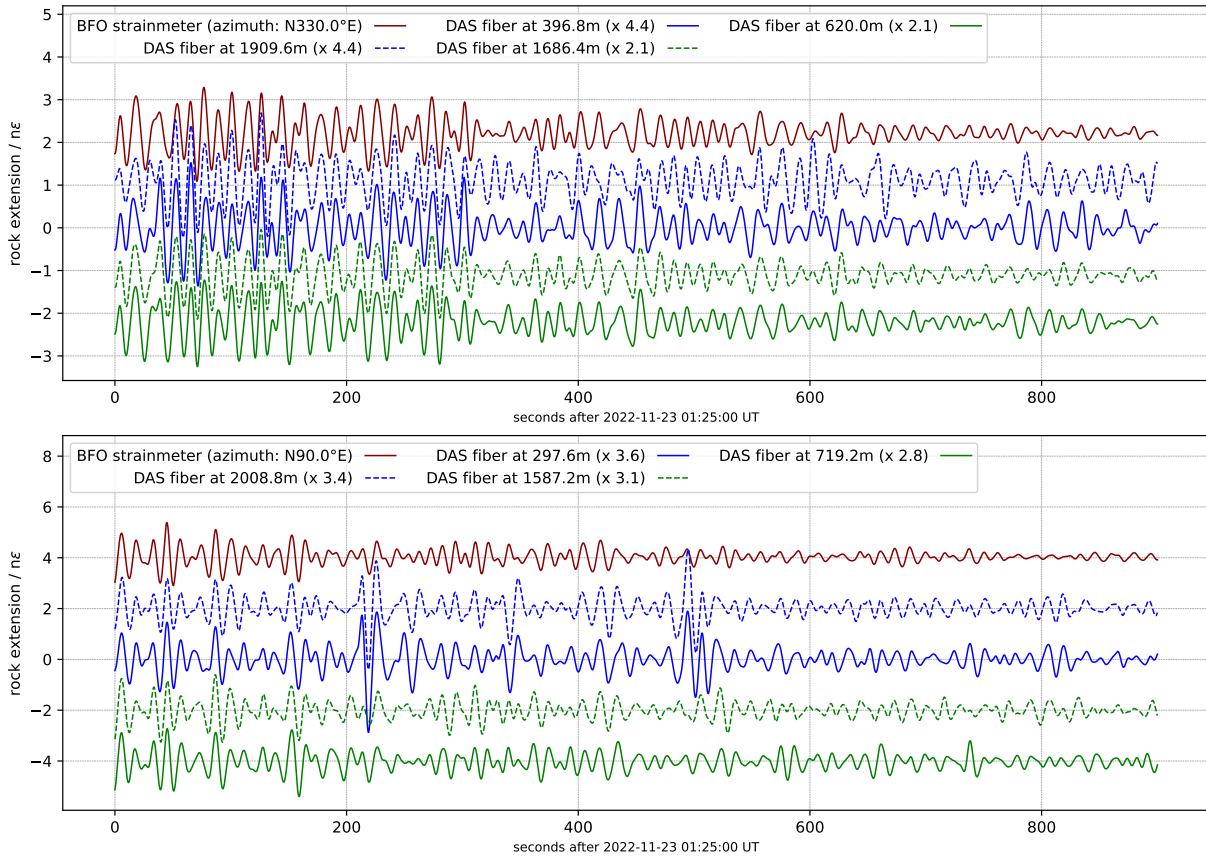


Figure S8: Surface wave data in the frequency band 0.05 Hz to 0.1 Hz for Mw 6.06 Turkey 2022-11-23 01:08:16.89 UTC 40.97°N 31.05°E 10.0 km (BAZ=N106.06°E, $\Delta=17.69^\circ$). Top: ‘Anton Gang’ (N330°E), bottom: ‘Vorstollen’ (N90°E). DAS data are scaled (factors are given in the legend) to minimize the rms misfit with respect to the strainmeter waveform.

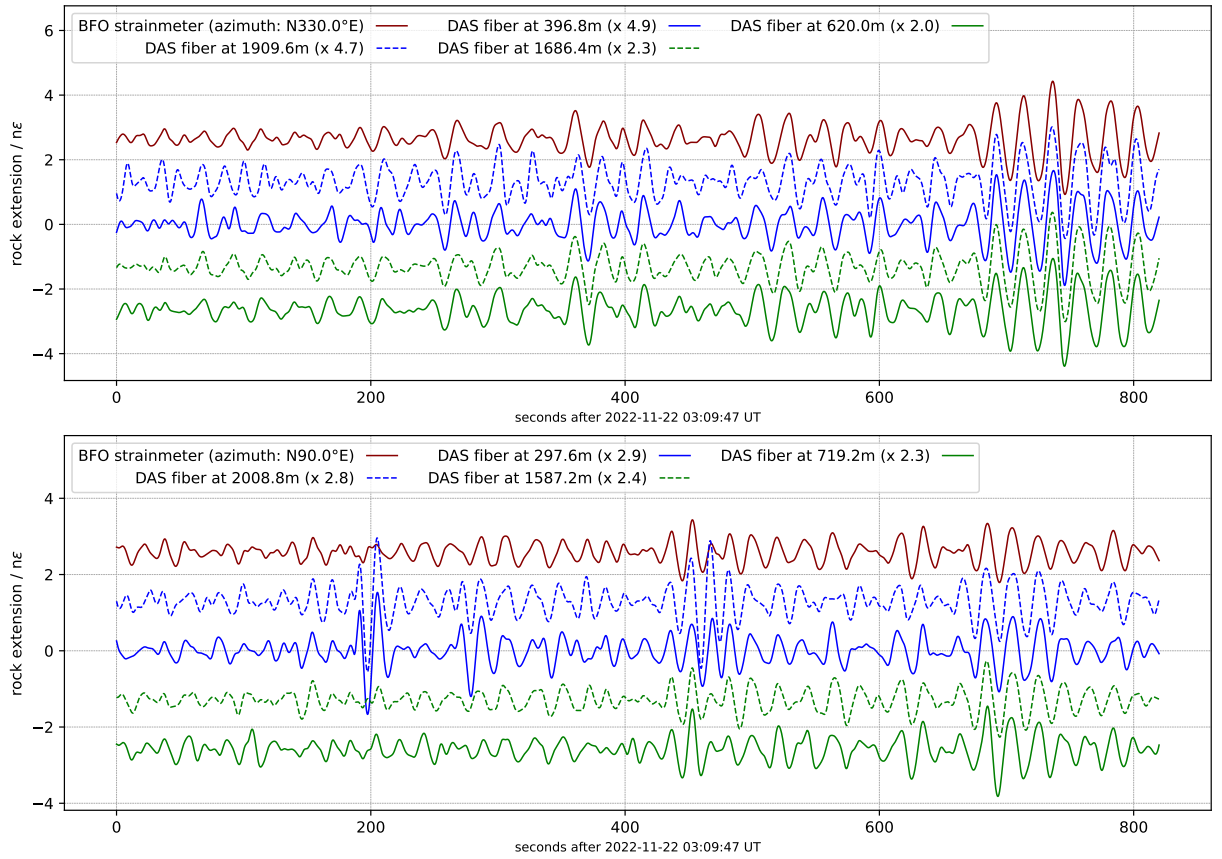


Figure S9: Surface wave data in the frequency band 0.05 Hz to 0.1 Hz for Mw 7.01 Solomon Islands 2022-11-22 02:03:07.65 UTC -9.78°N 159.57°E 9.7 km (BAZ= $N41.48^{\circ}\text{E}$, $\Delta=134.41^{\circ}$). Top: ‘Anton Gang’ ($N330^{\circ}\text{E}$), bottom: ‘Vorstollen’ ($N90^{\circ}\text{E}$). DAS data are scaled (factors are given in the legend) to minimize the rms misfit with respect to the strainmeter waveform.

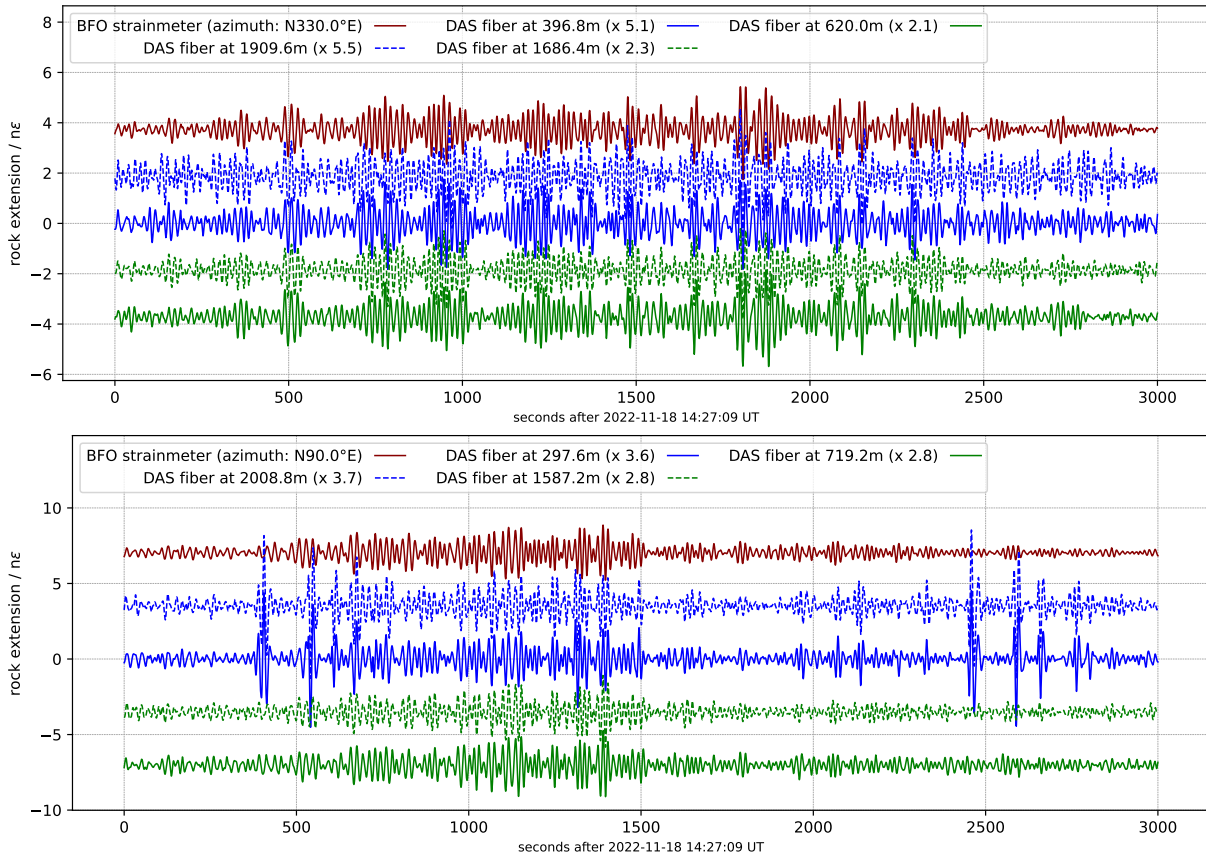


Figure S10: Surface wave data in the frequency band 0.05 Hz to 0.1 Hz for Mw 6.83 Southwest of Sumatra, Indonesia 2022-11-18 13:37:09.2 UTC -4.77°N 100.90°E 10.0 km (BAZ= $\text{N}91.10^{\circ}\text{E}$, $\Delta=95.16^{\circ}$). Top: ‘Anton Gang’ ($\text{N}330^{\circ}\text{E}$), bottom: ‘Vorstollen’ ($\text{N}90^{\circ}\text{E}$). DAS data are scaled (factors are given in the legend) to minimize the rms misfit with respect to the strainmeter waveform.

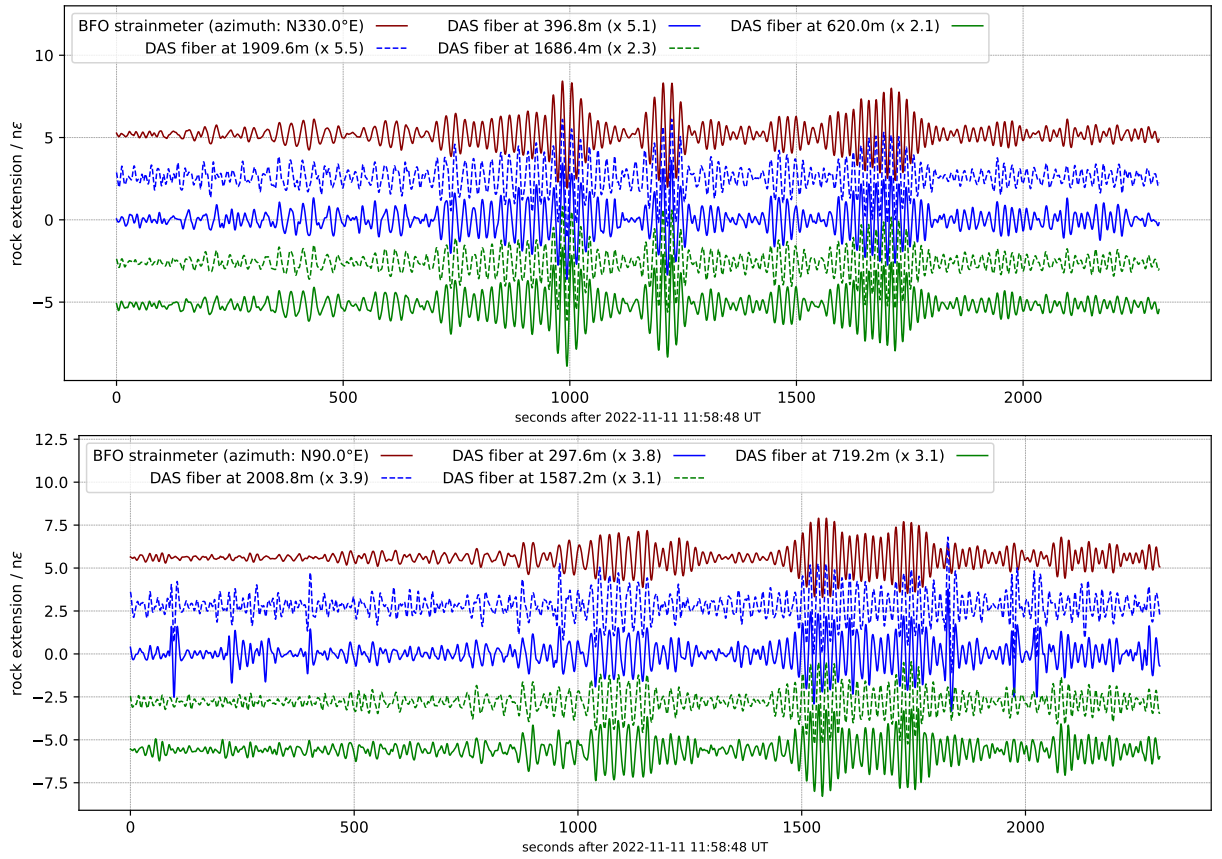


Figure S11: Surface wave data in the frequency band 0.05 Hz to 0.1 Hz for Mw 7.28 Tonga Islands Region 2022-11-11 10:48:48.57 UTC -19.27°N -172.38°E 44.5 km (BAZ= $\text{N}1.38^{\circ}\text{E}$, $\Delta=150.73^{\circ}$). Top: ‘Anton Gang’ ($\text{N}330^{\circ}\text{E}$), bottom: ‘Vorstollen’ ($\text{N}90^{\circ}\text{E}$). DAS data are scaled (factors are given in the legend) to minimize the rms misfit with respect to the strainmeter waveform.

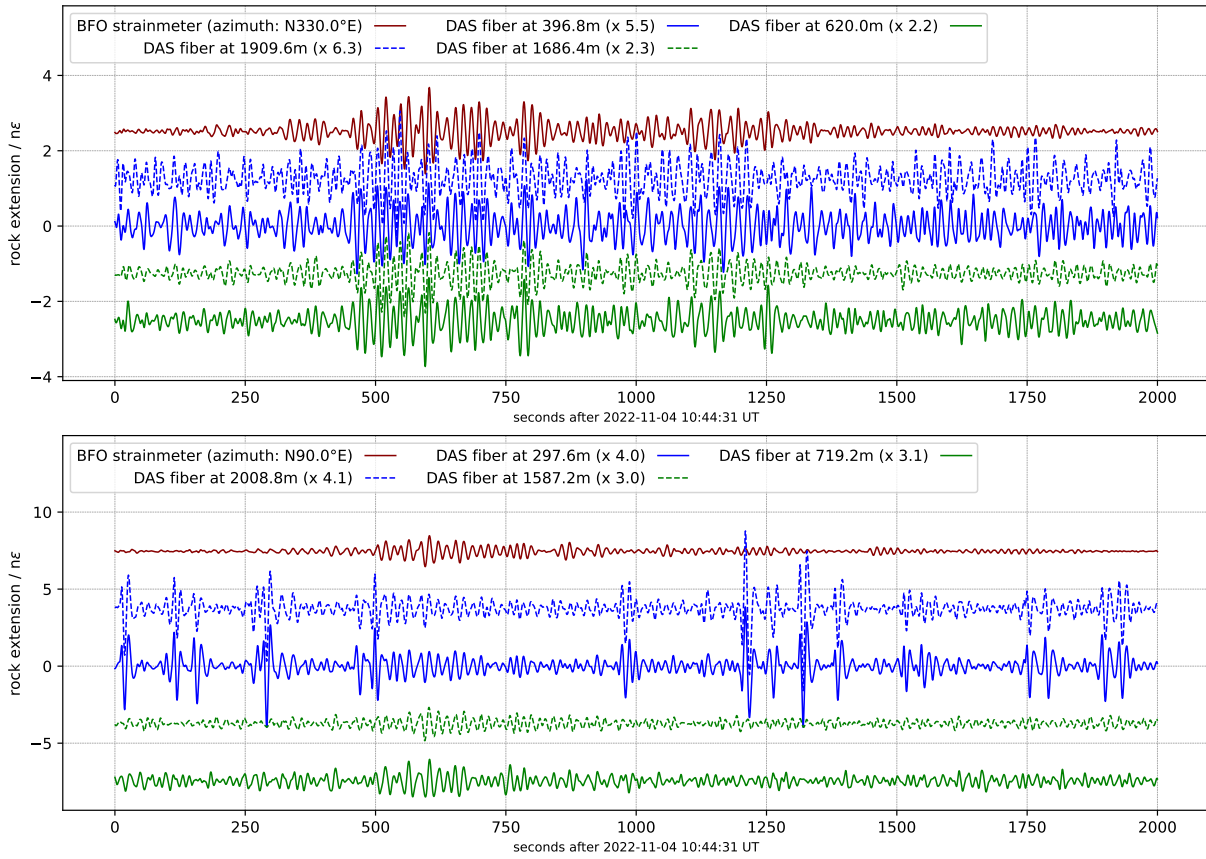


Figure S12: Surface wave data in the frequency band 0.05 Hz to 0.1 Hz for Mw 6.08 Gulf of California 2022-11-04 10:02:51.02 UTC 28.13°N –112.15°E 10.0 km (BAZ=N310.50°E, $\Delta=86.94^\circ$). Top: ‘Anton Gang’ (N330°E), bottom: ‘Vorstollen’ (N90°E). DAS data are scaled (factors are given in the legend) to minimize the rms misfit with respect to the strainmeter waveform.

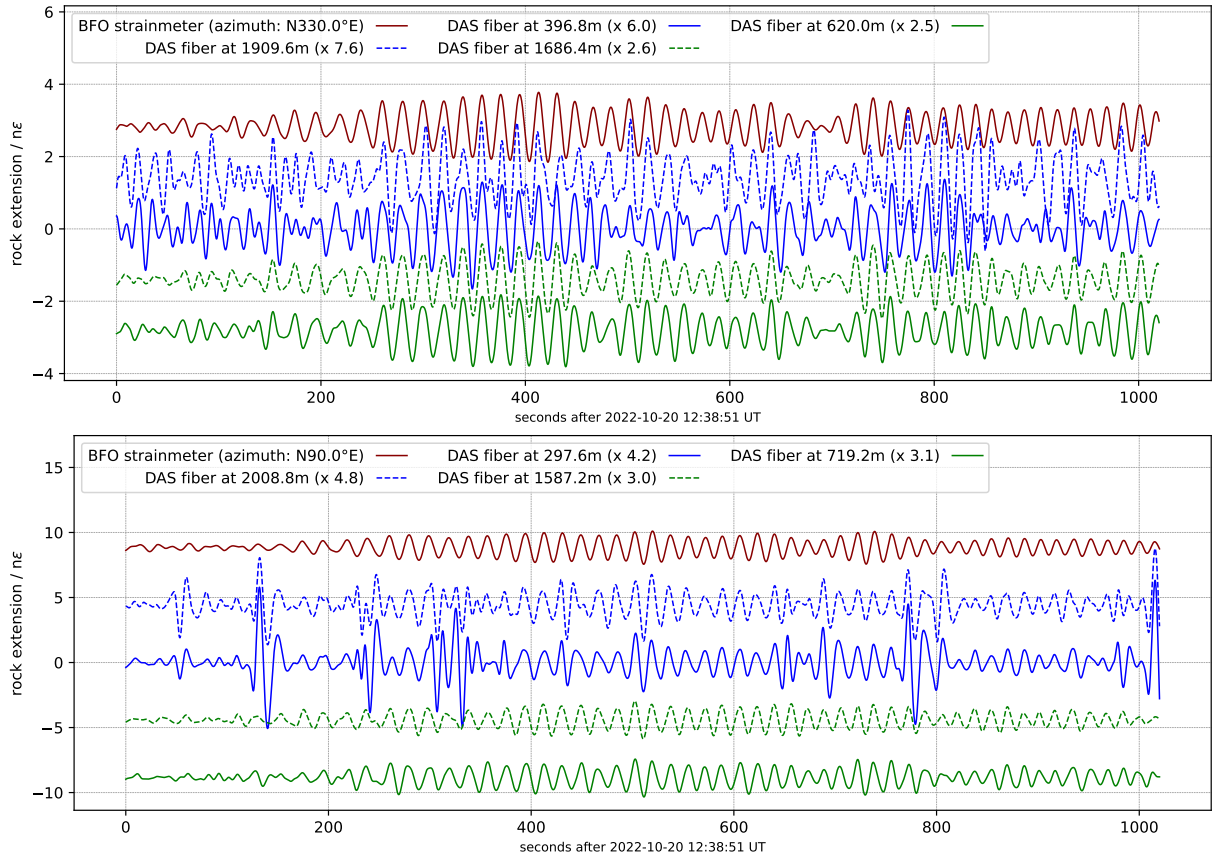


Figure S13: Surface wave data in the frequency band 0.05 Hz to 0.1 Hz for Mw 6.78 South of Panama 2022-10-20 11:57:11.66 UTC 7.66°N –82.32°E 10.0 km (BAZ=N275.73°E, Δ =84.68°). Top: ‘Anton Gang’ (N330°E), bottom: ‘Vorstollen’ (N90°E). DAS data are scaled (factors are given in the legend) to minimize the rms misfit with respect to the strainmeter waveform.

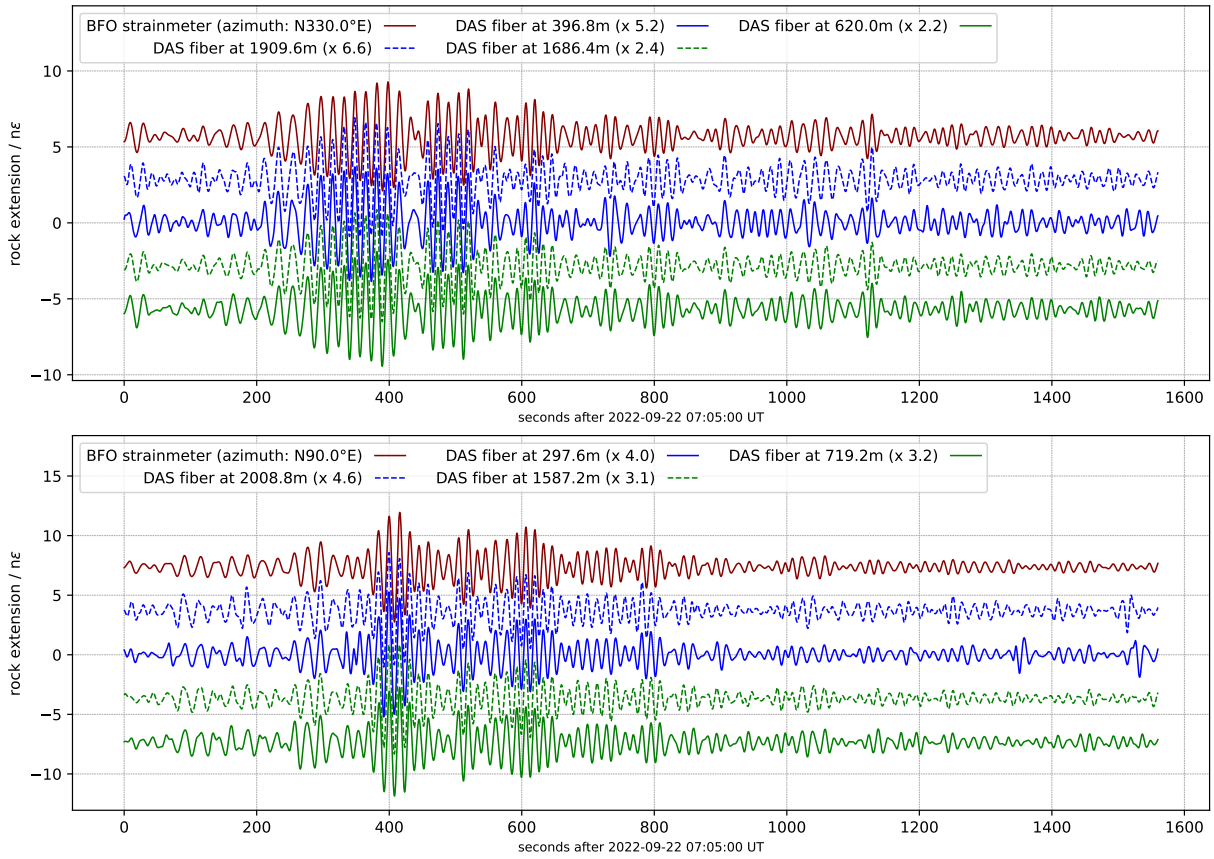


Figure S14: Surface wave data in the frequency band 0.05 Hz to 0.1 Hz for Mw 6.79 Michoacan, Mexico 2022-09-22 06:16:08.89 UTC 18.33°N –102.94°E 15.0 km (BAZ=N297.89°E, Δ =89.69°). Top: ‘Anton Gang’ (N330°E), bottom: ‘Vorstollen’ (N90°E). DAS data are scaled (factors are given in the legend) to minimize the rms misfit with respect to the strainmeter waveform.

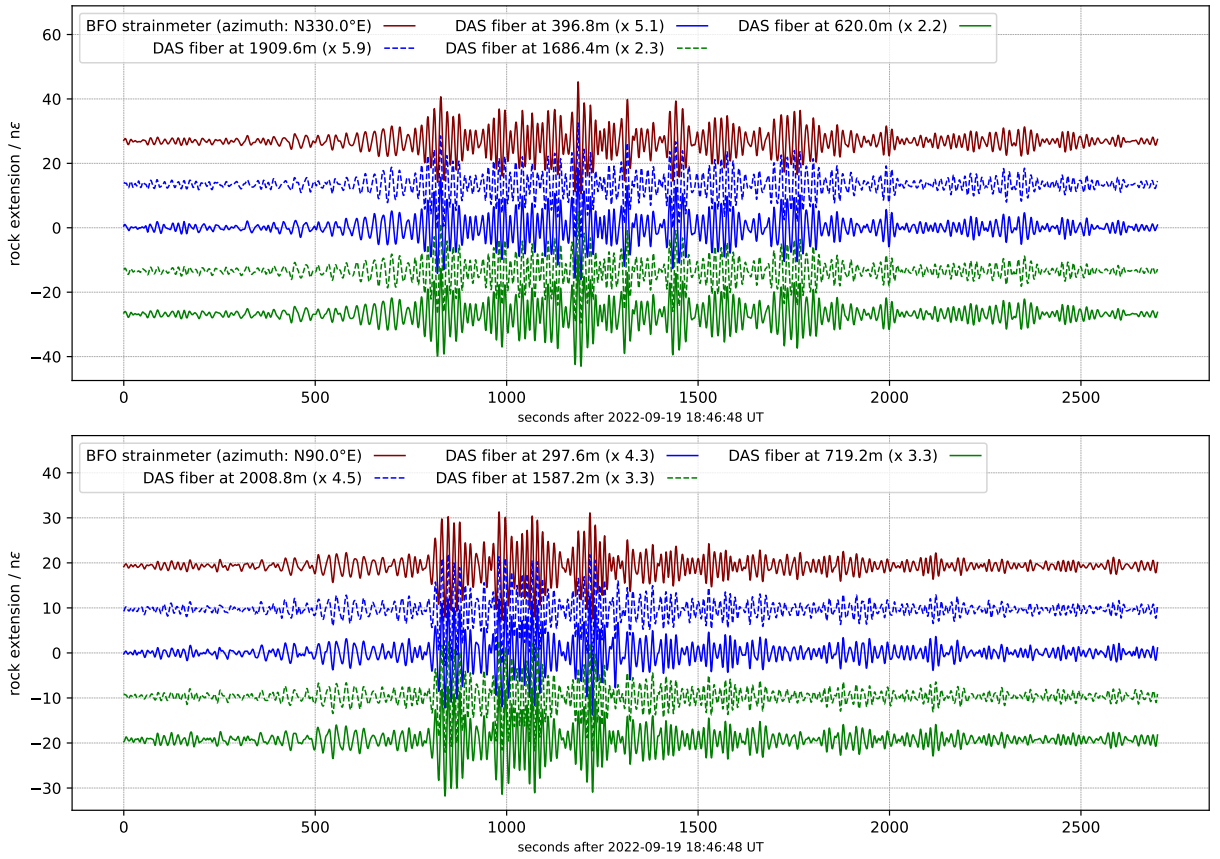


Figure S15: Surface wave data in the frequency band 0.05 Hz to 0.1 Hz for Mw 7.59 Near Coast of Michoacan, Mexico 2022-09-19 18:05:08.76 UTC 18.44°N – 103.01°E 20.0 km (BAZ=N298.02°E, Δ =89.65°). Top: ‘Anton Gang’ (N330°E), bottom: ‘Vorstollen’ (N90°E). DAS data are scaled (factors are given in the legend) to minimize the rms misfit with respect to the strainmeter waveform.

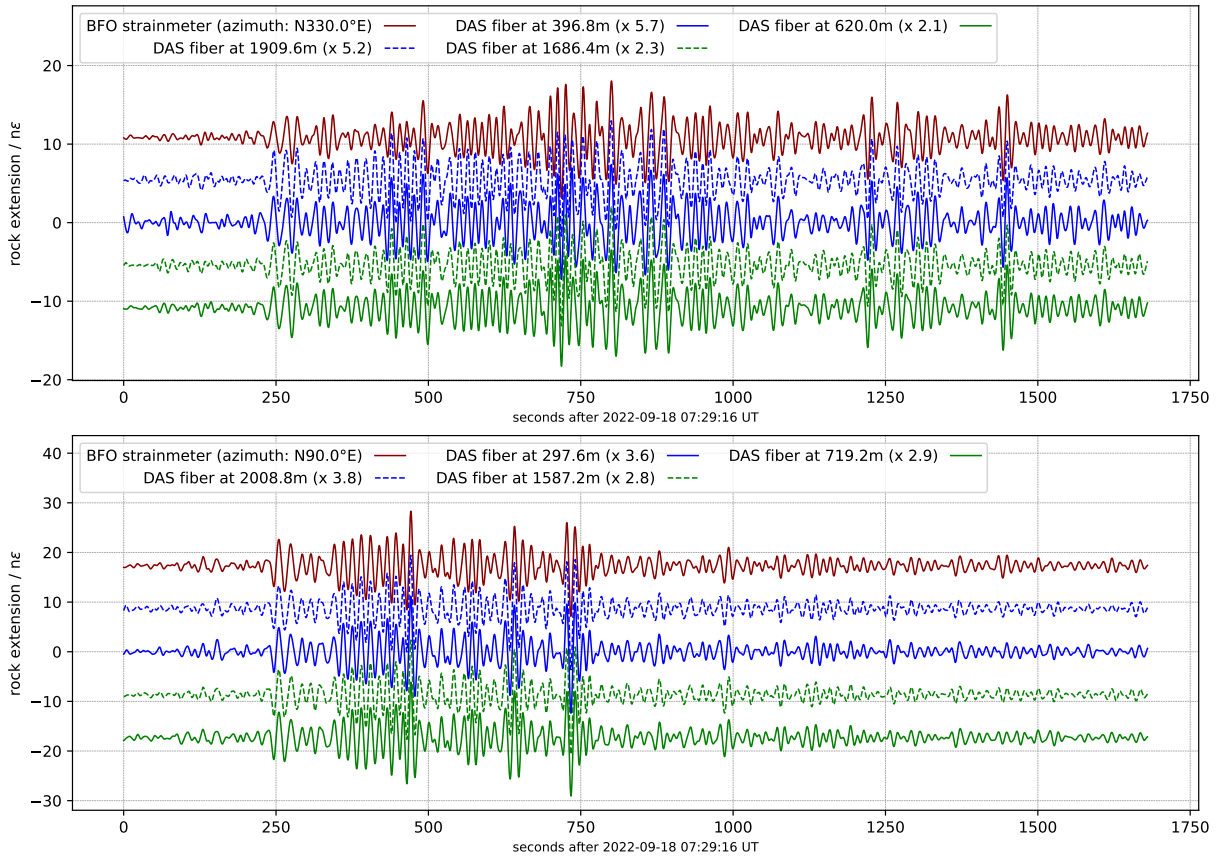


Figure S16: Surface wave data in the frequency band 0.05 Hz to 0.1 Hz for Mw 6.92 Taiwan 2022-09-18 06:44:16.55 UTC 23.20°N 121.35°E 10.0 km (BAZ=N57.83°E, Δ =86.89°). Top: 'Anton Gang' (N330°E), bottom: 'Vorstollen' (N90°E). DAS data are scaled (factors are given in the legend) to minimize the rms misfit with respect to the strainmeter waveform.

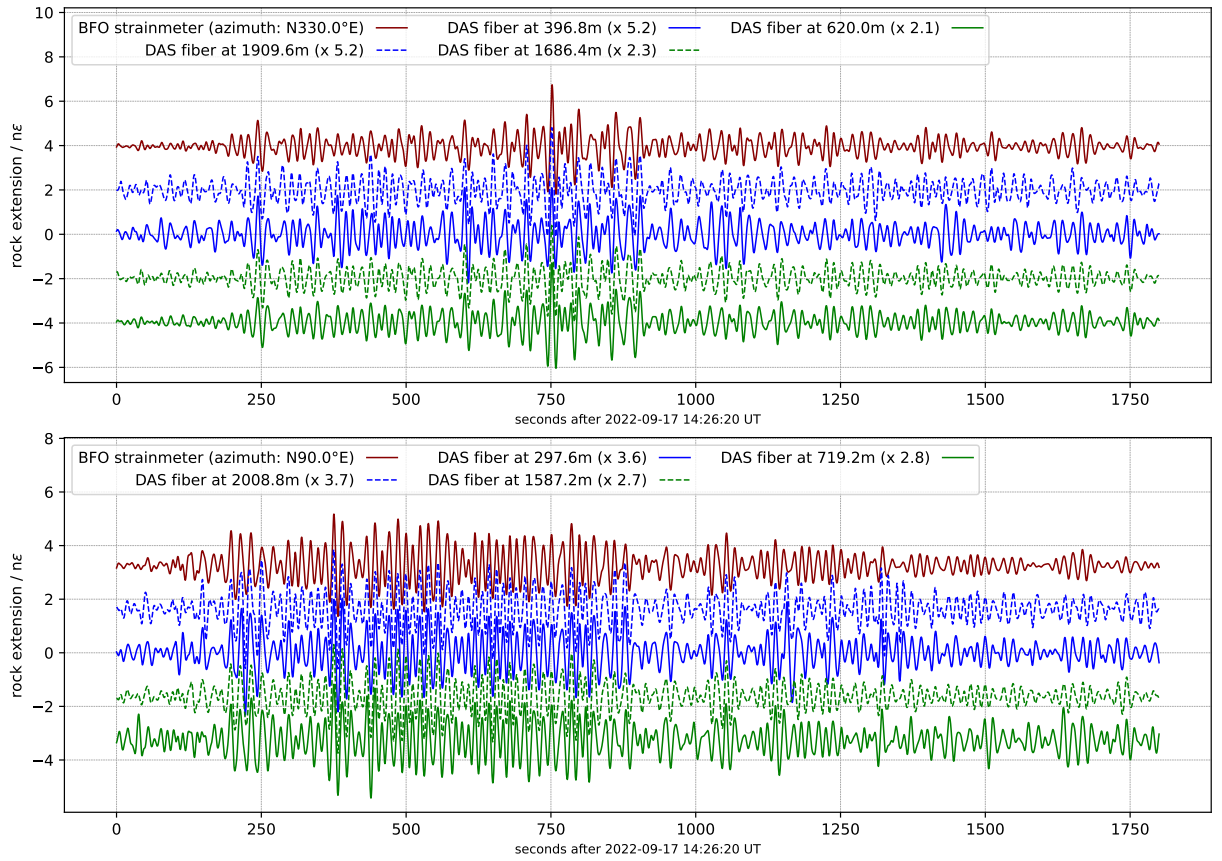


Figure S17: Surface wave data in the frequency band 0.05 Hz to 0.1 Hz for Mw 6.46 Taiwan 2022-09-17 13:41:20.35 UTC 23.11°N 121.29°E 10.0 km (BAZ=N57.93°E, Δ =86.92°). Top: 'Anton Gang' (N330°E), bottom: 'Vorstollen' (N90°E). DAS data are scaled (factors are given in the legend) to minimize the rms misfit with respect to the strainmeter waveform.

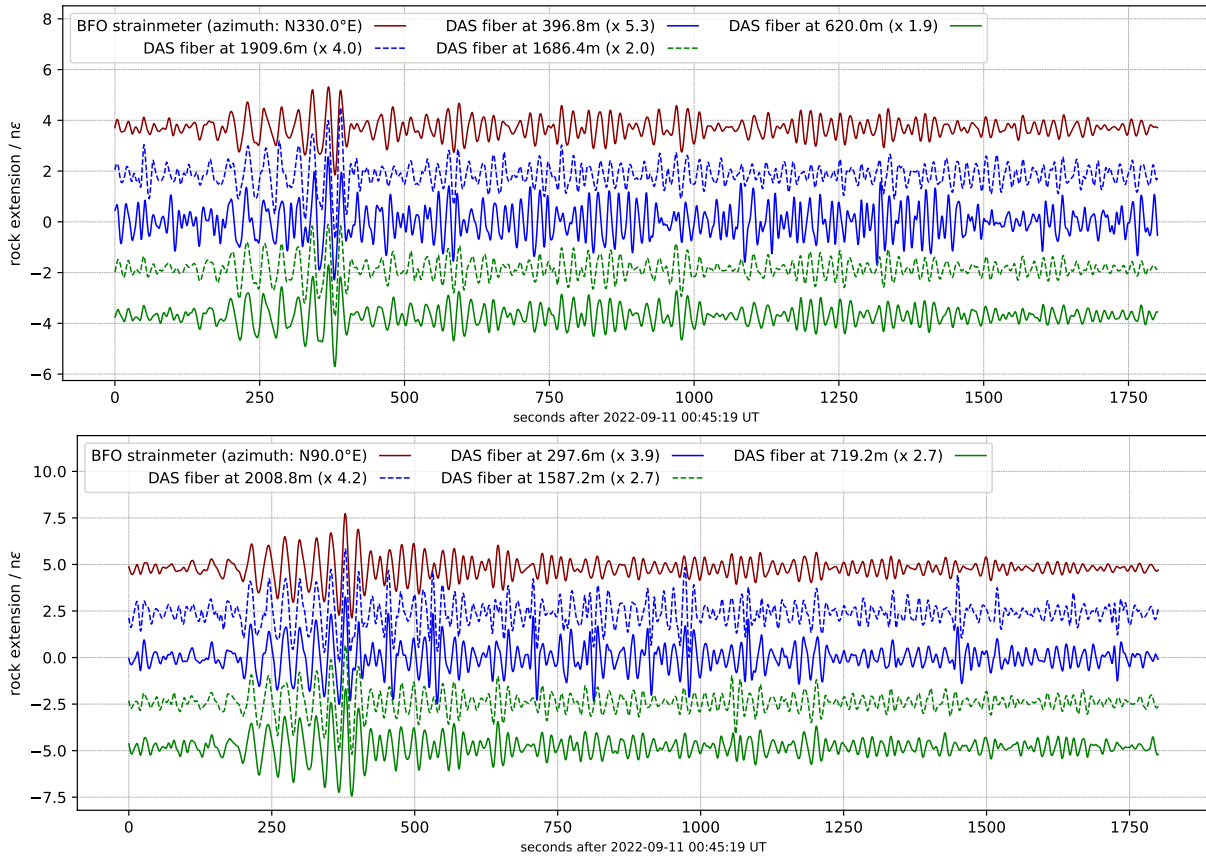


Figure S18: Surface wave data in the frequency band 0.05 Hz to 0.1 Hz for Mw 7.51 Papua New Guinea Region 2022-09-10 23:46:59.95 UTC -6.25°N 146.48°E km km (BAZ= $\text{N}53.88^{\circ}\text{E}$, $\Delta=124.91^{\circ}$). Top: ‘Anton Gang’ ($\text{N}330^{\circ}\text{E}$), bottom: ‘Vorstollen’ ($\text{N}90^{\circ}\text{E}$). DAS data are scaled (factors are given in the legend) to minimize the rms misfit with respect to the strainmeter waveform.

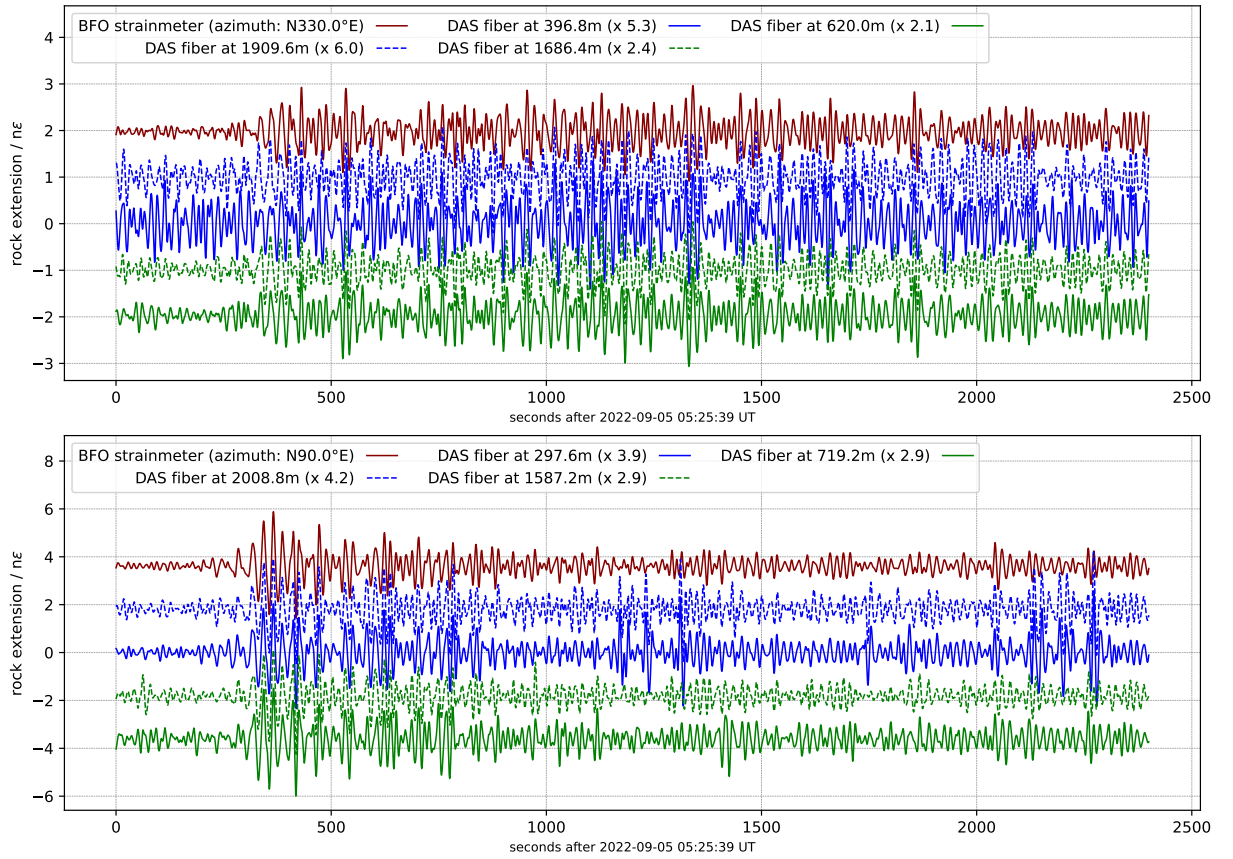


Figure S19: Surface wave data in the frequency band 0.05 Hz to 0.1 Hz for Mw 6.60 Sichuan, China 2022-09-05 04:52:19.87 UTC 29.64°N 102.16°E 10.0 km (BAZ=N66.71°E, $\Delta=70.75^\circ$). Top: 'Anton Gang' (N330°E), bottom: 'Vorstollen' (N90°E). DAS data are scaled (factors are given in the legend) to minimize the rms misfit with respect to the strainmeter waveform.

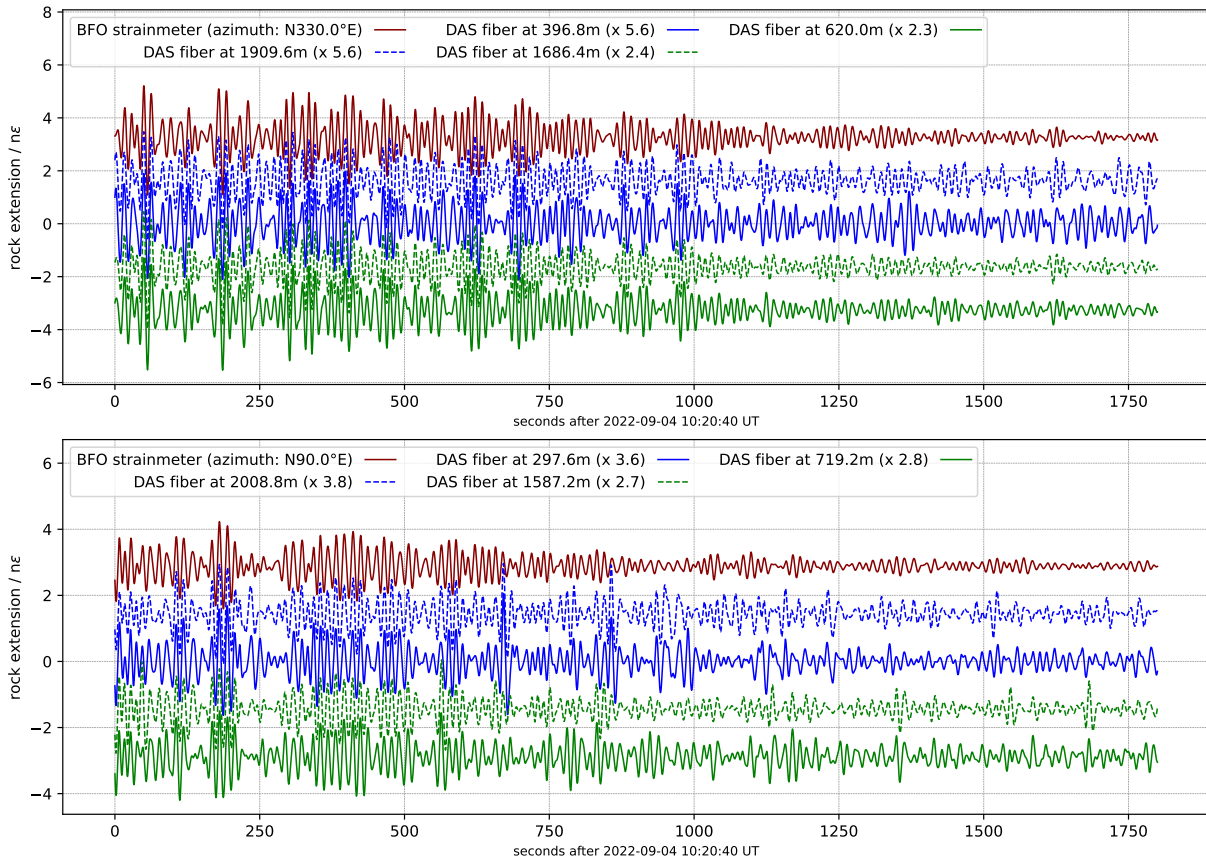


Figure S20: Surface wave data in the frequency band 0.05 Hz to 0.1 Hz for Mw 6.88 Central Mid-Atlantic Ridge 2022-09-04 09:42:20.22 UTC -0.85°N -21.76°E 10.0 km (BAZ= $\text{N}217.51^{\circ}\text{E}$, $\Delta=55.46^{\circ}$). Top: ‘Anton Gang’ ($\text{N}330^{\circ}\text{E}$), bottom: ‘Vorstollen’ ($\text{N}90^{\circ}\text{E}$). DAS data are scaled (factors are given in the legend) to minimize the rms misfit with respect to the strainmeter waveform.

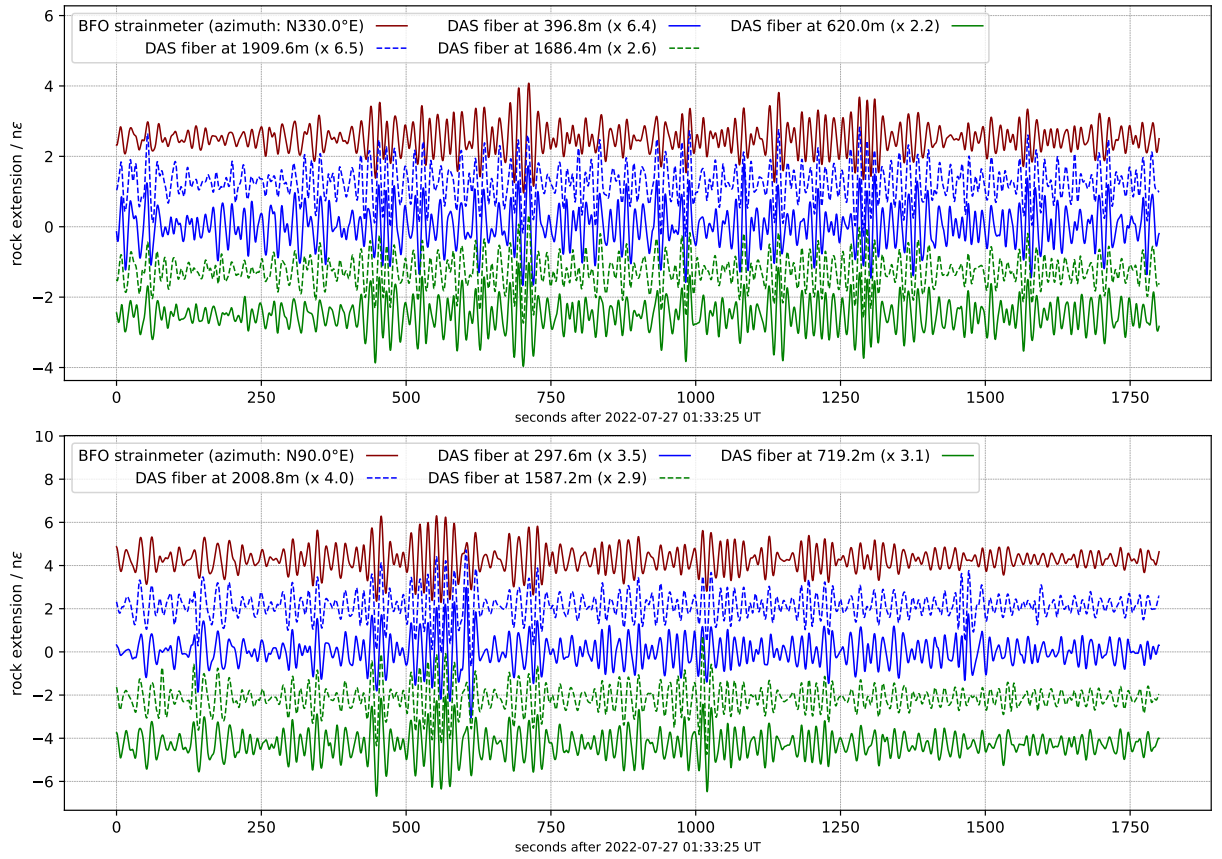


Figure S21: Surface wave data in the frequency band 0.05 Hz to 0.1 Hz for Mw 6.99 Luzon, Philippines 2022-07-27 00:43:25.36 UTC 17.50°N 120.82°E 21.0 km (BAZ=N61.70°E, Δ =91.06°). Top: 'Anton Gang' (N330°E), bottom: 'Vorstollen' (N90°E). DAS data are scaled (factors are given in the legend) to minimize the rms misfit with respect to the strainmeter waveform.

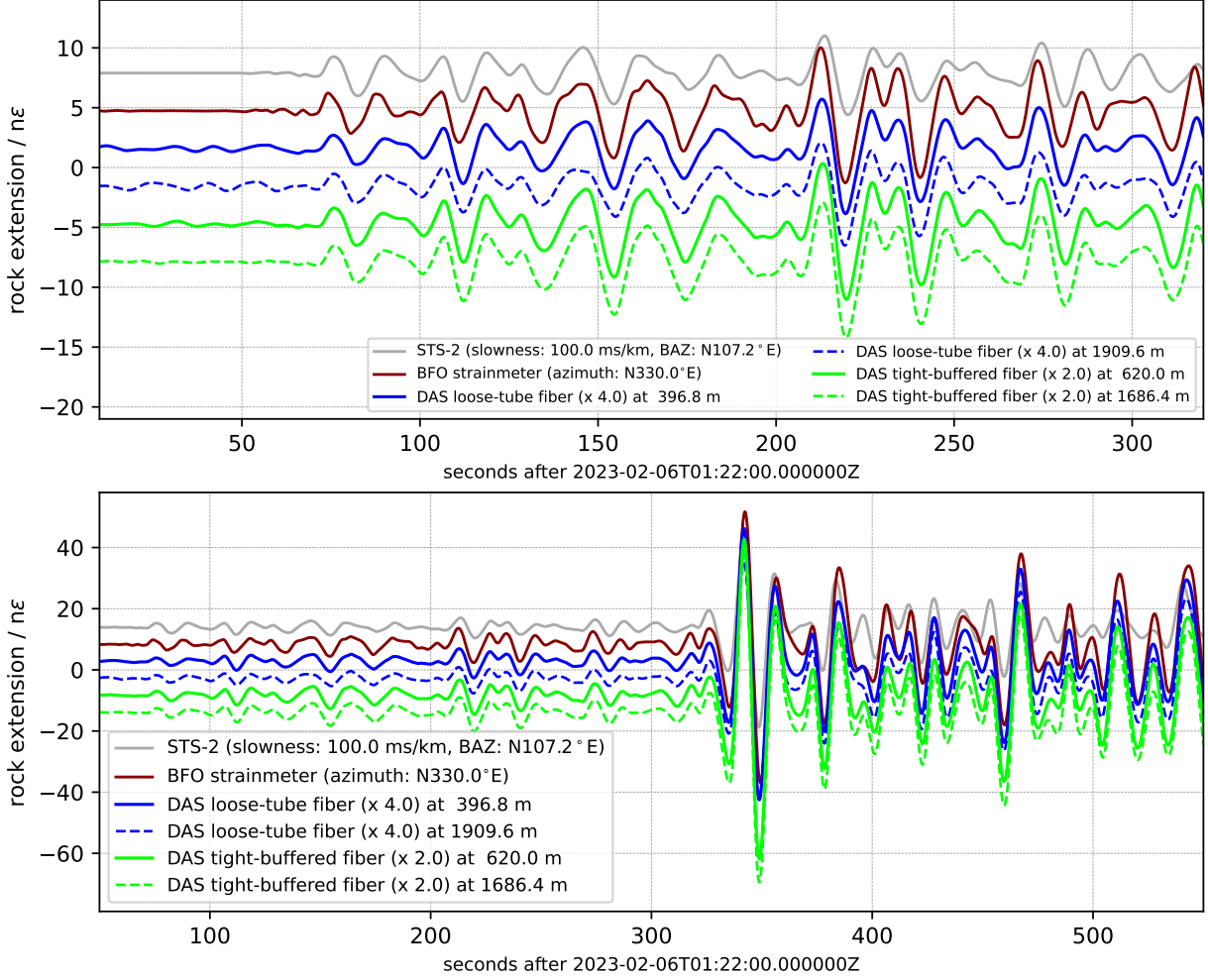


Figure S22: Strain waveforms as recorded for the azimuth (N330°E) of the ‘Anton Gang’ for the first of the main shocks of the Kahramanmaraş earthquakes: Mw 7.69 Turkey 2023-02-06 01:17:34.97 UTC 37.23°N 37.05°E 10.0 km (BAZ=N107.24°E, $\Delta=23.64^\circ$). Top: P-waves, bottom: P- and S-waves. First arrival times according to raytracing (obspy.taup.TauPyModel) with IASP91 are: P: 2023-02-06 01:22:46.44 UT and S: 2023-02-06 01:27:22.57 UT. P-waves arrive with a minimum slowness of 82.3 ms km^{-1} and a maximum slowness of 94.2 ms km^{-1} . The value range for the S-waves is 146.0 ms km^{-1} to 214.5 ms km^{-1} . The seismometer data are scaled by Eq. (S6). A band-pass from 0.05 Hz to 0.1 Hz is applied to all signals. The seismometer data was equalized to this filter response.

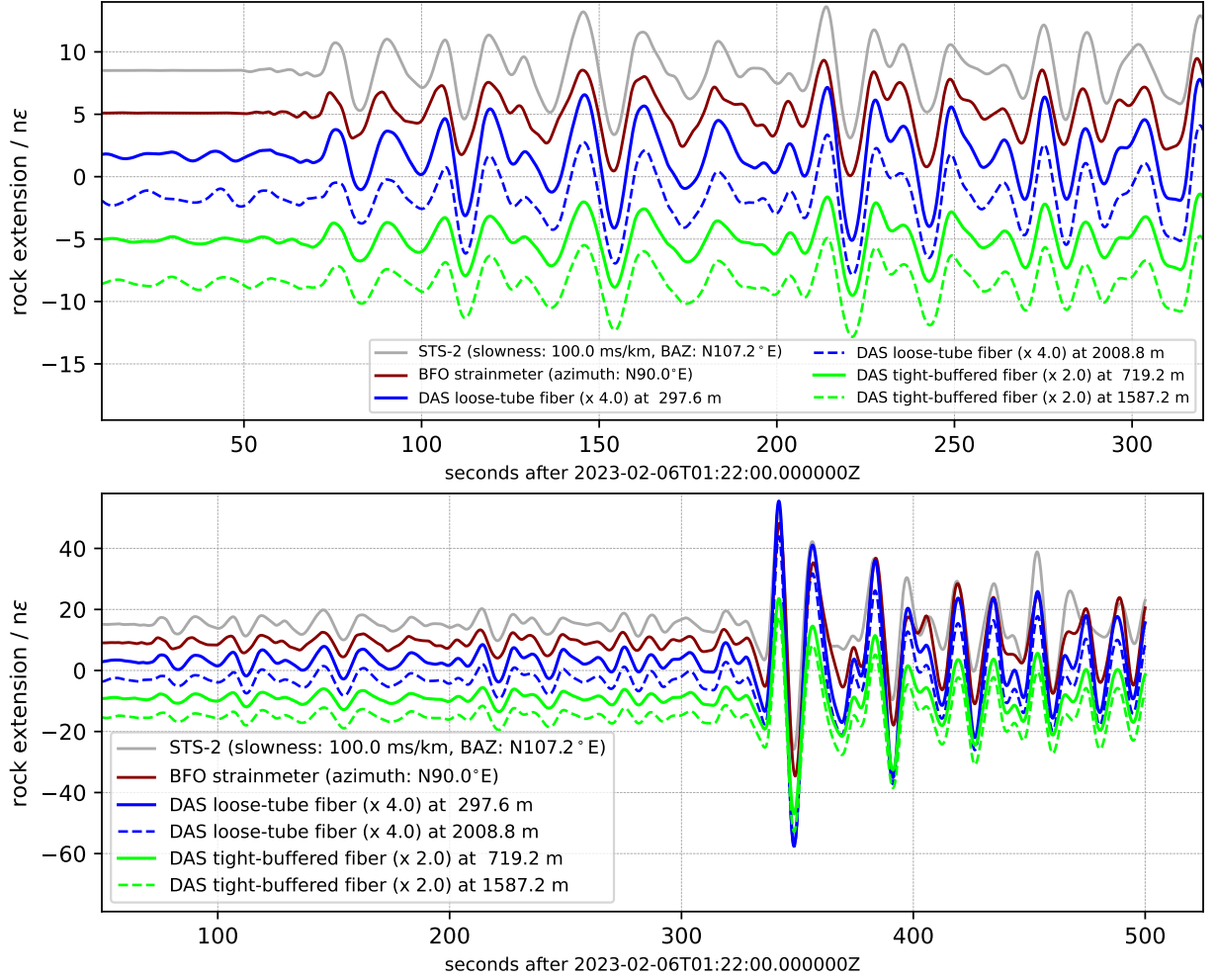


Figure S23: Strain waveforms as recorded for the azimuth (N90°E) of the ‘Vorstellen’ for the first of the main shocks of the Kahramanmaraş earthquakes: Mw 7.69 Turkey 2023-02-06 01:17:34.97 UTC 37.23°N 37.05°E 10.0 km (BAZ=N107.24°E, $\Delta=23.64^\circ$). Top: P-waves, bottom: P- and S-waves. First arrival times according to raytracing (obspy.taup.TauPyModel) with IASP91 are: P: 2023-02-06 01:22:46.44 UT and S: 2023-02-06 01:27:22.57 UT. P-waves arrive with a minimum slowness of 82.3 ms km^{-1} and a maximum slowness of 94.2 ms km^{-1} . The value range for the S-waves is 146.0 ms km^{-1} to 214.5 ms km^{-1} . The seismometer data are scaled by Eq. (S6). A band-pass from 0.05 Hz to 0.1 Hz is applied to all signals. The seismometer data was equalized to this filter response.

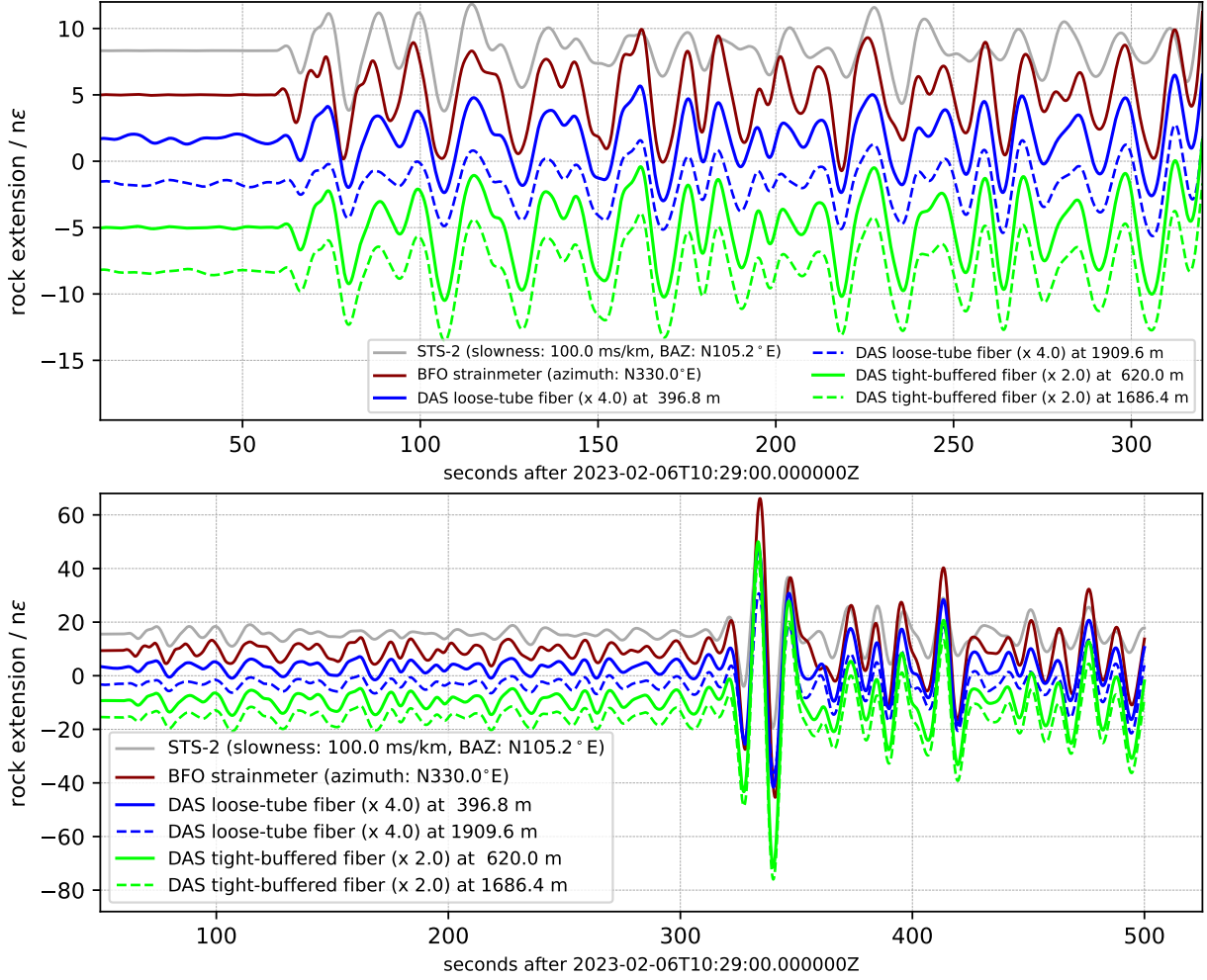


Figure S24: Strain waveforms as recorded for the azimuth (N330°E) of the ‘Anton Gang’ for the first of the main shocks of the Kahramanmaraş earthquakes: Mw 7.59 Turkey 2023-02-06 10:24:49.96 UTC 38.11°N 37.22°E 10.0 km (BAZ=N105.26°E, $\Delta=23.24^\circ$). Top: P-waves, bottom: P- and S-waves. First arrival times according to raytracing (obspy.taup.TauPyModel) with IASP91 are: P: 2023-02-06 10:29:57.35 UT and S: 2023-02-06 10:34:27.98 UT. P-waves arrive with a minimum slowness of 82.4 ms km^{-1} and a maximum slowness of 94.7 ms km^{-1} . The value range for the S-waves is 146.7 ms km^{-1} to 214.7 ms km^{-1} . The seismometer data are scaled by Eq. (S6). A band-pass from 0.05 Hz to 0.1 Hz is applied to all signals. The seismometer data was equalized to this filter response.

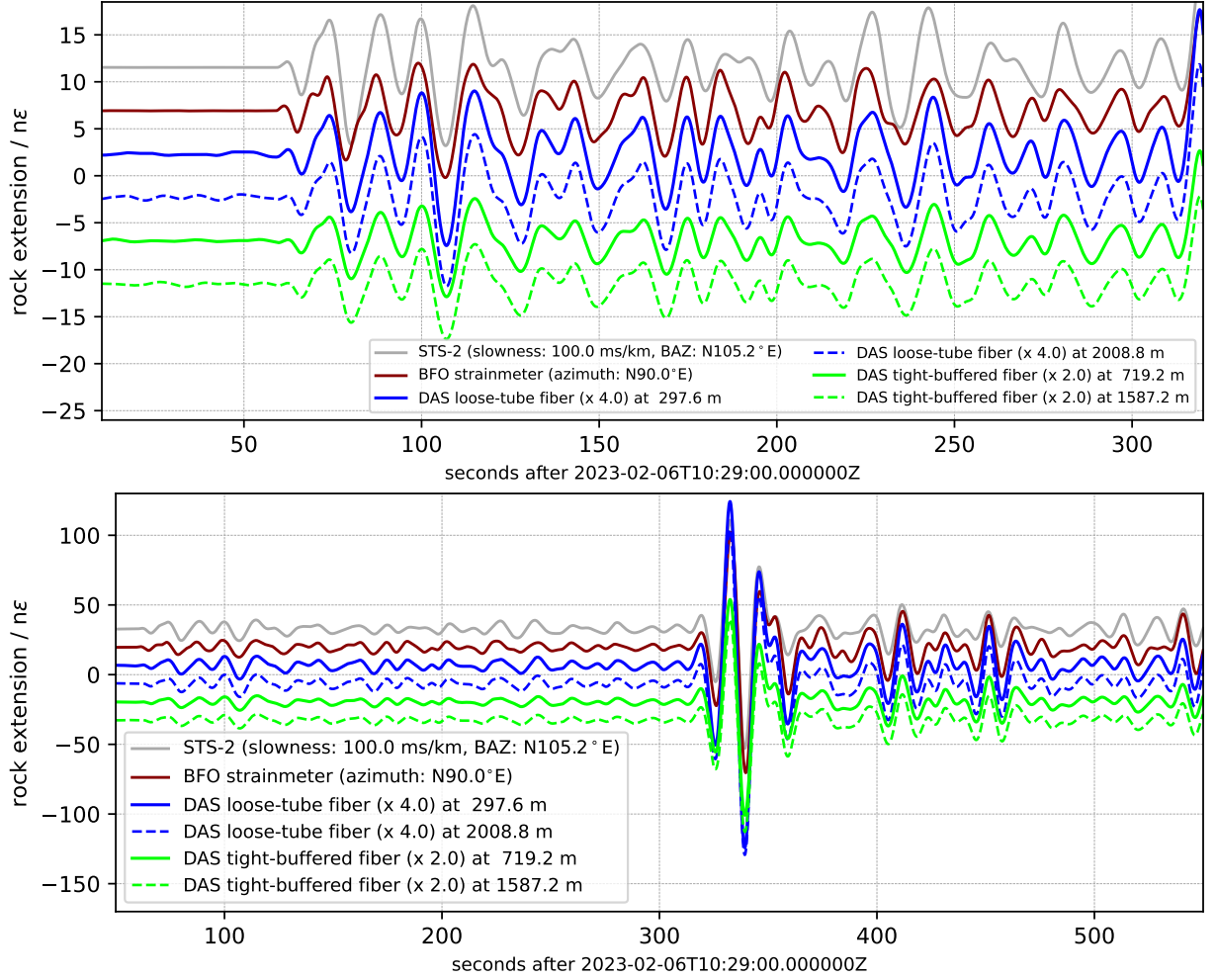


Figure S25: Strain waveforms as recorded for the azimuth (N90°E) of the ‘Vorstollen’ for the first of the main shocks of the Kahramanmaraş earthquakes: Mw 7.59 Turkey 2023-02-06 10:24:49.96 UTC 38.11°N 37.22°E 10.0 km (BAZ=N105.26°E, $\Delta=23.24^\circ$). Top: P-waves, bottom: P- and S-waves. First arrival times according to raytracing (obspy.taup.TauPyModel) with IASP91 are: P: 2023-02-06 10:29:57.35 UT and S: 2023-02-06 10:34:27.98 UT. P-waves arrive with a minimum slowness of 82.4 mskm^{-1} and a maximum slowness of 94.7 mskm^{-1} . The value range for the S-waves is 146.7 mskm^{-1} to 214.7 mskm^{-1} . The seismometer data are scaled by Eq. (S6). A band-pass from 0.05 Hz to 0.1 Hz is applied to all signals. The seismometer data was equalized to this filter response.

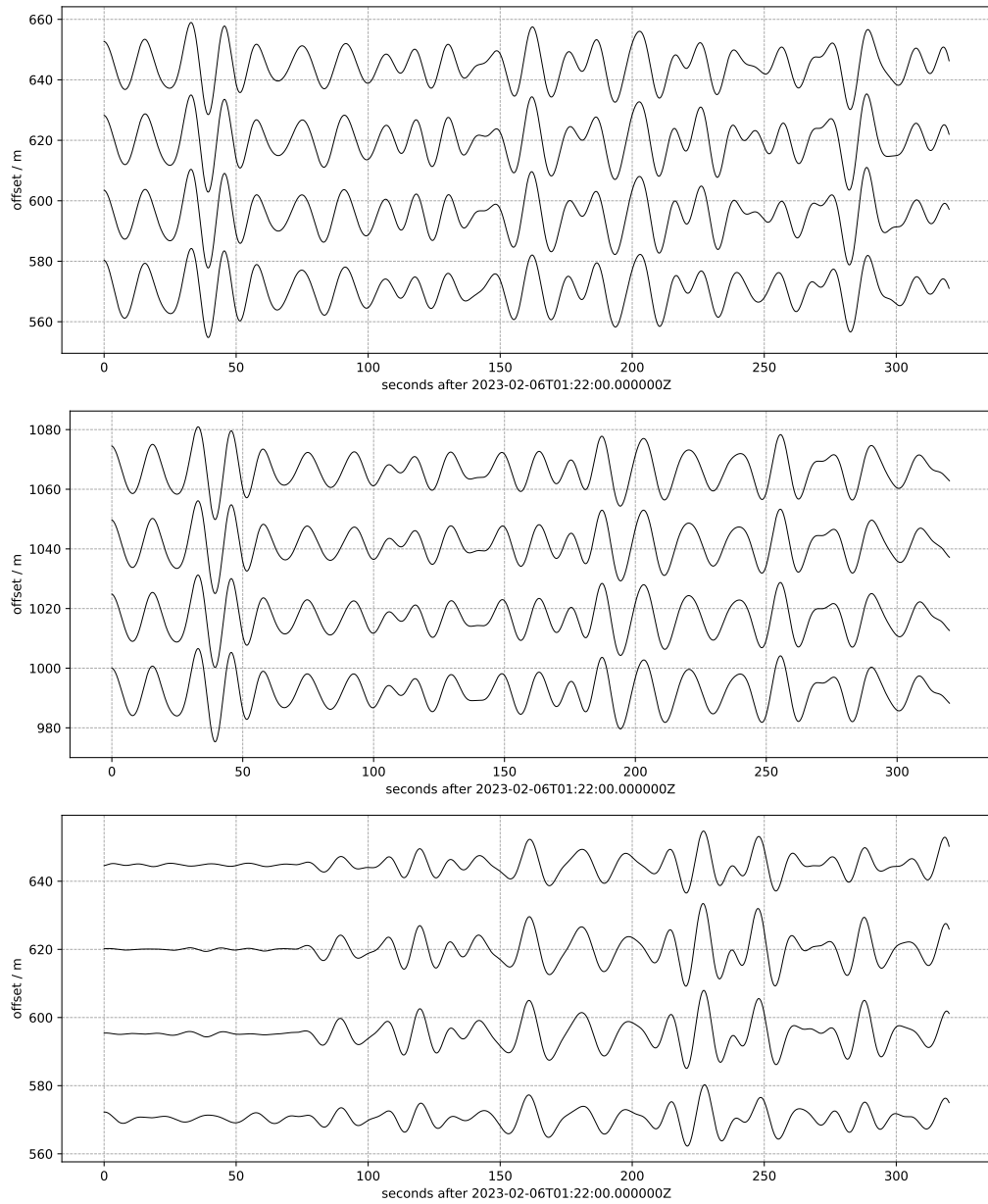


Figure S26: Demonstration of the reduction of coherent (common-mode) noise. The P-waves from the Mw 7.7 Pazarcık earthquake arrive in the displayed time window. All signals are filtered to the frequency band of 0.05 Hz to 0.1 Hz and are scaled to the same 5 m/nstrain. Top: recorded waveforms for channels between 570 m and 670 m. Center: recorded waveforms for channels between 1000 m and 1100 m (on the reference drum). Bottom: recorded waveforms for channels between 570 m and 670 m after the average of the recorded waveforms between 1000 m and 1100 m has been removed. The channel at 620 m is one of the two channels from the tight-buffered cable in the ‘Anton Gang’.

Only after subtracting the signal from the reference coil, the P-wave arrival (at 70 s on the time scale) becomes apparent.

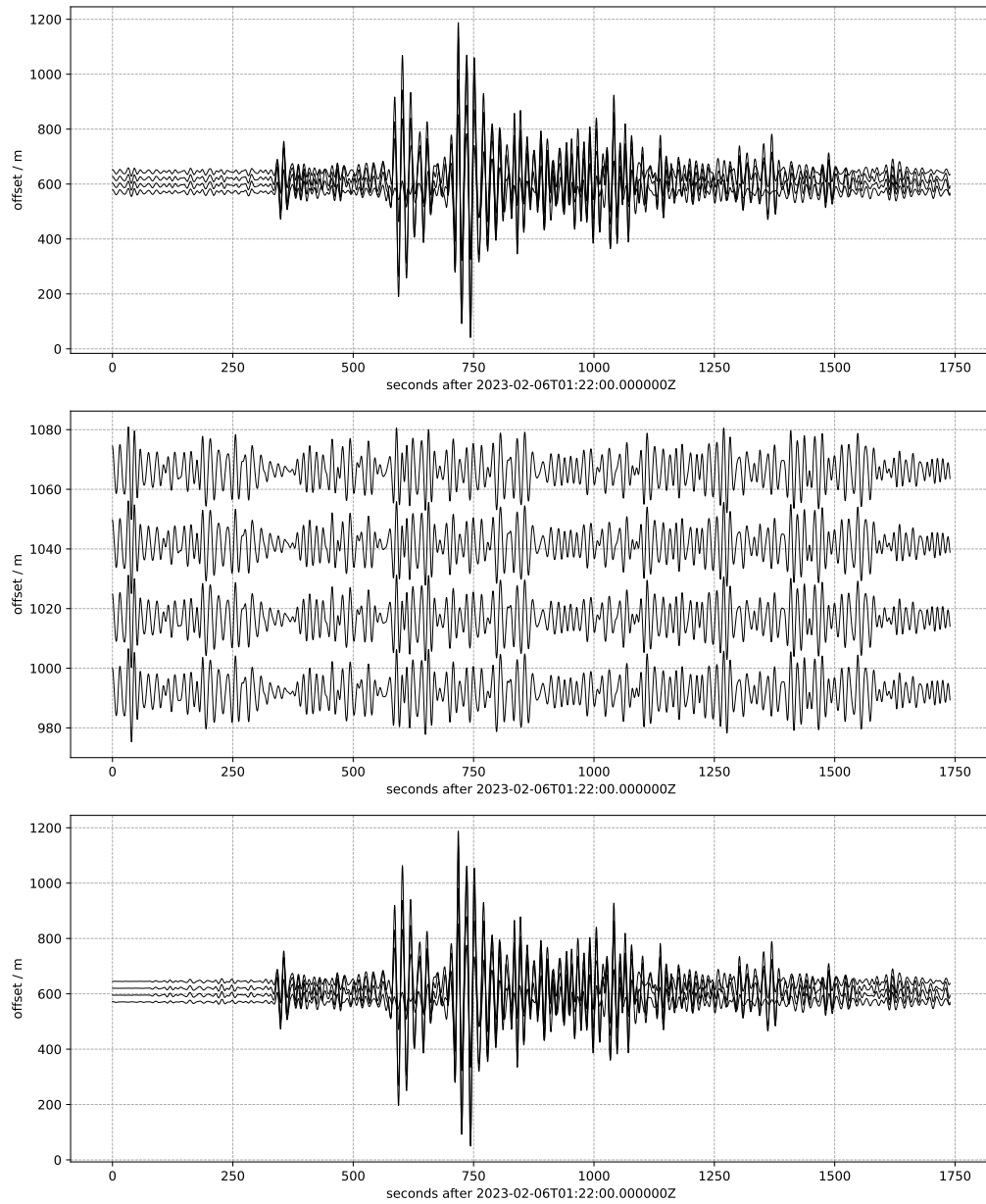


Figure S27: Demonstration of the reduction of coherent (common-mode) noise. The wave-train (including P-, S-, and surface waves) of the Mw 7.7 Pazarcık earthquake arrives in the displayed time window. All signals are filtered to the frequency band of 0.05 Hz to 0.1 Hz and are scaled to the same 5 m/nstrain, while the total axes range differs for the three panels. Top: recorded waveforms for channels between 570 m and 670 m. Center: recorded waveforms for channels between 1000 m and 1100 m (on the reference drum). Bottom: recorded waveforms for channels between 570 m and 670 m after the average of the recorded waveforms between 1000 m and 1100 m has been removed. The channel at 620 m is one of the two channels from the tight-buffered cable in the ‘Anton Gang’. The surface waves of the Mw 7.7 Pazarcık earthquake are the largest amplitude strain signals in the entire analyzed data. No signature of this earthquake signal, which has a signal-to-noise ratio of about 60 with respect to the coherent noise in the raw recording shown in the top panel, is apparent in the recording from the reference drum.

S3 Additional diagrams to complement the main results

Here we present some additional diagrams to support the main findings of the study. In Fig. S28 ‘strain transfer rate’ (STR) is plotted against the backazimuth (BAZ) of the respective event. We observe no significant correlation between both parameters. Fig. S29 shows STRs against NCCs. We find no correlation either. These results highlight that the STRs predominantly depends on cable type and installation conditions.

For the main shocks (Mw 7.7 and Mw 7.6) of the Kahramanmaraş earthquake sequence on February 6th 2023, we analyze the body waves in addition to the surface waves. Fig. S30 shows STRs and Fig. S31 displays NCCs. For these large amplitude signals, we observe large signal-to-noise ratio, which implies a high waveform similarity. Hence, the NCCs generally are larger than 0.92 and are largest (> 0.99) for the surface wave signals recorded in the ‘Anton Gang’ with the tight-buffered cable.

The ‘strain transfer rate’ is not correlated to the normalized correlation coefficient, like shown in Fig. S29, because smaller values of NCC are due to noise in the

DAS data, not in the strainmeter data. In this study, we fit strainmeter against DAS data in order to determine the STR. This approach provides reasonable STR, even for heavily disturbed DAS data. This is particularly the case in the ‘Vorstollen’, with the loose-tube cable, for which NCC are globally small. Among the 19 events, illustrative examples of the situation are shown in Figs. S12, S8, S9, and S13 (bottom panels),

In the linear regression the noise in the regressor causes a bias for the regression coefficients to smaller values. If we use the DAS data as regressors in fitting the DAS waveform to the strainmeter data, we find a correlation of the regression coefficients with the NCC, which is demonstrated in Fig. S32. The signal-to-noise ratio for the strainmeter data is much better in all cases, such that no bias is found in Fig. S29, where the strainmeter data is used as regressor.

Fig. S33 displays a plot of NCC against the maximum strain amplitude. We observe a clear trend where smaller strain amplitudes are associated with lower NCC values. For smaller strain amplitudes the noise in the DAS data takes a larger fraction of the signal energy. The effect is stronger for the loose-tube cable than for the tight-buffered cable and is strongest in the ‘Vorstollen’, where cables are not embedded in sand.

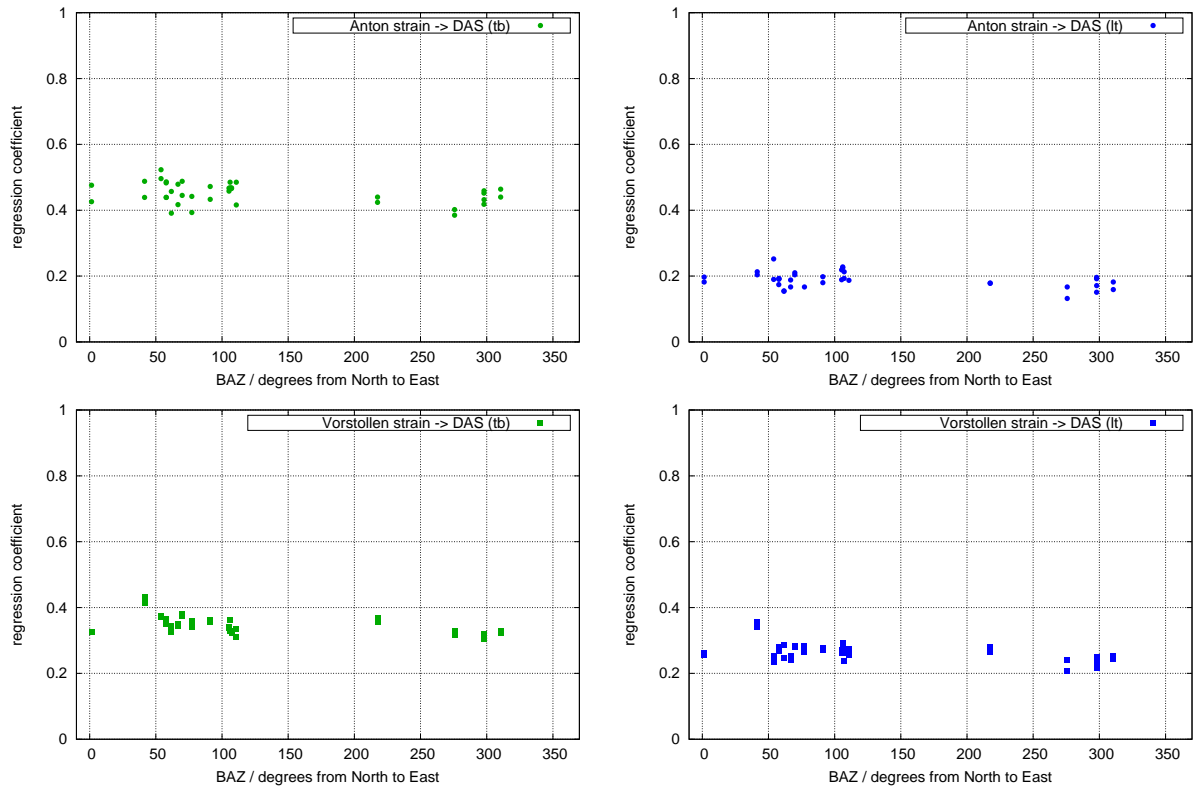


Figure S28: ‘strain transfer rate’ (regression coefficients for fitting strainmeter data to the DAS data) plotted against the backazimuth. Results for both cables (left: tight-buffered, right: loose-tube) and both locations (top: ‘Anton Gang’, bottom: ‘Vorstollen’) are displayed.

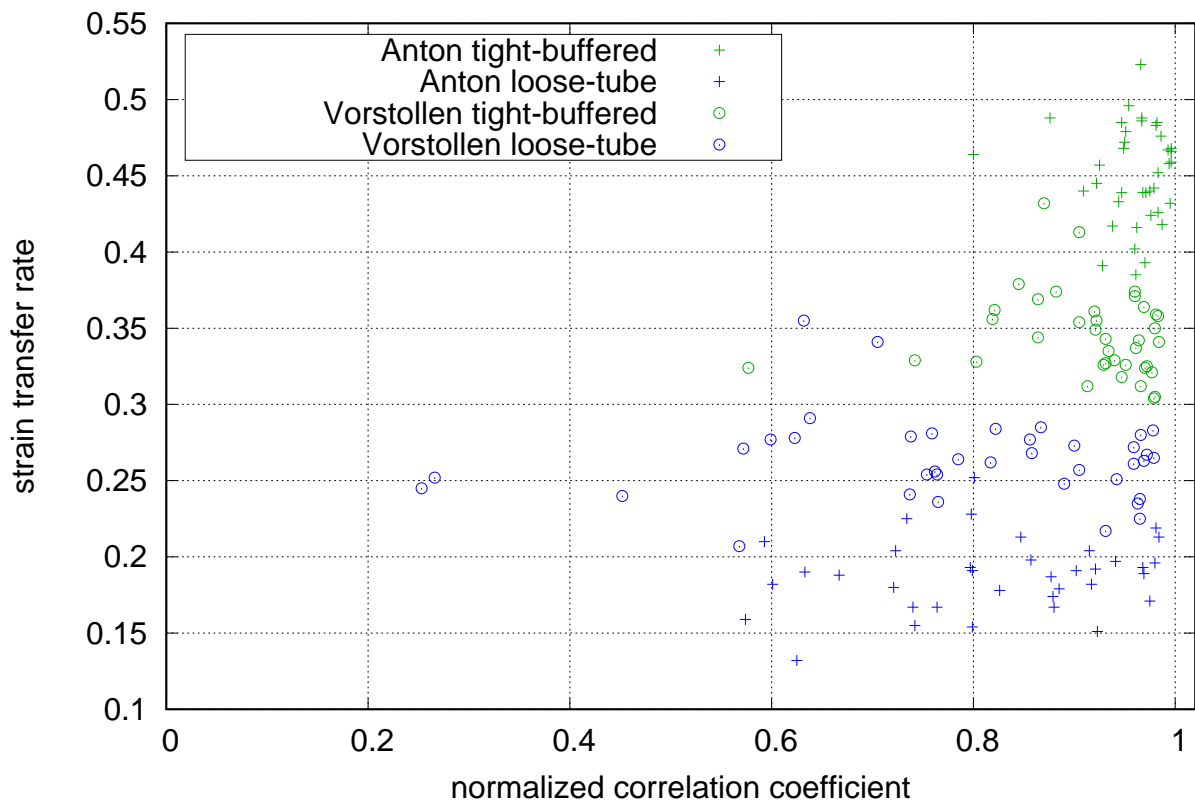


Figure S29: Measured ‘strain transfer rate’ plotted against the normalized correlation coefficient for each of the 19 events studied in the analysis. The analysis focuses on surface waves and on the comparison between linear strain recorded by the DAS and strainmeter in a given azimuth. The measurements are carried out on sensing points situated along the ‘Anton Gang’ (crosses) and ‘Vorstollen’ (circles) and in loose-tube (blue) and tight-buffered (green) cables.

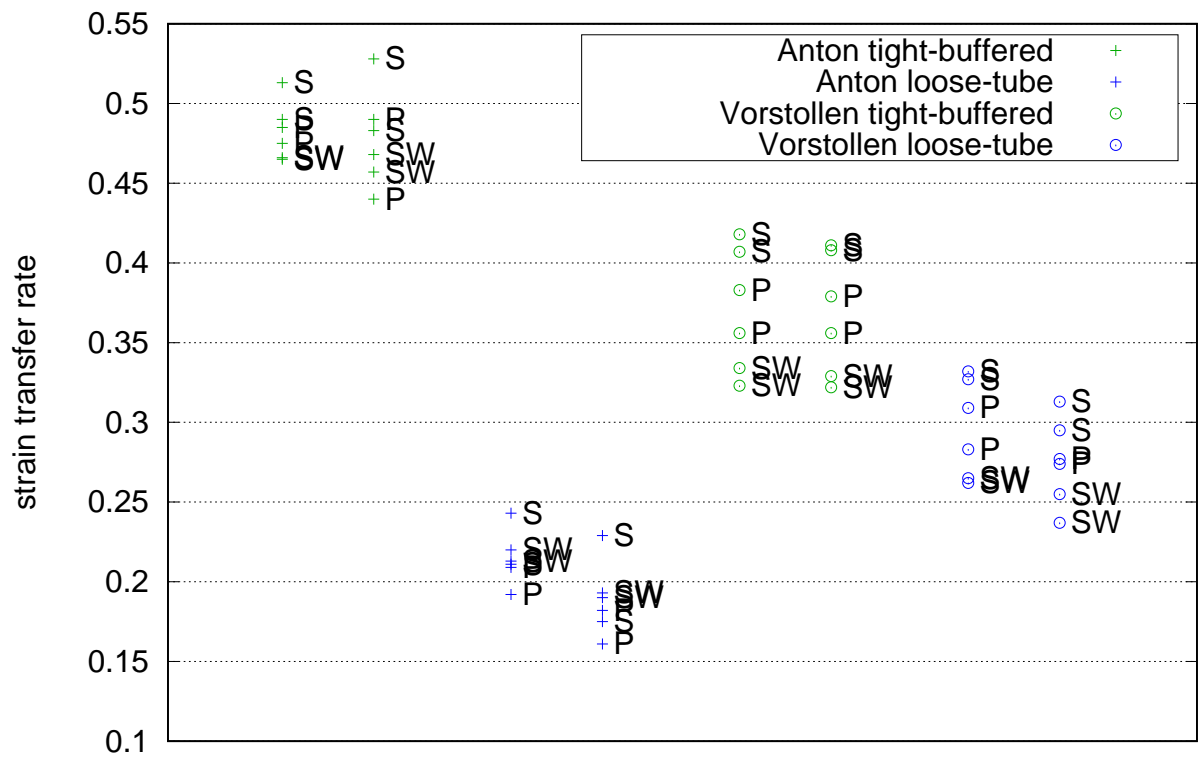


Figure S30: Measured ‘strain transfer rate’ for the main shocks (Mw 7.7 and Mw 7.6) of the Kahramanmaraş earthquake sequence on February 6th 2023. The analysis focuses on P, S and surface waves (SW), on the comparison between linear strain recorded by the strainmeter versus the DAS, in a given azimuth. For each phase, the measurements are carried out on sensing points situated along the ‘Anton Gang’ (crosses) and ‘Vorstollen’ (circles) and in loose-tube (blue) and tight-buffered (green) cables. The corresponding phases are indicated near the data points.

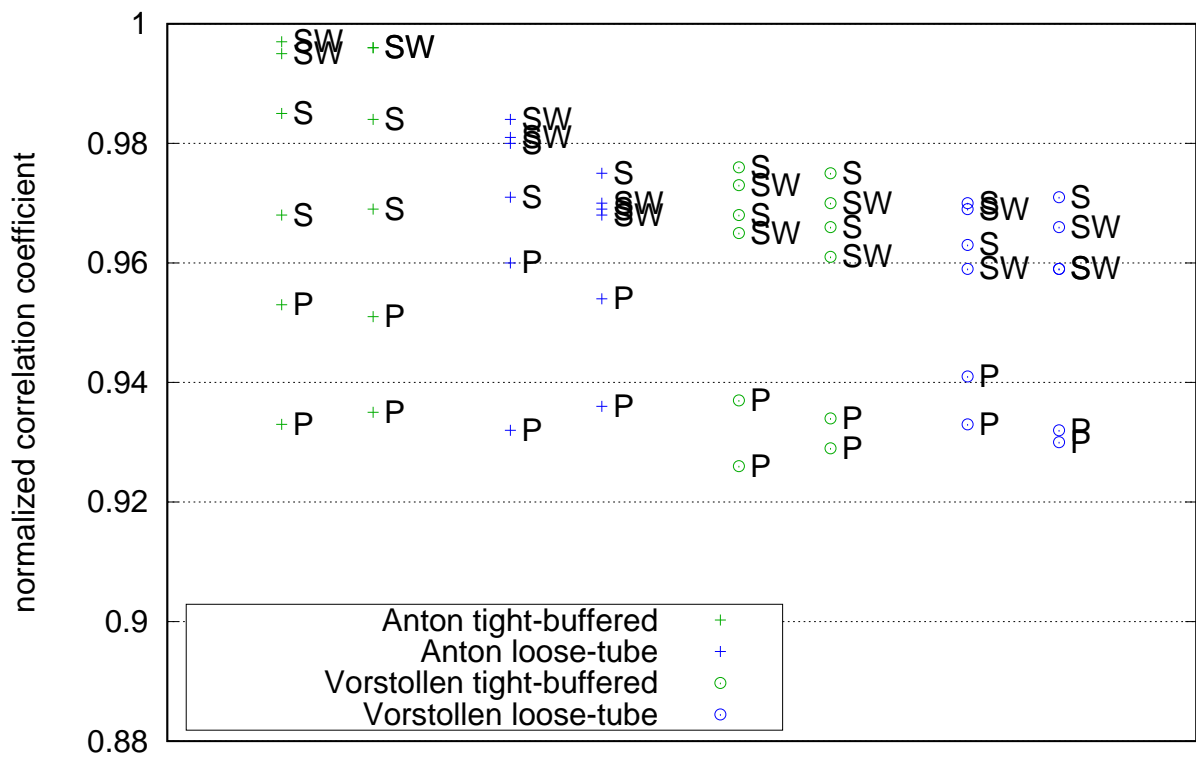


Figure S31: Normalized correlation coefficients for the main shocks (Mw 7.7 and Mw 7.6) of the Kahramanmaraş earthquake sequence on February 6th 2023. The analysis focuses on P, S and surface waves (SW), on the comparison between linear strain recorded by the strainmeter versus the DAS, in a given azimuth. For each phase, the measurements are carried out on sensing points situated along the ‘Anton Gang’ (crosses) and ‘Vorstollen’ (circles) and in loose-tube (blue) and tight-buffered (green) cables. The corresponding phases are indicated near the data points.

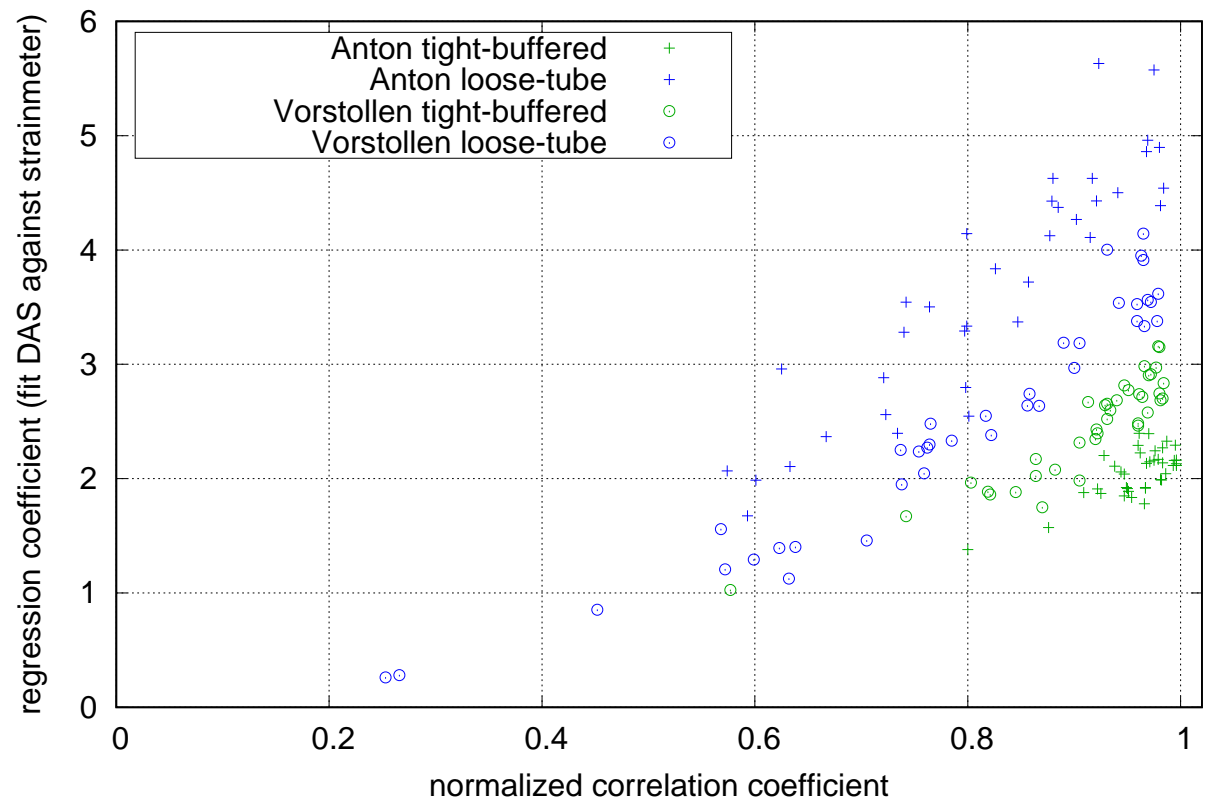


Figure S32: Regression coefficient for fitting DAS data to strainmeter waveforms plotted against the normalized correlation coefficient for each of the 19 events studied in the analysis. The analysis focuses on surface waves and on the comparison between linear strain recorded by the DAS and strainmeter in a given azimuth. The measurements are carried out on sensing points situated along the ‘Anton Gang’ (crosses) and ‘Vorstollen’ (circles) and in loose-tube (blue) and tight-buffered (green) cables.

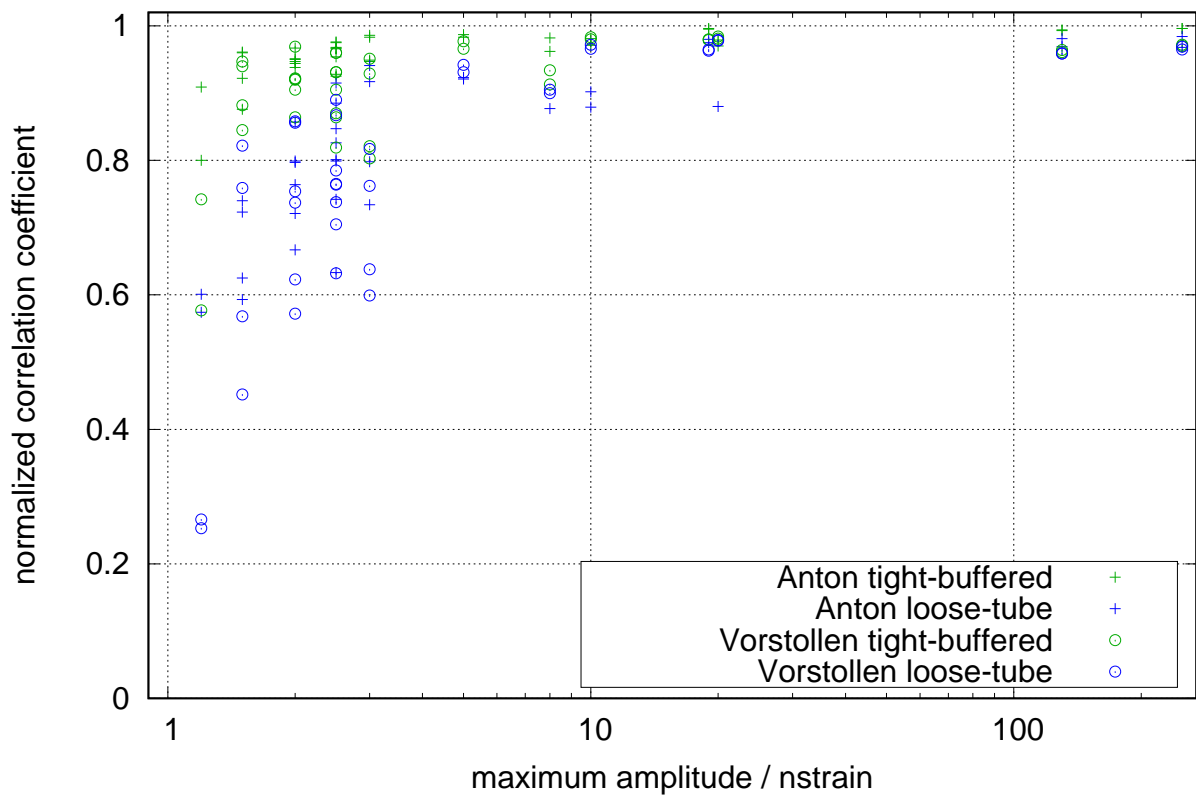


Figure S33: Normalized correlation coefficient plotted against the maximum signal amplitude for each of the 19 events studied in the analysis. The values of maximum amplitude are those in listed in Table S2 and are given per event and not per actual time series and should be understood as a proxy for the actual signal amplitude. The analysis focuses on surface waves and on the comparison between linear strain recorded by the DAS and strainmeter in a given azimuth. The measurements are carried out on sensing points situated along the ‘Anton Gang’ (crosses) and ‘Vorstollen’ (circles) and in loose-tube (blue) and tight-buffered (green) cables.

S4 Plane wave strain from seismometer recordings

In this study, we fit waveforms of ‘rock strain’ recorded by the array of Invar-wire strainmeters at BFO (Zürn et al., 2015) to ‘fiber strain’ recorded by DAS. The regression coefficient is the ‘strain transfer rate’ (STR), a measure of how much of the strain amplitude is picked up by the DAS fibers. Strainmeters are rare installations and in the absence of these types of sensors studies of DAS recorded strain occasionally compare the signals with strain simulated from particle velocity recorded by seismometers, or convert DAS signals to equivalent particle velocity recordings. This conversion is possible in cases where the waveform represents a plane wave of known phase velocity and azimuth of propagation.

In section S4.1 ‘Scaling rule for plane waves’ we summarize the theory behind this conversion. The final conversion rule is given by Eq. (S6) and is valid for a single, non-dispersive plane wave.

When using surface wave-data, which provide superior signal-to-noise ratio because of their large amplitudes (compared to body-wave signals) the limitations of the plane-wave approximation become significant. The surface waves are dispersive and do not propagate with a single phase-velocity and Love- and Rayleigh-waves are inseparably superimposed. Due to their propagation along the surface of the heterogeneous Earth’s crust, they have non-plane character and contain significant components, which do not propagate along the backazimuth (BAZ) great circle. These limitations become most obvious for BAZ being perpendicular to the azimuth of measured linear strain. The plane wave does not strain the material perpendicular to the direction of propagation and the value of the cosine in Eq. (7) necessarily vanishes. The recorded signals then entirely are composed by the non-plane components of the wave, not propagating along the BAZ great circle. The problem becomes already apparent for BAZ being close to perpendicular to strain azimuth. The seismometer recorded particle velocity contains as well these non-plane components, which are at variance with the expected polarization of the plane wave. Thus the scaling in Eq. (S6) is not valid for them. We discuss the consequences of this on the regression coefficients in section S4.2 ‘Regression with respect to seismometer data’. In section S4.3 ‘Comparison of seismometer and strainmeter data’ we discuss a direct comparison of strainmeter and seismometer data.

S4.1 Scaling rule for plane waves

For signals of single non-dispersive plane waves, strain can be simulated from particle velocity recorded by a seismometer. Consider that ground deformation is due

to a non-dispersive plane wave, then particle displacement at location \vec{r} and time t is

$$\vec{u}(\vec{r}, t) = \vec{U} f(\vec{s}\vec{r} - t), \quad (\text{S1})$$

where \vec{s} is the slowness-vector of the plane wave, \vec{U} defines the polarization and $f(t)$ is the shape of the wave (d’Alembert’s solution to the wave equation), which propagates in direction of the slowness vector.

The linear strain in x -direction for this wave is

$$\epsilon_{xx}(\vec{r}, t) = \frac{d}{dx} u_x(\vec{r}, t) = U_x s_x f'(\vec{s}\vec{r} - t), \quad (\text{S2})$$

where $f'(t)$ is the derivative of $f(t)$ with respect to t and u_x , s_x , and U_x are the x -components of the slowness vector \vec{s} , of \vec{u} , and of \vec{U} , respectively. Likewise the x -component of particle velocity is

$$v_x(\vec{r}, t) = \frac{d}{dt} u_x(\vec{r}, t) = -U_x f'(\vec{s}\vec{r} - t). \quad (\text{S3})$$

Hence

$$\frac{\epsilon_{xx}(\vec{r}, t)}{v_x(\vec{r}, t)} = -s_x. \quad (\text{S4})$$

If the x -direction is the horizontal direction along the ‘Anton Gang’ or the ‘Vorstollen’, given by azimuth ψ_x and s_h is the horizontal component of the plane wave slowness for propagation in a 1D structure, as can be derived by ray-tracing, then

$$s_x = s_h \cos(\psi_{\text{BAZ}} - \psi_x - 180^\circ), \quad (\text{S5})$$

where ψ_{BAZ} is the backazimuth of the source. In this way we estimate the linear strain in x -direction

$$\epsilon_{xx}(\vec{r}, t) = -s_h \cos(\psi_{\text{BAZ}} - \psi_x - 180^\circ) v_x(\vec{r}, t) \quad (\text{S6})$$

from the particle velocity $v_x(\vec{r}, t)$ as recorded by the broad-band seismometer.

S4.2 Regression with respect to seismometer data

Fig. S34 compares the regression coefficients measured by fitting strainmeter signals to DAS signals (filled symbols), with those obtained by fitting scaled seismometer data to DAS signals (open symbols). The seismometer data is scaled according to Eq. (S6) to represent linear strain in the direction of the DAS fiber in cases where the waves propagate along the BAZ great circle with phase slowness $s_h = 280 \text{ ms km}^{-1}$. This value corresponds to phase velocity of 3.57 km s^{-1} , which is the value for Rayleigh waves at 0.05 Hz (the lower end of the investigated frequency band) as shown for Southern Germany by Friederich and Huang (1996). Love-waves propagate with a higher phase velocity. For both wave types phase velocity decreases with increasing frequency, such that the chosen value lies within the range to be expected in the observed wave trains.

The regression coefficients obtained by fitting the strainmeter waveform against the DAS waveform are the STRs, as displayed in Fig. S28. They are reproduced for reference. The regression coefficients for fitting the scaled seismometer waveform against the DAS waveform show a considerably stronger scatter, not only for cases where BAZ is close to perpendicular to the strain azimuth.

Cases where BAZ is close to $N60^\circ E$ or $N240^\circ E$ have a great-circle propagation direction almost perpendicular to the azimuth of the ‘Anton Gang’ ($N330^\circ E$). For the Vorstollen ($N90^\circ E$), the same applies when BAZ is close to $N0^\circ E$ or $N180^\circ E$. Most of these cases are illustrated in Fig. S34. The coefficients are significantly outside reasonable limits, with some even being negative. The scatter is more substantial for the ‘Anton Gang’, where we find several cases with BAZ almost perpendicular to the strain azimuth. For the ‘Vorstollen’ the study includes one case with BAZ near $N0^\circ E$, but none with BAZ near $N180^\circ E$. In consequence the overall scatter is less strong.

For data from the ‘Vorstollen’ we also observe a systematic shift between coefficients obtained for regression with respect to strainmeter data compared to regression with respect to seismometer data. The seismometer data appears to over-estimate the strain amplitude, such that it has to be downscaled by a factor of about 0.5 with respect to the coefficients obtained with the strainmeter data. The P-wave signals in Figs. S23 and S25 show an amplitude mismatch of a similar size. This might be a consequence of strain-strain coupling due to the local topography as discussed in section S2.5 ‘Distortion of the strain field due to local heterogeneity’. The East-West strain measured by the strainmeters as well as by the DAS fibers in the ‘Vorstollen’ is reduced compared to what is estimated from particle velocity (seismometer data). From tidal analysis Zürn et al. (2015, their table S2 in the supporting material) estimate a factor of 0.58 for $N60^\circ E$ and Emter and Zürn (1985, their figure 5) derive a factor of 0.67 by a 2D finite element analysis. Both are in the order of magnitude of the bias

seen in Fig. S34 for the ‘Vorstollen’.

Apart from these amplitude related issues, the DAS waveforms also show greater similarity to the strainmeter waveforms than to the seismometer waveforms. This is shown in Fig. S35, where the values of NCCs are plotted against backazimuth. The NCC measured by comparing DAS data with respect to seismometer data are generally smaller than for DAS with respect to the strainmeter data. For BAZ nearly perpendicular to the fiber optic cable azimuth, some of the signals are even anti-correlated (Fig. S35). This results from the change in the sign of the cosine in Eq. (S6).

The dissimilarity is attributed to the non-plane components of the waves, rather than to instrumental noise or signal-to-noise ratio (SNR) issues. Both the strainmeter and seismometer data exhibit significantly better SNR than the DAS data, with the seismometer having the highest SNR among the instruments compared. This can be seen in Figs. S22, S24, S23, and S25, where the signal level prior to the P-wave onset is least for the seismometer data, when compared to the P-wave amplitude.

S4.3 Comparison of seismometer and strainmeter data

To evaluate how well strain from particle velocity recorded by the seismometer can represent ‘rock strain’, we perform a direct comparison between the strain waveforms from the strainmeter array and those derived from the particle velocity recorded by the seismometer. Fig. S36 shows the results of the comparison. If the seismometer signal scaled by Eq. (S6) would be a good representation of ‘rock strain’, all these coefficients would equal 1. This takes place in only very few cases. If the mismatch would be due to an amplitude factor only, the coefficients for fitting the strainmeter data to the seismometer data would be the reciprocals of the coefficients computed when fitting seismometer data to strainmeter data. This is not the case, due to a considerable waveform mismatch caused by non-plane components of the surface waves.

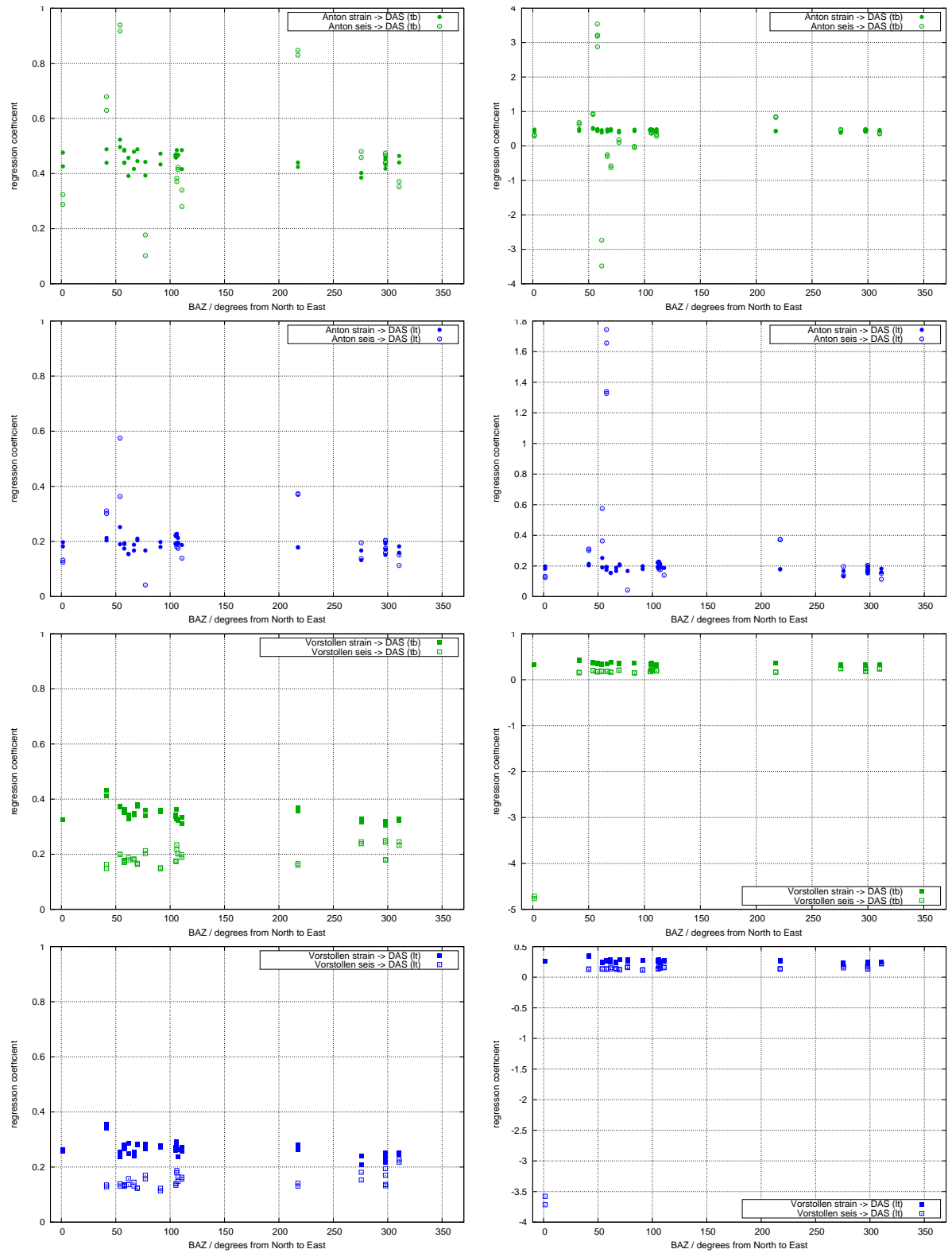


Figure S34: Regression coefficients obtained when fitting to the DAS data and using the strainmeter data (filled symbols) as regressor on the one hand and seismometer data (open symbols) on the other hand. The values are plotted against the BAZ of the respective earthquake. The diagrams on the left are limited to values from 0 to 1. The diagrams on the right show the full scatter. From top to bottom: tight-buffered in the ‘Anton Gang’, loose-tube in the ‘Anton Gang’, tight-buffered in the ‘Vorstollen’, loose-tube in the ‘Vorstollen’. The seismometer data is scaled for a slowness of 280 ms km^{-1} , equivalent to a phase velocity of 3.57 km s^{-1} .

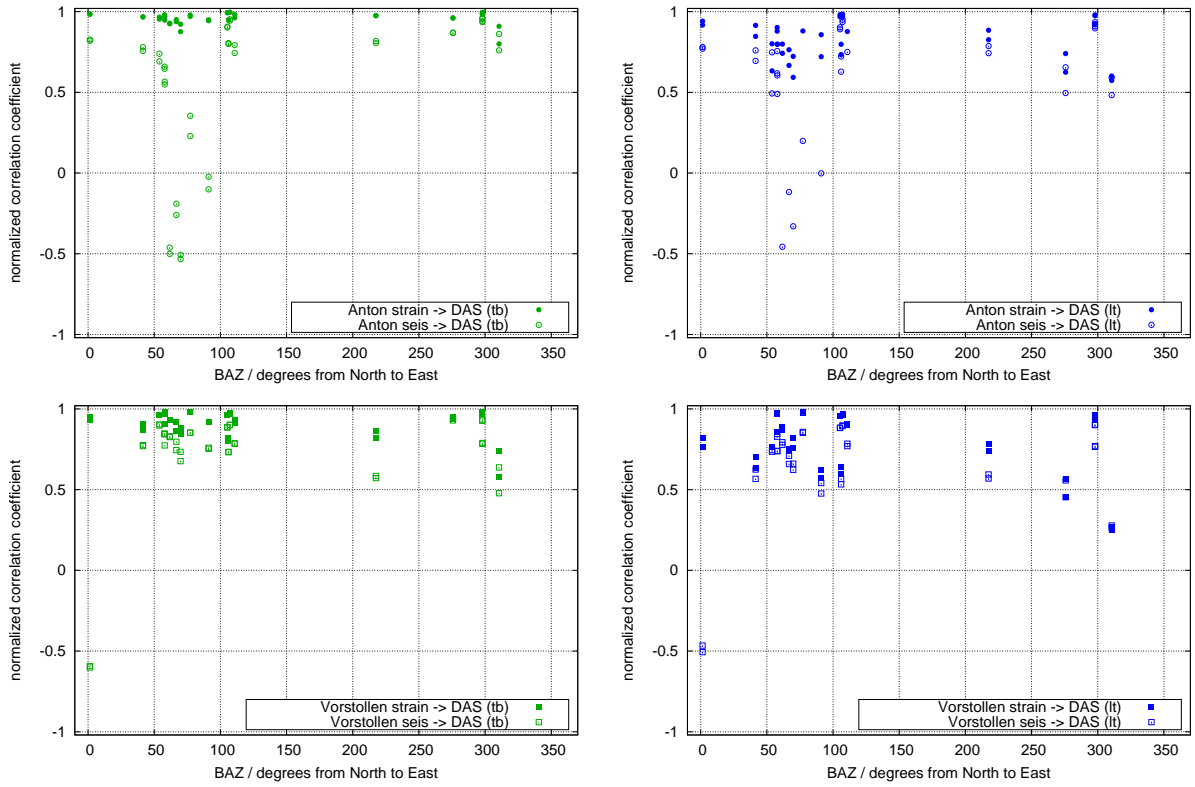


Figure S35: Normalized correlation coefficients for DAS data and strainmeter data (filled symbols) on the one hand and seismometer data (open symbols) on the other hand. Results are plotted against the backazimuth. Results for both cables (left: tight-buffered, right: loose-tube) and both locations (top: ‘Anton Gang’, bottom: ‘Vorstollen’) are displayed.

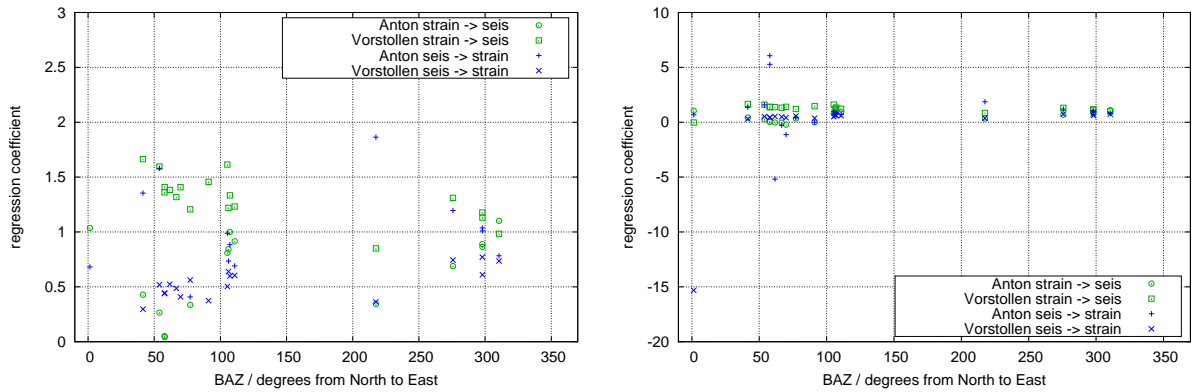


Figure S36: Regression coefficients when fitting surface wave strainmeter data to seismometer data (green) and fitting seismometer data to strainmeter data (blue). Results are displayed for the azimuths of the ‘Anton Gang’ (circles and pluses) and the ‘Vorstollen’ (squares and crosses). The values are plotted against the backazimuth (BAZ) of the respective earthquake. Left: limited value range. Right: full range. In cases, where the seismometer derived strain signal represents rock strain, the values equal 1. These cases are rare.